

ABSTRACT

SALEHI, AMIN. Manipulating Refractive Index In Organic Light Emitting Diodes and Direct Triplet Exciton Formation by Charge Injection. (Under the direction of prof. Franky So).

This work is a study on two major separate aspects of Organic Light Emitting Diodes (OLEDs). In the first half of this thesis, chapters two and chapter three, refractive index and the role of refractive index of constituting layers of a conventional OLED stack on light out-coupling efficiency is studied. It is shown that about 70% of the radiated power is lost to bound optical modes. Role of each mode and the effect of refractive index of each layer on each mode is studied. It is illustrated, that the transverse magnetic (TM) polarized bound modes, i.e. the transverse magnetic waveguided (TMWG) mode and the surface plasmon polariton (SPP) mode have the largest loss contributions. Further it is manifested that the TM-polarized modes are mainly distributed in the electron transporting layer (ETL) in a conventional OLED stack and reducing the refractive index of ETL can tremendously increase optical out-coupling at the expense of suppressing SPP and TMWG modes. It is displayed that transverse electric waveguide (TEWG) mode is mainly distributed in the transparent anode and the hole transporting layers (HTL) in a conventional OLED stack and reducing the refractive index of the transparent anode and the HTL can increase optical outcoupling at the expense of less TEWG loss. Refractive index of most of common organic thin films used in OLED devices is measured and reported. It is shown that majority of organic thin films show an in-plane negative birefringence due to anisotropic molecular geometry. Role of birefringence on light out-coupling is discussed and it is indicated that extraordinary (ordinary) refractive index mainly affects the TM (TE) polarized modes.

Furthermore, the refractive index of amorphous thin films deposited using physical vapor deposition can be reduced by pore-inclusion using oblique angle deposition (OAD). In OAD, a substrate is positioned at an oblique angle with respect to a collimated incident vapor flux. Upon

formation of initial islands, a self-shadowing lead to a porous columnar growth. The porosity is controlled by the angle of incident and, the refractive index of the thin film can be reduced in a controlled manner. In this work, refractive index of a common ETL, Alq3, is reduced using OAD, and the low-index ETL is incorporated in an OLED stack, resulting in a 30% increase in efficiency.

The second half of this thesis, chapter four, presents a major discovery which changes the understanding of exciton formation in organic semiconductors. According to the conventional understanding of organic semiconductors, electrons and holes can only be injected into the lowest unoccupied molecular orbital (LUMO) and highest occupied molecular orbital (HOMO) of an organic semiconductor, and the LUMO-HOMO gap is analogous to the bandgap in inorganic semiconductors, and the emitted photons have energies close to the HOMO-LUMO gap. Therefore, to form a radiative exciton a voltage equivalent to the HOMO-LUMO gap is required. Chapter four contradicts this understanding and shows evidence, for the first time, that charge carriers can readily be injected into the sub-bandgap (sub HOMO-LUMO gap) excitonic states, such as triplet states and then excite a band-gap exciton through bimolecular excitonic annihilation, such as triplet-triplet annihilation (TTA), and result in band-gap radiation. Based on the discovery, an efficient hyper-fluorescent blue OLED is made with sub-bandgap operating voltages. Although fluorescent OLEDs have a 25% limit for internal quantum efficiency, which results in a maximum external efficiency of 5%, the low operating voltage of the hyper-fluorescent OLED device which is presented in chapter four, results in power efficiencies that is comparable or larger than some of the best TADF and phosphorescent OLEDs with 100% internal efficiency. This ground-breaking discovery ushers in a new generation of fluorescent OLEDs, which are named here as Su-Per fluorescent OLEDs, after **Sub**-bandgap and **Hyper**-fluorescent.

© Copyright 2019 by Amin Salehi

All Rights Reserved

Manipulating Refractive Index in Organic Light Emitting Diodes and Direct Triplet Exciton
Formation by Charge Injection.

by
Amin Salehi

A dissertation submitted to the Graduate Faculty of
North Carolina State University
in partial fulfillment of the
requirements for the degree of
Doctor of Philosophy

Physics

Raleigh, North Carolina
2019

APPROVED BY:

Dr. Franky So
Committee Chair

Dr. David Aspnes

Dr. Daniel Dougherty

Dr. Linyou Cao

DEDICATION

To my wife Luna. For all your never-ending love and support through all these years.

I could have not done it without you.

BIOGRAPHY

I was born and raised in a small city, outside of the Iranian capital Tehran, in an academic family. My mother, Prof. Fatima Sarvi, an academic prodigy, is my academic and scientific backbone, and everything I am and I will be, is because of her. I was also blessed with a highly technical, hands-on and creative father, who instilled an experiential spirit in me from the early ages.

Since the very beginning I showed a great aptitude for science with an unquenchable mind. I assembled my first functioning electronic circuit (an FM radio) when I was 9 years old. 21 years later, I can still feel the excitement of when I first heard the sound coming out of the speaker. I fell in love with physics in middle school because of a great science teacher. At the age of 12, I won the silver medal in the science Olympiad in my province. Since my early teenage years, I realized that I wanted nothing in the world but to be a great physicist. Einstein, Plank, Rutherford, Newton, Fermi, Heisenberg, were my idols.

In pursuing my dream in studying physics, I learnt and became familiar with both fundamental and applied branches of physics during my undergraduate and graduate studies in Iran. I started my graduate program at NCSU physics department in 2014, where I had the opportunity to learn from some of the greatest physicists of our time, such as Prof. David Aspnes and later on had the privilege of working with Prof. Franky So, one of the most prominent scientists and a pioneer in organic electronics.

In Prof. So's lab I worked on two main issues concerning organic light emitting diodes (OLEDs): 1. Refractive index in OLEDs and 2. Electroluminescence at sub-bandgap voltages in OLEDs. My scientific contributions led to a patent and seven publications including three first

author papers. In August 2018 I had the honor of being the recipient of the Annual Physics Research Assistant Award of 2018.

ACKNOWLEDGMENTS

I would like to thank my adviser, Prof. Franky So, for his incredibly generous, kind and strong support during my entire program. As one of the early pioneers and most successful scholars in the field, his tireless and outstanding career in organic electronics has made it possible for our group to carry-out research and further advance and push the boundaries of the field.

I would like to thank the Physics Director of Graduate Program, Prof. David Aspens. His teaching in electrodynamics gave me a tremendous advantage in my research on optics of OLEDs. Moreover, the technology he invented and developed, Spectroscopic Ellipsometry, was crucial to my research.

I would like to thank Prof. Daniel Dougherty. I made my first OLED device in Prof. Dougherty's lab. He was incredibly generous and kind to me, and later with his support and recommendation I was able to join Prof. So's team.

I would like to thank my group-mates who tirelessly worked side-by-side with me, Samuel, Ying, Cheng, Erik, Xueping, Jaime, Chen, Dong Hun, Bhoj, Parand, Lei Lei, Laura, Juliana, Jason, Sean, Stephen, Nilesh, Monica, Mason, Carr, Qi.

TABLE OF CONTENTS

LIST OF TABLES	x
LIST OF FIGURES	xi
CHAPTER 1: Introduction to Organic Light Emitting Diodes (OLEDs)	1
1.1. Introduction	1
1.2. Organic Molecular Solids.....	1
1.3. OLED Physical Structure: Materials.....	2
1.4. OLED Methods of Fabrication.....	3
1.5. Charge Injection into Organic Semi-Conducting Materials.....	4
1.6. Exciton Formation and Energy Transfer in Organic Molecular Solids	5
1.7. Fluorescent OLEDs	7
1.8. Phosphorescent OLEDs.....	8
1.10. OLED Electronic Design Rules	9
1.10.1. Ohmic Contacts:	9
1.10.2. Charge balance:	10
1.10.3. Exciton confinement:.....	11
1.11. OLED Optical Design Rules	11
1.11.1. Extraction of Substrate Trapped Light	12
1.11.2. Extraction of Waveguide Trapped Light.....	13
1.11.3. Suppression of Evanescent Loss	14
1.12. Optical Simulations of OLED Cavity	14
1.12.1. A dipole Near a Metal-Dielectric Interface.....	16
1.12.2 Surface Plasmon Polariton	17
1.12.3 Mode Analysis.....	18
1.12.4 Emitter Dipole Orientation.....	20
1.13 Conclusions	22
CHAPTER 2: Suppressing evanescent loss using low refractive index electron transport layer	24
2.1. Abstract	24
2.2. Introduction	24
2.3. Crosslinkable Hole Transporting Layer in Solution-processed OLED.....	26
2.4. Design of the High Efficiency TADF OLED.....	27
2.5. Optimized Devices Using Conventional Electron Transporting Layers	27

2.6. Optimized Devices Using 3TPYMB as Electron Transporting Layers	29
2.7. Difference in Thicknesses of the Two ETLs.....	31
2.8. Measuring Refractive Index of Electron Transport Layers.....	33
2.9. Optical Simulations	34
2.9.1. Suppression of Evanescent Loss Following the SPP Dispersion Equation.....	34
2.9.2. Optical Simulations: Suppression of Evanescent Loss Following the Fermi's Golden Rule	37
2.9.3 Optimized Device.....	39
2.10. An Opto-Electronic Interplay.....	41
2.11. Conclusions	42
2.12. Experimental Section	43
CHAPTER 3: Manipulating Refractive Index in Organic Light Emitting Diodes	45
3.1. Abstract	45
3.2. Introduction	45
3.3. Oblique Angle Deposition (OAD)	46
3.4. Fabrication of Porous Low Refractive Index OAD Films	47
3.5. Effect of Refractive Index of Each Individual layer in an OLED Device	48
3.5.1. All Layers Having the Same Refractive Index.....	49
3.5.2. Electron Transporting Layer's Refractive Index.....	50
3.5.3. Transparent Anode (ITO) Layer's Refractive Index.....	50
3.5.4. Hole Transporting Layer's Refractive Index.....	51
3.5.5. Emissive Layer's Refractive Index	51
3.6. Effect of Anisotropy in Refractive Index.....	52
3.6.1 Birefringence in Organic Thin Films	52
3.6.2 Origins of Birefringence.....	53
3.6.3 Anisotropy and Light Extraction in OLEDs.....	54
3.7. Ultra-Low Refractive Index Organic Layers using Oblique Angle Deposition.....	56
3.7.1. Characterization of Porous Alq3 films Deposited using Oblique Angle Deposition.....	57
3.7.2. Formation of Wetting Layer	59
3.7.3. Oblique Angle Deposition of Other Organic Thin Films.....	60
3.8. Optimized OLED Multilayer	61
3.9. Refractive Indices of Common Materials Used in OLED Devices	63
3.10. Optical Simulation of Experimentally Fabricated Devices.....	64

3.10.1 Power Dissipation Calculations.....	64
3.10.2. Transvers Magnetic Modes	66
3.10.3. Transvers Electric Modes	67
3.10.4. Mode Distributions of Power Dissipation	68
3.10.5. Validation of Effect of Low Index ETL in Electroluminescent Spectra	69
3.11. Conclusions	70
3.12. Experimental	71
CHAPTER 4: Hyper-Fluorescent OLEDs with Sub-bandgap Operating Voltages.....	72
4.1. Abstract	72
4.2. Introduction	72
4.2.1. Catastrophic Failure of Blue Phosphorescent and TADF OLEDs	72
4.2.2. Band-gap Energy “Requirement” for Exciton Formation in Organic Solids	73
4.2.3. This Work’s Breakthrough	73
4.2.4. Triplet-Triplet Annihilation (Triplet-Fusion)	74
4.2.5. Exciplex Assisted Triplet-Fusion	75
4.3. Results and Discussion.....	76
4.3.1. The Hyper-Fluorescent OLED with Sub-Bandgap Operating Voltage.....	76
4.3.2. Structure of the Multilayer Hyperfluorescent Device	77
4.3.3. Guidelines for Choosing the Emitter and Host Molecules	77
4.3.4. Anthracene-based Host with Small Triplet Energy.....	78
4.3.5. Horizontally Oriented Emitter with P-type Delayed Electroluminescence.....	78
4.3.6. Investigation of Exciplex Formation	80
4.3.7. Single-layer OLEDs	86
4.3.8. Examining Other Wide-Bandgap Organic Semiconductors.....	90
4.3.9. Examining Narrow-Bandgap Organic Semiconductors: Rubrene	93
4.3.10. Direct Formation of Triplet Excitons by Charge Injection	97
4.3.11. Exciton Formation and Energy Transfer in the Multilayer Device.....	97
4.3.12. A Perturbation Approach to Singlet-Triplet State Mixing	102
4.3.13. TF vs. non-TF Host	105
4.3.14. This Work’s Hyper-Fluorescent OLED vs. Literature’s Best Phosphorescent and TADF OLEDs.....	106
4.4. Conclusion.....	107
4.6. Experimental	108
CHAPTER 5: Future Work and Outlook	112

5.1. Electro-Optical Correlations in Organic Solids	112
5.2. Degradation-Optical Correlations in Organic Solids	112
5.3. Exploiting Optical Anisotropy	113
5.4. Pushing the Efficiency Limit of Triplet-Fusion OLEDs	113
5.4.1 Quantification of Triplet-Fusion Contribution	113
5.4.2 The Efficiency Limit of Triplet-Fusion OLEDs.....	114
5.4.3 Developing New Materials for Triplet-Fusion OLEDs.....	114
REFERENCES	115

LIST OF TABLES

Table 2.1. Device performance summary.....	32
Table 2.1. Refractive indices of different ETLs at 550nm	33
Table 3.1. Refractive indices of some of commonly used materials in OLED devices at 550nm.....	63
Table 4.1. Materials studied in single-layer OLEDs. The OLED structure for all the devices is ITO/PEDOT (30 nm) / Material (40 nm) / Cs ₂ CO ₃ (1 nm) / Aluminum (100 nm), except for rubrene. Rubrene device structure was ITO / PEDOT (30 nm) / Rubrene (40 nm) / Aluminum (100 nm).....	101
Table 4.2. Comparing performance of my optimized device with some of the best TADF and phosphorescent OLEDs with similar color coordinates reported in literature. my device has the highest power efficiency at a luminance of 500 cd/m ² and larger, compared to all other devices shown in the table. N/R stands for not-reported.....	107

LIST OF FIGURES

Figure 1.1. The "acenes", simple organic molecular solids, by increasing the conjugation length of the molecule the absorption (emission) of the molecule shifts toward the red, with benzene having an absorption peak of 254 nm and Pentacene having an absorption of 582 nm. These simple organic molecules can be treated as a two-dimensional quantum well. As the length of quantum well increases the energy eigen-values decreases leading to a red shift in photoemission.....	2
Figure 1.2. Schematic of a bottom-emitting OLED physical structure, and materials. ETL stands for electron-transporting-layer, EML stands for emissive-layer and HTL stands for hole-transporting layer.	3
Figure 1.3. Conventional understanding of electron/hole charge injection into the LUMO/HOMO of organic solids in an OLED device. ETL stands for electron-transporting-layer, EML stands for emissive-layer and HTL stands for hole-transporting layer.	5
Figure 1.4. Exciton formation mechanism in organic thin films. a) Electron and hole pair are injected into the HOMO-LUMO levels. b) Exciton forms once the Coulomb potential of the electron-hole pair reaches room temperature KT , which is about 20meV. c) singlet and triplet exciton energies split from one another as the electron and hole pair approach further.....	7
Figure 1.5. a) Schematic of light propagation and loss channels in a generic bottom emitting OLED. Radiation can couple to the lossy surface plasmon polaritons (SPP) on the cathode, or it can be lost to the absorption of metal contact. After the critical angle, $\theta_c = \sin^{-1} n_{\text{substrate}}$, for substrate-air boundary, radiation is totally internally reflected into the substrate, called substrate-guided (SG) mode. After the critical angle for ITO-substrate boundary $\theta_c = \sin^{-1} n_{\text{substrate}}/n_{\text{ITO}}$, radiation is totally internally reflected into the ITO layer, called waveguide (WG) mode. b) Optical mode distribution of the OLED stack shown in a) as a function of emitter's distance from cathode. Strong interference of the emitter with itself dominates OLED's optical characteristics.	12
Figure 1.6. Using a semi-hemispherical lens on top of the substrate, all of the substrate-trapped light will be extracted.	13
Figure 1.7. Radiative excitons can be treated as damped driven radiative dipoles, these damped dipoles are driven by the reflected electromagnetic field from the metallic cathode (bottom of figure). The dipoles can have both radiative and non-radiative decay rates depending on the photoluminescence quantum yield of the emitter. The radiative decay rate can be influenced by the dipole moment orientation with respect to the substrate plane (θ), emitter distance from metallic electrode (h) and the cavity length (d).....	15

Figure 1.8. The calculated dipole radiation (power dissipation) can be categorized in four different regions depending on the magnitude of the inplane wave vector of the radiation: region 1, indicates the radiation that leaks to the ambient, and is so called “air-mode”. Region 2 indicates the “substrate-mode”. Regions 3 and 4 indicate the “waveguide-mode “and “evanescent-mode” respectively. Emitter dipole orientation and distance from the metal can heavily affect radiation coupling into surface plasmon polaritons and the evanescent-mode contributions. c) An example of optical-mode-distribution calculated from power dissipation results.....	20
Figure 1.9. Effect of dipole orientation on mode-contribution in an OLED device. Vertically aligned dipole moments strongly couple to the surface plasmon polaritons and have significant loss in the evanescent region.	22
Figure 2.1. Molecular structures of materials used.....	27
Figure 2.2. Characteristics of devices using T2T and NBphen, with different emitter concentrations. (EML concentration optimization).....	28
Figure 2.3. Characteristics of devices using T2T and NBPhen, with different NBPhen thicknesses. (ETL thickness Optimization).....	28
Figure 2.4. Characteristics of devices using 3TPYMB, with different 3TPYMB thicknesses. (ETL thickness Optimization).....	29
Figure 2.5. Characteristics of devices using 3TPYMB, with different emitter concentrations. (EML concentration optimization).....	30
Figure 2.6. The performance of device A and device B: A) Current density -Voltage-Luminance (J-V-L) characteristics. B) The electroluminescence (EL) spectra. C) Device energy band diagram. D) EQE vs. Luminance.	30
Figure 2.7. Simulation of normalized electroluminescence intensity versus ETL thickness for five different refractive indices of ETL. Maximum intensity happens at smaller ETL thicknesses for larger ETL refractive indices.	32
Figure 2.8. Measured refractive index of: a) T2T, showing positive in-plane birefringence. b) NBPhen, showing negative in-plane birefringence. c) 3TPYMB, showing an isotropic low refractive index. d) All measured refractive indices at $\lambda=550\text{nm}$. All refractive indices were measured using a spectroscopic ellipsometer and fitted to a uniaxial Cauchy model in transparent region.	34
Figure 2.9. Power dissipation as a function of normalized in-plane wave-vector for six different refractive indices of ETL. The area under the curve in first region indicates the amount of light escaping to air (air-mode). The area under the curve in second region indicates the amount of light trapped in substrate (substrate-mode). The area under the curve in third region indicates the	

amount of light trapped in waveguide (waveguide-mode). The area under the curve in fourth region indicates the amount of power lost to SPPs (evanescent-mode). Lower refractive index for ETL, shifts the SPP peak from larger normalized inplane wave-vectors to smaller, resulting in less loss in the evanescent region. Here ETL thickness is assumed to be 50nm.....	36
Figure 2.11. Power dissipation as a function of normalized in-plane wave-vector for six different thicknesses of ETL at 550nm. The area under each curve to the right of the black dashed line indicates the amount of power lost to the SPPs. Here refractive index of ETL is assumed to be 1.65	38
Figure 2.12. Percentage of power that is coupled to SPP (evanescently coupled) and to substrate (substrate + air-mode) as a function of ETL thickness. Increase in the thickness of ETL will result in more light out-coupling to air and substrate at expense of less power loss to SPPs (evanescently coupled). Contribution of each mode is calculated based on the power dissipation shown in Figure 2.11.	39
Figure 2.13. a) and b) Mode power contributions of Device A and Device B respectively. * Other loss channels include substrate modes, waveguide modes. Inset shows the corresponding device structure used in calculation. c) and d) Spectral power dissipation as a function of normalized in-plane wave-vector for Device A and Device B respectively. The region indicated by red double arrow is out-coupled to substrate and air, and the region indicated by blue double arrow is evanescent, the region between the two dashed lines is coupled to wave-guide mode.	40
Figure 2.14. Effect of refractive index of UT-314 and EML on light extraction. Refractive index of UT314 has a small effect (<5%) on light extraction while assuming larger refractive index for EML will result in more light extraction.	44
Figure 3.1. Schematic of Oblique Angle Deposition. A substrate is positioned at an oblique angle with respect to a collimated vapor flux. Upon initial islanding, a self-shadowing leads to an ordered porous columnar growth. The degree of porosity can be tuned by self-shadowing and therefore the angle which substrate makes with the vapor flux.....	47
Figure 3.2. Demonstrating ordinary, <i>no</i> , and extraordinary, <i>ne</i> , components of refractive index with respect to substrate.	52
Figure 3.3. On the left, a schematic of top view of an anisotropic organic film, with negative birefringence, due to rod-shape geometry of organic molecule, is displayed. On the right, side-view (cross-section) of the film is illustrated. Organic molecules are represented as rod-shaped “sticks”, with the molecular axis being along the “stick”.	53

Figure 3.4. Both TE and TM polarized modes propagate in plane of the substrate (slab), i.e. have their k vector in plane of the slab. However, the electric field component of the TE-polarized radiation lies in the plane of the substrate, making a complete overlap with the ordinary component of refractive index and normal to the extraordinary component of refractive index, while TM-polarized radiation is normal to the ordinary refractive index and overlaps completely with the extraordinary refractive index.	54
Figure 3.5. Distribution of intensity of lossy modes in a conventional OLED stack. TM-polarized modes, including SPP and TMWG ₀ are mainly distributed near the metal cathode, therefore it is expected for refractive index of ETL to have the largest impact on TM-polarized modes. Since TM-polarized modes have their electric field normal to the plane of the substrate, as shown in figure 3.4, the extraordinary component of ETL is expected to have much larger impact on the modes rather than the ordinary component of the ETL's refractive index. TEWG ₀ mode is mainly distributed in the HTL and ITO layer, and therefore refractive index of HTL and ITO is expected to mainly influence this mode. Since TE-polarized modes have their electric field parallel to the plane of the substrate, as shown in figure 3.4, it is expected for the ordinary refractive index of ITO and HTL to have much larger impact on light-extraction, rather than the extraordinary refractive index of the two layers. The mode distributions above is calculated using Lumerical software.	55
Figure 3.6 Calculated Air, η_A , contribution as a function of ordinary and extraordinary refractive indices of a birefringent: a) ETL, and b) HTL. Calculated Air+Substrate η_{A+S} contribution as a function of ordinary and extraordinary refractive indices of a birefringent: c) ETL, and d) HTL.	56
Figure 3.7 Cross-sectional SEM image of the sample used for ellipsometry measurement. Substrate is a 1mm thick Si wafer with 300nm of thermal oxide layer. A 200nm thick solid Alq3 film at 0 degrees is first deposited to measure the refractive index of the solid Alq3 film. Then a 700nm thick Alq3 layer is deposited at 80 degrees on top of the solid Alq3 film to measure the refractive index of the porous Alq3 film. A Bruggeman Effective Medium Approximation (BEMA) model using the refractive index of the solid Alq3 layer and void is used to find the refractive index of the porous film.	58
Figure 3.8 a) Optical constants of Alq3 film deposited at 80°. b) Optical constants of Alq3 deposited normally. c) Refractive index of Alq3 deposited thin films as a function of angle of deposition at 525nm, from ref. [92] d) Cross sectional SEM image of ~ 600nm of Alq3 deposited at 80° on top of 90nm B3PYMPM deposited at 0° on top of 300nm of SiO ₂	59
Figure 3.9 a) Dispersive refractive index and extinction coefficient of some of isotropic materials used in OLED devices. b) Dispersive ordinary	

refractive index and extinction coefficient of some of birefringent materials used in OLED device. c) Dispersive extraordinary refractive index and extinction coefficient of some of birefringent materials used in OLED devices.	62
Figure 3.10. Device characteristic of OAD Device and Control Device.	64
Figure 3.11. a) Power dissipation as a function of refractive index of the ETL and in-plane wavevector, at $\lambda=525\text{nm}$. Region 1 presents “air-mode”, region 2 presents “substrate-mode”, region 3 presents “waveguide-mode” and region 4 presents “evanescent-mode”. b) Relative mode contribution calculated from the power dissipation. The star marks indicate the experimental maximum EQE achieved by OAD Device and Control Device. The calculations are based on the structure of OAD Device and Control Device. The refractive index of the last 40nm of the ETL (Alq3) layer was varied from 1.4 to 2.	66
Figure 3.12. TE-polarized power dissipation vs. in-plane wavevector as a function of ITO refractive index.	68
Figure 3.13. A) Experimental electroluminescence spectrum obtained from OAD Device and Control Device. B) Simulated electroluminescence spectrum of OAD Device and Control Device.	69
Figure 4.1. a) Energy transfer schematic and mechanism of previously reported OLEDs with electroluminescence at sub-bandgap voltages. Upon the formation of the low energy CT-exciton, the energy is transferred to the triplet exciton of the emitter via Dexter energy transfer (ET). The triplet excitons on the emitter will then undergo fusion and excite a radiative singlet exciton through energy up-conversion b) and c) show two examples of OLED devices with sub-band gap electroluminescence. In the Rubrene device the CT-exciton forms between Rubrene and C60 and then transfers to the triplet of the rubrene. In the ADN device the CT-exciton forms between ADN and m-MTDATA and then transfers to the triplet exciton of the ADN molecule.	76
Figure 4.2. Ordinary and extraordinary extinction coefficient of BCzVBi thin film. I calculated the dipole orientation of BCzVBi in pure film, using the order parameter calculated from the equation: $S = \frac{k_{\text{max}} - k_{\text{omax}}}{k_{\text{max}} + 2k_{\text{omax}}} = 3\theta - 12$, where θ indicates the ensemble average of vertically oriented transition dipole moments. The film showed $\theta = 0.101$ or 89.9% horizontal orientation of dipole moments.	79
Figure 4.3. a) Overlap between absorption (extinction coefficient) of BCzVBi and PL and EL emission of CzPA, indicates efficient Förster energy transfer from singlet state of CzPA to the singlet state of BCzVBi. b) Device structure of	

the device corresponding to the EL spectrum of pure single-layer CzPA device shown in a).	79
Figure 4.4. Device Characteristics: a) Device structure. b) JVL graph. c) Electroluminescent spectrum. d) External quantum efficiency. e) Power efficiency.	80
Figure 4.5. OLED device structure and the electroluminescent spectra of the optimized device at different voltages. A low energy exciplex emission would dominate the EL spectra specially at low voltages. Lack of change in the EL spectra as a function of voltage refutes existence of any exciplex state.	81
Figure 4.6. Device structures and characteristics of OLEDs with a thin layer of pure host (CzPA) or emitter (BCzVBi) at the HTL (TAPC) or ETL (BPhen) interfaces.	82
Figure 4.7. Device structures and characteristics of OLEDs with pure host (CzPA) or emitter (BCzVBi) at the HTL (TAPC) or ETL (BPhen) interfaces.	83
Figure 4.8. Device structure and EL spectra at different voltages of the OLED device made of pure BCzVBi EML between TAPC and BPhen.	84
Figure 4.9. Device structure and EL spectra at different voltages of the OLED device made of pure BCzVBi/CzPA bilayer EML between TAPC and BPhen.	84
Figure 4.10. Device structure and EL spectra at different voltages of the OLED device made of pure CzPA/BCzVBi bilayer EML between TAPC and BPhen.	85
Figure 4.11. Device structure and EL spectra at different voltages of the OLED device made of pure CzPA EML between TAPC and BPhen.	85
Figure 4.12. a) Device current density and photocurrent versus bias voltage. Two detectors were used to detect the electroluminescence; a photomultiplier tube (PMT) was used for low light intensities and a Si-photodiode was used for higher light intensities (due to PMT saturation). The photocurrent corresponding to a luminance of 0.1 cd/m ² is marked on the graph. b) Molecular structure of BCzVBi and device structure of the OLED with a single-layer of BCzVBi. c) Electroluminescent (EL) spectra of the device. d) Photocurrent vs. current density in the low voltage region showing a quadratic behavior, which is indicative of emission due to triplet-fusion, “quadratic regime”. e) Photocurrent vs. current density in the high voltage region showing a normal linear behavior, “linear regime”. f) Transient EL dynamic of the device after turn-off shows microsecond scaled delayed fluorescence which is indicative of fluorescence due to triplet-fusion. A reverse bias of -5.0 volts was applied at the onset of turn-off.	87
Figure 4.13. Device structure of the BCzVBi single-layer device and its EL spectra at different voltages.	88

Figure 4.14.a) Device current density and photocurrent versus bias voltage. The photocurrent corresponding to a luminance of 0.1 cd/m^2 is also marked on the graph. b) Molecular structure of CzPA and the device structure of the OLED with a single-layer of CzPA. c) Electroluminescent (EL) spectra of the device at 2.8 volts. d) Photocurrent vs. current density in the low voltage region showing a quadratic behavior, which is indicative of emission due to triplet-fusion, “quadratic regime”. e) Photocurrent vs. current density in the high voltage region showing a normal linear behavior, “linear regime”. f) Transient EL dynamic of the device after turn-off shows microsecond scaled delayed fluorescence which is indicative of fluorescence due to triplet-fusion. A reverse bias of -5.0 volts was applied at the onset of turn-off.89

Figure 4.15. Device structure of the CzPA single-layer device and its EL spectra at different voltages.90

Figure 4.16.a) Device current density and photocurrent versus bias voltage. Two detectors were used to detect the electroluminescence; a photomultiplier tube (PMT) was used for low light intensities and a Si-photodiode was used for higher light intensities (due to PMT saturation). b) Molecular structure of BDAVBi and the device structure of the OLED with a single-layer of BDAVBi. c) Electroluminescent (EL) spectra of the device. d) Photocurrent vs. current density in the low voltage region showing a quadratic behavior, which is indicative of emission due to triplet-fusion, “quadratic regime”. e) Photocurrent vs. current density in the high voltage region also showing a quadratic behavior. f) Transient EL dynamic of the device after turn-off shows microsecond scaled delayed fluorescence which is indicative of fluorescence due to triplet-fusion. A reverse bias of -5.0 volts was applied at the onset of turn-off.91

Figure 4.17.a) Device current density and photocurrent versus bias voltage. b) Molecular structure of TBADN and the device structure of the OLED with a single-layer of TBADN. c) Electroluminescent (EL) spectra of the device. d) Photocurrent vs. current density in the low voltage region showing a quadratic behavior, which is indicative of emission due to triplet-fusion, “quadratic regime”. e) Photocurrent vs. current density in the high voltage region also showing a quadratic behavior. f) Transient EL dynamic of the device after turn-off shows microsecond scaled delayed fluorescence which is indicative of fluorescence due to triplet-fusion. A reverse bias of -5.0 volts was applied at the onset of turn-off.92

Figure 4.18. Device current density and photocurrent versus bias voltage. b) Molecular structure of DMPPP and the device structure of the OLED with a single-layer of DMPPP. c) Electroluminescent (EL) spectra of the device. d) Photocurrent vs. current density in the low voltage region showing a quadratic behavior, which is indicative of emission due to triplet-fusion, “quadratic regime”. e) Photocurrent vs. current density in the high voltage

region also showing a quadratic behavior. f) Transient EL dynamic of the device after turn-off shows microsecond scaled delayed fluorescence which is indicative of fluorescence due to triplet-fusion. A reverse bias of -5.0 volts was applied at the onset of turn-off.93

Figure 4.19. a) Device current density and photocurrent versus bias voltage. Two detectors were used to detect the electroluminescence; a photomultiplier tube (PMT) was used for low light intensities and a Si-photodiode was used for higher light intensities (due to PMT saturation). The photocurrent corresponding to a luminance of 0.1 cd/m² is also marked on the graph. b) Molecular structure of rubrene and the device structure of the OLED with a single-layer of rubrene. c) Electroluminescent (EL) spectra of the device. d) Photocurrent vs. current density in the low voltage region showing a quadratic behavior, which is indicative of emission due to triplet-fusion, “quadratic regime”. e) Photocurrent vs. current density in the high voltage region also showing a quadratic behavior. f) Transient EL dynamic of the device after turn-off shows microsecond scaled delayed fluorescence which is indicative of fluorescence due to triplet-fusion. A reverse bias of -5.0 volts was applied at the onset of turn-off.95

Figure 4.20. Current density as a function of voltage of rubrene single-layer OLEDs, when cathode is bare aluminum, LiF (1nm) /Aluminum or Cs2CO3/Aluminum.96

Figure 4.21. a) Direct triplet exciton formation in single-layer devices with the structure ITO/PEDOT/Emitter/Cathode. Once holes are injected into the HOMO of the emitter, triplet excitons would form directly without injection of the electrons to the LUMO level. Therefore, the onset of electroluminescence would be the required energy for the triplet exciton plus the Schottky barrier for the hole injection into the HOMO of the emitter. b) Direct triplet exciton formation on BCzVBi molecule, in CzPA:BCzVBi EML placed between TAPC and BPhen as HTL and ETL respectively. Once holes are injected into the HOMO of CzPA they will transfer to the HOMO of the BCzVBi and then the electrons directly form triplet excitons without injection to the LUMO of BCzVBi. c) Energy transfer mechanism and interaction between CzPA and BCzVBi. At sub-bandgap voltages. Triplet excitons are initially formed on BCzVBi molecules, they can then, either directly undergo fusion and create a radiative singlet exciton on BCzVBi or they can diffuse to the triplet state of CzPA via Dexter energy transfer (ET). The triplet excitons on CzPA then undergo fusion and create a radiative singlet exciton on CzPA, which will transfer its energy to the singlet state of BCzVBi via Forster energy transfer (ET), due to the overlap between CzPA’s emission and BCzVBi’s absorption. The triplet excitons on BCzVBi and CzPA can also have hetero-fusion which would further enhance emission due to triplet fusion.99

Figure 4.22.a) Voltage-Current Density-Photocurrent of the optimized device, using Si-Photo diode and PMT. The onset of the electroluminescence occurs at 2.1 volts, similar to the BCzVBi single-layer device, indicating that triplet excitons first form on BCzVBi at sub-bandgap voltages. b) Device structure of the optimized device.	100
Figure 4.23.Spectral change in absorption coefficient as a function of applied bias for a) Device A with structure ITO/MoOx/BCzVBi/Al and b) Device B with structure ITO/BPhen/BCzVBi/LiF/Al.....	104
Figure 4.24.Comparison between the device using CBP as host vs the optimized device using CzPA as host. a) and b) Device structures. c) JVL characteristic of the devices, while the device using CzPA as host has a turn-on voltage of 2.4 volts, the device using CBP has a turn-on voltage of 3.8 volts. d) and e) and f) EL spectra, EQE and power efficiency of the devices.....	106
Figure 4.25.Phosphorescent spectra of the molecules studied in this work recorded at 77K. Molecular triplet energies were experimentally estimated via the phosphorescence spectra.	110
Figure 4.26.Photoluminescence (red) and absorption (black) spectra of the molecules used in this study. Molecular singlet energies were estimated from the absorption and emission spectra.....	111

CHAPTER 1

CHAPTER 1: Introduction to Organic Light Emitting Diodes (OLEDs)

1.1. Introduction

Organic light emitting diodes have been widely commercialized in the past three decades. Ultra-thin structure, self-emitting pixels, transparent and flexible panels are some of the extraordinary features of OLED displays that distinguishes them from other display technologies such as LCDs. With the continuously improving technology and better performances, OLED displays are deemed to overtake the display market, with a current market value of \$50 billion USD.

1.2. Organic Molecular Solids

Organic molecular solid is a term which describes, solids such as crystals or amorphous film made of organic molecules. Organic molecules are, compounds with a large carbon presence which can also include elements such as N, O, S, Se, etc. [1] In organic molecular solids, due to sp^2 hybridization of carbon-carbon bonds, a delocalized cloud of electrons is formed above and below the plane of the molecule. The delocalized electron clouds, or π orbitals, form the frontier orbitals of the molecular solid, that is: the highest occupied molecular orbital (HOMO) and the lowest unoccupied molecular orbital (LUMO), with a bandgap of a few eV. [1] Therefore Organic

molecules can absorb and luminesce in visible, UV and IR regions of spectra. Examples of some organic molecular solids are shown in Figure 1.1.

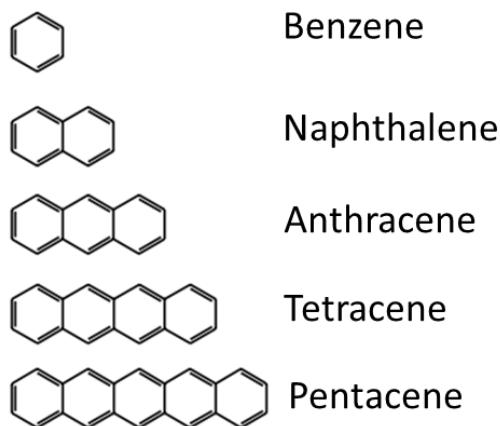


Figure 1.1. The "acenes", simple organic molecular solids, by increasing the conjugation length of the molecule the absorption (emission) of the molecule shifts toward the red, with benzene having an absorption peak of 254 nm and Pentacene having an absorption of 582 nm. These simple organic molecules can be treated as a two-dimensional quantum well. As the length of quantum well increases the energy eigen-values decreases leading to a red shift in photoemission.

1.3. OLED Physical Structure: Materials

An organic light emitting diode (OLED) consists of an active organic multilayer, made of organic thin films, which is sandwiched between a transparent electrode and a reflecting electrode. The transparent electrode is usually a transparent conductive oxide such as Indium Tin Oxide (ITO), and the reflecting metallic electrode is usually aluminum or silver. The organic multilayer is usually comprised of three main layers of organic solids: a hole transporting layer (HTL), an emissive layer (EML) and an electron transporting layer (ETL). A generic schematic of an OLED

structure, and examples of materials used, is demonstrated in Figure 1.2. The entire thickness of an OLED multilayer device is in the range of 50nm to 300nm, excluding the substrate.

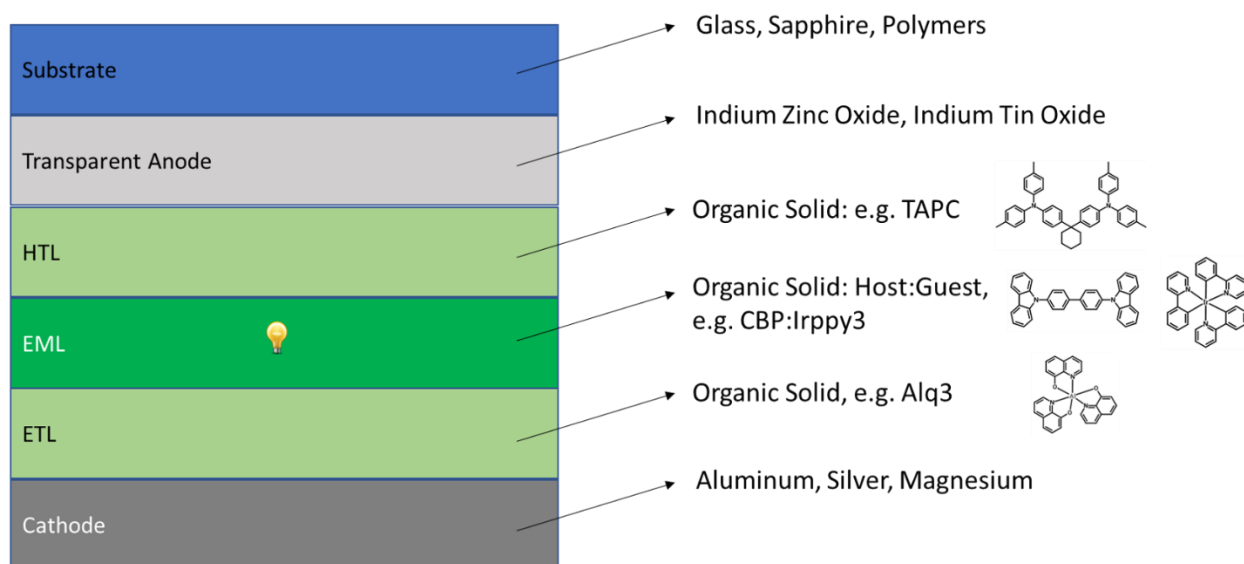


Figure 1.2. Schematic of a bottom-emitting OLED physical structure, and materials. ETL stands for electron-transporting-layer, EML stands for emissive-layer and HTL stands for hole-transporting layer.

1.4. OLED Methods of Fabrication

OLEDs can be fabricated using two main methods: 1. Solution-processing 2. Organic molecular beam deposition (vacuum deposition).

Solution processed OLEDs are mainly fabricated using spin-casting. First solutions, for each specific layer, are prepared by dissolving powder form of organic molecules in orthogonal solvents, and then they are sequentially spin casted. Spin casted layers may be cured or treated for solidification. In general solution processed OLEDs lack in performance and operational lifetime compared with vacuum evaporated OLEDs, due to increased electronic disorder, impurities, and material diffusion at the layer interfaces.[2][3]

Organic molecular beam deposition, is a physical vapor deposition (PVD) method, in which organic materials in powder form are placed inside a thermal boat in a high vacuum chamber

(pressure $< \sim 10^{-6}$ torr) and evaporated. The vapor flux then leads to thin film deposition of the material on a substrate, upon condensation. This method is the preferred method of fabrication for industrial applications of OLED devices.

1.5. Charge Injection into Organic Semi-Conducting Materials

Unlike inorganic semiconductors where there exists a valence/conduction band for hole/electron transport, organic semiconductors have highly localized HOMO/LUMO states and hole/electron transport in organic semiconductors happens through a phonon-assisted hopping mechanism. The localization of electronic states in organic semiconductors is mainly due Anderson localization,[4] since the electronic disorder is larger than the band-width.[5][6][7] Moreover electron-phonon interaction in the organic solids leads to an increased effective mass of the “dressed” polarons, further localizing the charge carriers.[8] The carrier hopping in organic solids is described via the Abraham-Miller tunneling probability between localized electronic states:

$$v = v_0 e^{-2\alpha R} \quad (1.1)$$

Where v_0 is attempt-to-escape frequency (rate), R is the distance between states, and α is the spatial decay of the electronic wavefunction. [9]

Electrons and holes can be injected into organic single molecule solids through ohmic contacts. Using a metal-organic junction, electrons can be injected into the Lowest Un-occupied Molecular Orbital or LUMO, and holes can be injected into the Highest Occupied Molecular Orbital or HOMO, through a thermally-assisted tunneling process.[8] HOMO/LUMO levels in organic semiconductors are analogous to valence/conduction bands in inorganic semiconductors. Although, the general understanding is that charge carriers can only be injected into the HOMO-

LUMO states of an organic semiconductor, as shown in Figure 1.3, it will be shown later at the last chapter of this dissertation, that carriers can readily be injected into sub-bandgap excitonic states of the molecules, such as triplet states, instead of HOMO/LUMO levels.

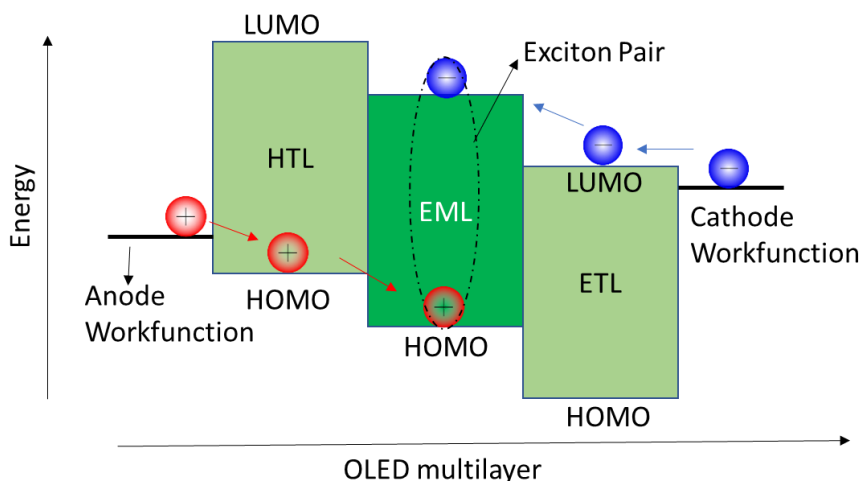


Figure 1.3. Conventional understanding of electron/hole charge injection into the LUMO/HOMO of organic solids in an OLED device. ETL stands for electron-transporting-layer, EML stands for emissive-layer and HTL stands for hole-transporting layer.

1.6. Exciton Formation and Energy Transfer in Organic Molecular Solids

After electron and hole are injected into the LUMO and HOMO of an organic molecular solid from two opposing electrodes, under the force of the electric field from the applied voltage, they move toward one another in the organic thin film. Electron-hole pair form an exciton pair once the attractive Coulomb potential between the two is in the order of room temperature KT , which happens at a distance of about $\sim 20\text{nm}$.^[10] The initially formed exciton, has the same degenerate energy for excitons with both triplet and singlet spin states, which is close to the HOMO-LUMO gap. As the electron-hole pair further approach each other and an overlap between the HOMO-LUMO orbitals appear, singlet and triplet exciton's energy levels split from one another, due to an increase in the exchange energy. When electron-hole pair reach the emitting

molecule, the exciton recombines and depending on the type of the emitter, recombination can either be radiative or non-radiative. Figure 1.4 displays different stages of exciton formation. More details on exciton formation will be discussed in chapter 4 of this dissertation.

Excitons can transfer energy through two main mechanisms, Forster energy transfer and Dexter energy transfer.[11] In Forster energy transfer, an exciton first emits a photon by recombination, and then the emitted photon excites another molecule and creates a new exciton. Forster energy transfer is long range and an overlap between the transmitting molecule's spectral emission and the receiving molecule's spectral absorption is required. Forster energy transfer only takes place between excitons with radiative spin states, i.e. singlet excitons in a fluorescent system. Dexter energy transfer is a collisional and non-radiative short range (~ 1 nm) energy transfer, that can also include non-radiative excitons, i.e. triplet excitons in a fluorescent system.

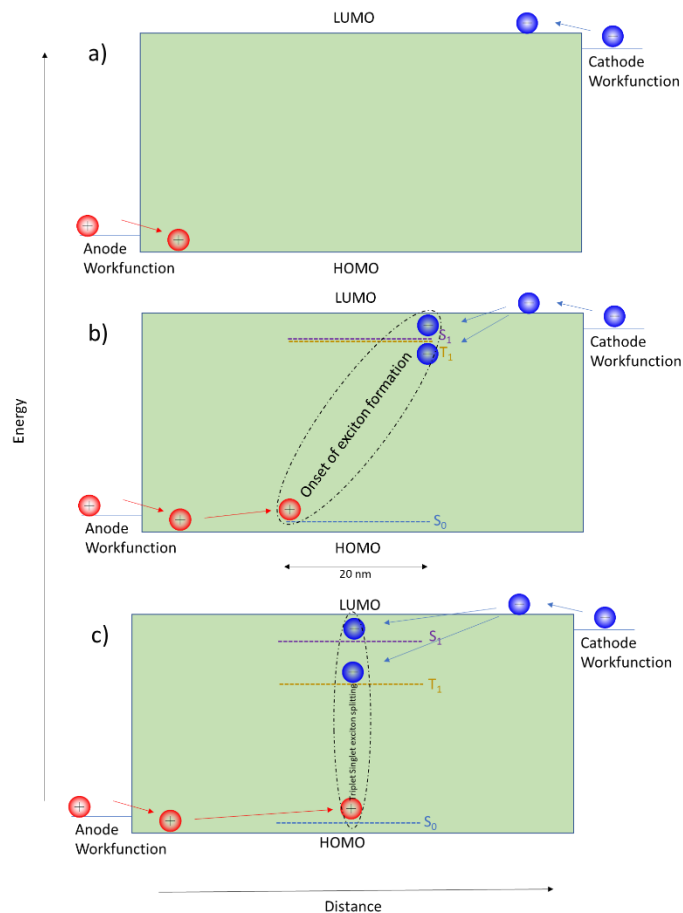


Figure 1.4. Exciton formation mechanism in organic thin films. a) Electron and hole pair are injected into the HOMO-LUMO levels. b) Exciton forms once the Coulomb potential of the electron-hole pair reaches room temperature KT , which is about 20nm . c) singlet and triplet exciton energies split from one another as the electron and hole pair approach further.

1.7. Fluorescent OLEDs

In a conventional organic fluorophore, only excitons with a singlet spin state can have a radiative recombination, because the ground state of all organic molecular solids has a total spin of zero, i.e. is a singlet. A transition of a triplet excited state to ground state is spin-forbidden. Radiation by recombination of singlet excitons is called fluorescence and it takes place within nano-seconds or with 10^9 Hz rate. When charge carriers are electronically injected through ohmic contacts, $\frac{3}{4}$ of electron-hole pairs (excitons) have a triplet spin state and $\frac{1}{4}$ of the excitons have a

singlet spin state, due to spin multiplicity. Fluorescent OLEDs, utilizing fluorescent fluorophores, have a maximum internal quantum efficiency (IQE) of 25%, since only 25% of injected carriers will form singlet excitons.

1.8. Phosphorescent OLEDs

Triplet excitons can have radiative recombination if the singlet and triplet spin states can be mixed by perturbation. One way to achieve the spin-mixing is by placing a heavy atom, such as Ir and Pt, in the molecular solid to induce strong spin-orbit-coupling (SOC).[12][13] Radiation by triplet excitons is called phosphorescence, which has a slower $\sim 10^6$ Hz rate compared to fluorescence. Phosphorescent OLEDs, utilizing phosphorescent emitters, can achieve 100% IQE.[14] Although phosphorescent OLEDs can achieve four times more efficiency compared to fluorescent OLEDs, they are costlier due to incorporation of heavy (rare-earth) metals. Moreover, for wide bandgap (blue) emitters phosphorescent emitters have a short operational lifetime which has rendered them impractical for real applications. The short operational life time of phosphorescent OLEDs is due to annihilative processes of the high energy triplet state of the emitter with itself, triplet-triplet-annihilation (TTA), or with polaronic states, triplet-polaron-annihilation (TPQ), which in turn results in dissociation of organic bonds by generation of “hot” excited states. [15][16][17][18]

1.9. TADF OLEDs

The energy states associated with singlet and triplet spin states have different energies or are “split” from one another (also called singlet-triplet splitting). The singlet-triplet splitting is a direct consequence of HOMO-LUMO orbital overlap or exchange energy. The larger the overlap

(exchange energy) the larger the splitting. By reducing the exchange energy through molecular design, the singlet-triplet splitting energy can be reduced to room temperature KT . When the energy difference between the two spin states is that small, triplet exciton can be converted to singlet excitons by reverse-intersystem-crossing (RISC). Electroluminescence in such systems is called E-type delayed fluorescence or Thermally Assisted (Activated) Delayed Fluorescence (TADF).[19] OLEDs, utilizing emitters with TADF property are called TADF OLEDs. Similar to phosphorescent OLEDs, TADF OLEDs can achieve an internal efficiency of 100%, but unlike phosphorescent OLEDs, TADF OLEDs lack the requirement for the expensive rare-earth metals,[20] which makes them more attractive. However, they too suffer from short operational lifetime for blue emitters. [21][22][23][24]

1.10. OLED Electronic Design Rules

To design an efficient OLED device, from an electronic prospective, the following design rules should be followed:

1.10.1. Ohmic Contacts:

It is imperative to select electrodes and transport materials that will form minimal Schottky barrier for electron/hole charge carriers. For the choice of cathode, aluminum, magnesium and silver are the most popular choices. A thin layer of lithium fluoride or cesium carbonate is deposited immediately under the cathode for better electron injection to decrease the cathode's work function and promote electron injection.[25][26] Indium tin oxide and indium zinc oxide are the popular choices for anode. UV-ozone treatment of ITO is usually used to increase ITO's work-function for better hole injection.[27]

1.10.2. Charge balance:

Organic electronic materials are known to have a larger hole mobility compared to electron mobility, which leads to an accumulation of hole polarons in the OLED device.[28] The excess of unpaired polarons leads to non-radiative recombination of the radiative excitons, due to annihilative processes, such as singlet-polaron-annihilation (STA) and triplet-polaron-annihilation (TPA), which leads to a decreased efficiency and material degradation.[29][11][16][17] Therefore, it is important to maintain charge-balance, in order to have maximum efficiency and operational lifetime.[30][31] To improve/adjust carrier mobilities, the transporting layers can be doped with n-dopands, such as cesium carbonate,[32] or p-dopands such as molybdenum oxide. The thickness of the transporting layers also naturally effects the transport of a charge carrier in a reverse manner. Therefore, the charge balance can be adjusted by either doping or tuning the thicknesses of the corresponding transport layers.

It is important to note that carrier charge mobility in organic solids is both temperature and field dependent, since the transport mechanism happens through a hopping process.[9] The carrier mobility dependence on temperature and field can be expressed in a so called “Pool-Frenkel” form:

$$\mu(E, T) = \mu_{\infty} \frac{\Delta_0 \beta_{PF} \sqrt{E}}{kT_{eff}} \quad (1.2)$$

here E is the electric field, $T_{eff}^{-1} = T^{-1} - (T')^{-1}$, Δ_0 , β_{PF} , T' and μ_{∞} are constantans. [1] In an OLED multilayer stack, field dependence of mobility is different for each individual layer and material,[1] meaning that charge balance cannot necessarily be maintained in the entire operational voltage range of the device, and efficiency roll-up or roll-off may occur in the luminance range of an OLED.

1.10.3. Exciton confinement:

1.10.3.1. Hole/Electron Blocking Layers

As we mentioned above, an exciton can diffuse and lose its energy by a Forster or Dexter energy transfer to a non-radiative channel. Therefore, it is important to confine the exciton to the emissive layer (EML) by selecting wide-bandgap materials as the neighboring transport layers.[33] A wide band-gap electron transporting layer would have a very deep HOMO relative to other layers and therefore sometimes is called a hole-blocking layer (HBL).[34] A wide band-gap hole transporting layer would have a very shallow LUMO relative to other layers and therefore is called an electron blocking layer (EBL). [35]

1.10.3.2. Choice of Host Matrix

In modern OLEDs, emitter is doped in a host matrix with a small ratio to avoid complications due to concentration quenching.[36] In such host-emitter systems, the host matrix should be selected in way to have emission spectral overlap with emitters spectral absorption, in order to have efficient Forster transfer from the host to the emitter.[37] Moreover, in TADF and phosphorescent OLEDs, the host material should have a larger triplet energy compared to the emitter's triplet energy to avoid non-radiative quenching via Dexter energy transfer.[36][38]

1.11. OLED Optical Design Rules

Even with a 100% internal efficiency, i.e. all injected charge carriers producing photons, only a fraction of light leaves the OLED device, due to the optically lossy nature of an optical micro-cavity. More than half of generated light is lost to bound optical modes such as waveguide modes, surface plasmon polaritons and absorption.[39][20][40] A schematic of optical structure

of a bottom emitting OLED is demonstrated in Figure 1.5a. The light that is generated by the excitons in the EML can be lost to surface plasmon polaritons or metal absorption or it can be trapped either in the substrate or in the OLED cavity itself. Figure 1.5b displays optical mode distribution of the OLED shown in Figure 1.5a. Emitter's optical interference with itself dominates the optical characteristics of OLED, and therefore the distance between the emitter and the metallic reflector is the most important factor dominating the optical outcoupling, as it is shown in Figure 1.5b.

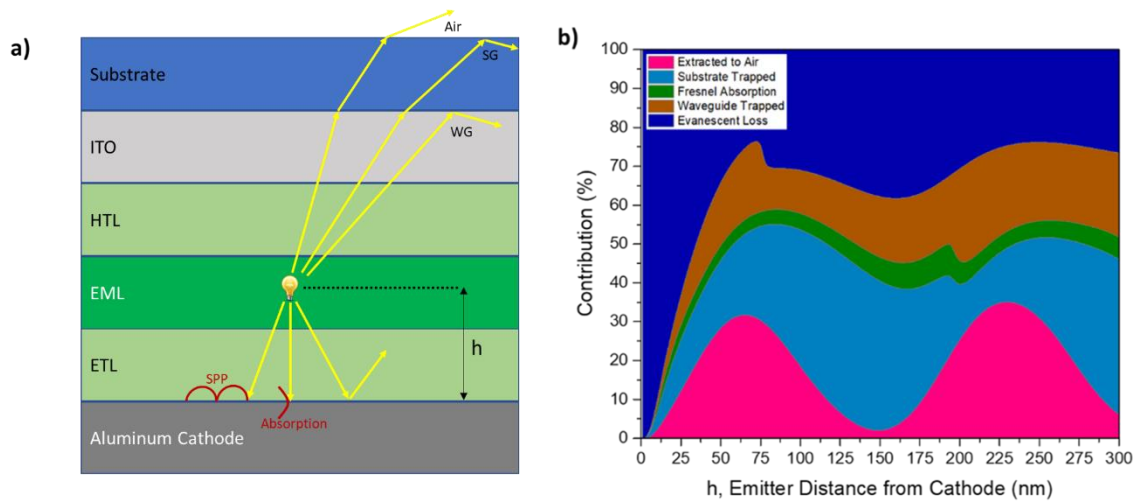


Figure 1.5. a) Schematic of light propagation and loss channels in a generic bottom emitting OLED. Radiation can couple to the lossy surface plasmon polaritons (SPP) on the cathode, or it can be lost to the absorption of metal contact. After the critical angle, $\theta_c = \sin^{-1} \frac{1}{n_{\text{substrate}}}$, for substrate-air boundary, radiation is totally internally reflected into the substrate, called substrate-guided (SG) mode. After the critical angle for ITO-substrate boundary $\theta_c = \sin^{-1} \frac{n_{\text{substrate}}}{n_{\text{ITO}}}$, radiation is totally internally reflected into the ITO layer, called waveguide (WG) mode. b) Optical mode distribution of the OLED stack shown in a) as a function of emitter's distance from cathode. Strong interference of the emitter with itself dominates OLED's optical characteristics.

1.11.1. Extraction of Substrate Trapped Light

Placing a semispherical lens with the same refractive index as substrate or creating a rough scattering structure or placing a micro-lens array on top of substrate, are some of the common

approaches to the extraction of the substrate guided light. Figure 1.6, shows a schematic of substrate light-extraction using a semi-hemispherical lens. [41][42]

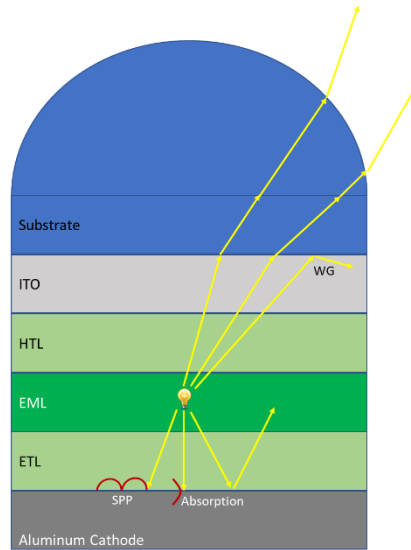


Figure 1.6. Using a semi-hemispherical lens on top of the substrate, all of the substrate-trapped light will be extracted.

1.11.2. Extraction of Waveguide Trapped Light

The most straight-forward method of extracting waveguide trapped light is with use of a high index substrate, such as sapphire with a refractive index equal or larger than the refractive index of the organic emissive layer. When using a high index substrate, the entire far-field radiation in the OLED cavity will enter the substrate, and the bound eigenmodes of the system will no longer exist, except surface plasmon polaritons. Substrate trapped light can then be extracted using substrate light extraction methods. Scattering structures can also be used to extract trapped waveguided light.[43][44][45]

1.11.3. Suppression of Evanescent Loss

Evanescent loss or near-field radiation of excitons in OLED, is coupled to surface plasmon polariton modes and lossy surface waves of the metallic electrode.[46] Within the structure of a conventional OLED device with the EML at least 50 nm apart from any metal layer, the evanescent loss is mainly due to exciton coupling with the SPP modes, and the surface lossy waves have a negligible contribution. As I will show in the next two chapter, the evanescent loss can be significantly reduced by employing a low refractive index electron transport layer.[20][40]

Here we should note that to achieve an OLED device with theoretical limit efficiency, both electronic and optical design rules should be followed in fabrication of an OLED device. For instance, an OLED device with perfect charge balance, ohmic contacts and exciton confinement will not work efficiently if the optical cavity is off-resonance and vice-versa.

1.12. Optical Simulations of OLED Cavity

The most prevalent method for optical simulation of OLEDs, is based on a classical dipole model, which was first introduced by Chance, Prock, and Silbey (CPS).[47][48] In this model excitons are treated as damped oscillators that are driven by a reflected electromagnetic field. The damped oscillators have both radiative and non-radiative decay rates, which is mainly determined by the photoluminescence quantum yield (PLQY) and the radiative mechanism of the emitter e.g. fluorescence, phosphorescence, delayed fluorescence, etc.[49][50] Parameters such as the distance of the dipole (emitter) from the metallic cathode (z in Figure 1.7), dipole orientation (θ), and the cavity length (d in Figure 1.7) can increase or decrease the radiative decay rate. [51] The change of radiative decay rate due to the optical structure (z , θ , d) is expressed by the so-called Purcell factor. Although the Purcell factor could be engineered to increase the intrinsic radiative decay

rate of the emitter, the effect is dwarfed and insignificant for high PLQY emitters.[50] For all optical simulations presented in this work, FLUXiM SETFOS software is used, which is based on the CPS model. The assumptions made in the CPS model are:[52]

1. The emitting layer must be transparent, i.e. the refractive index of the EML, and therefore the dielectric permittivity $\varepsilon = n^2$ must be real for all wavelengths considered. The same must be true for the material at the top of the multilayer stack.
2. The interface planes are infinitely extended.
3. The wavelength λ of the radiation as well as the distance between the emitter and the individual interfaces is large with respect to the spacial extensions of the dipole (point dipole approximation).
4. The dipole is at least at $\lambda/50$ –distance away from the regions with a complex permittivity ε .
5. The materials of the multilayer stack are non-magnetic.
6. The stack must be “lossy” (from the point of view of the radiating dipoles).

Further details on mathematical formulation of the model is presented below.

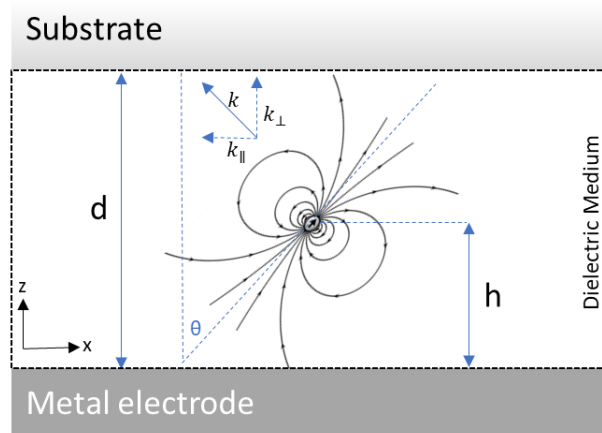


Figure 1.7. Radiative excitons can be treated as damped driven radiative dipoles, these damped dipoles are driven by the reflected electromagnetic field from the metallic cathode (bottom of figure). The dipoles can have both radiative and non-radiative decay rates depending on the photoluminescence quantum yield of the emitter. The radiative decay rate can be influenced by the dipole moment orientation with respect to the substrate plane (θ), emitter distance from metallic electrode (h) and the cavity length (d).

1.12.1. A dipole Near a Metal-Dielectric Interface

As I mentioned above, in the CPS optical treatment of excitons, a damped, forced, Hertzian dipole is assumed. Newton's second law for the damped driven dipole, is expressed as:

$$\ddot{\vec{p}} + b_o \dot{\vec{p}} + \omega^2 \vec{p} = \frac{e^2}{m} \vec{E}_R(\omega) \quad (1.3)$$

here, \vec{p} is the dipole moment vector, ω is the intrinsic frequency for the un-damped case,[48][46] b_o is the damping coefficient which is the same as the dipole transition rate. \vec{E}_R is the reflected electromagnetic field at the position of the dipole. A solution in the following form can be given to the differential equation above:

$$\vec{p}(t) = \vec{p}_o e^{-\left(i\omega + i\Delta\omega + \frac{b}{2}\right)t} \quad (1.4)$$

$$\vec{E}_R(t) = \vec{E}_o e^{-\left(i\omega + i\Delta\omega + \frac{b}{2}\right)t} \quad (1.5)$$

Substituting the solutions into the differential equation we find:[53]

$$\Delta\omega \approx \frac{b^2}{8\omega} - \frac{bb_o}{4\omega} - \frac{e^2}{2p_o m \omega} \text{Re}(E_o) \quad (1.6)$$

and

$$b = b_o + \frac{e^2}{p_o m \omega} \text{Im}(E_o) \quad (1.7)$$

The above solution for b, yields the dispersive radiated power of dipole as a function of reflected electric field at the position of the dipole. An example of calculated power dissipation of dipole in an OLED stack is shown in Figure 1.8a.

The reflected electric field at the position of the dipole in a multi-layer optical stack can be calculated using Fresnel reflection coefficients across boundaries for the two TE and TM polarizations. Fresnel reflection coefficient between two dielectric mediums for TM polarization is expressed as:

$$r_{12}^{TM} = \frac{\epsilon_1 k_{\perp 2} - \epsilon_2 k_{\perp 1}}{\epsilon_1 k_{\perp 2} + \epsilon_2 k_{\perp 1}} \quad (1.8)$$

For TE polarization Fresnel reflection coefficient between two mediums is expressed as:

$$r_{12}^{TE} = \frac{k_{\perp 2} - k_{\perp 1}}{k_{\perp 2} + k_{\perp 1}} \quad (1.9)$$

Here $k_{\perp 1}$ denotes the normal component of wavevector and ϵ is dielectric constant and 1 and 2 subscripts denote medium 1 and 2.

1.12.2. Surface Plasmon Polariton

Plasmons, or the “elementary excitations” are solutions of the homogenous Maxwell equations.[54][55] Surface Plasmon Polariton (SPP) is the asymptotic limit of Fresnel reflection coefficient for TM-polarized waves at a dielectric-metal boundary, where the denominator of equation (1.8) approaches zero. For a metal with dielectric constant ϵ_m , and for a dielectric with dielectric constant ϵ_d , putting the denominator of equation (1.8) equal to zero we have:

$$\epsilon_m k_{\perp d} + \epsilon_d k_{\perp m} = 0 \quad (1.10)$$

Moreover, from boundary conditions dictated by Maxwell equation the in-plane component of wave-vector must remain continuous across boundaries, i.e.:

$$k_{\parallel m} = k_{\parallel d} = k_{\parallel} \quad (1.11)$$

Also, we have:

$$k_{\perp m}^2 + k_{\parallel m}^2 = \epsilon_m \frac{\omega}{c} \quad (1-12)$$

And

$$k_{\perp d}^2 + k_{\parallel d}^2 = \epsilon_d \frac{\omega}{c} \quad (1.13)$$

Solving for equations (1-11), (1-12) and (1-13), the dispersion equation for surface plasmon polaritons can be derived as:

$$k_{\parallel} = \frac{\omega}{c} \left(\frac{\epsilon_m \epsilon_d}{\epsilon_m + \epsilon_d} \right)^{\frac{1}{2}} \quad (1.14)$$

We should note here that in order for denominator of equation (1.9) to be zero, the dielectric constant of the metal has to be purely imaginary. However, all metals are slightly absorbing, i.e. have a small real component in the dielectric constant. Therefore, in real situations the denominator never becomes exactly zero but becomes very small (approaches zero), resulting in a ‘‘SPP-like’’ propagation. [56]

1.12.3. Mode Analysis

Once we have calculated the power dissipation of the dipoles as a function of in-plane wave vector we can apply the kinematic limits to calculate optical mode distributions. In region 1 of Figure 1.8a, i.e.:

$$0 < k_{in} < \frac{2\pi n_{air}}{\lambda} \quad (1.15)$$

radiation will escape the glass substrate and ‘‘leak’’ to ambient air and integrating over this region of power dissipation would yield the ‘‘air-mode’’ contribution. In region 2 of Figure 1.8a, where k_{in} becomes larger than $\frac{2\pi n_{air}}{\lambda}$, light will be totally-internally-reflected into the substrate and integrating for the region:

$$\frac{2\pi n_{air}}{\lambda} < k_{in} < \frac{2\pi n_{glass}}{\lambda} \quad (1.16)$$

would yield the ‘‘substrate-mode’’ contribution. The radiation in the second region can easily be extracted using a semi-hemispherical lens with the same refractive index as the substrate. When k_{in} becomes larger than $\frac{2\pi n_{glass}}{\lambda}$, light will be totally-internally-reflected from the ITO/glass boundary and will not enter the substrate, therefore integrating region 3 of Figure 1.8a, i.e:

$$\frac{2\pi n_{glass}}{\lambda} < k_{in} < \frac{2\pi n_{EML}}{\lambda} \quad (1.17)$$

would yield the “waveguide-mode” contribution. Here n_{EML} denotes the refractive index of the emissive layer (EML), where the dipole is located. The maximum allowed magnitude for the in-plane wave vector for a far-field radiation is $\frac{2\pi n_{EML}}{\lambda}$, since the emitter is in the EML, and when the in-plane wave vector becomes larger than the total magnitude of the wave vector, i.e.:

$$k_{in} > \frac{2\pi n_{EML}}{\lambda} \quad (1.18)$$

the wave vector will acquire an imaginary component which renders the radiation evanescent in near-field. Therefore, integrating the region with $k_{in} > \frac{2\pi n_{EML}}{\lambda}$, i.e. region 4 of Figure 1.8a, yields the “evanescent-mode” contribution. It should be noted here that even though radiation with $k_{in} > \frac{2\pi n_{EML}}{\lambda}$ is evanescent in the organic emissive layer, there could be a high-index layer such as ITO that can support far-field radiation with $k_{in} > \frac{2\pi n_{EML}}{\lambda}$. [40] Interestingly, the in-plane wave vector of the transvers-electric waveguide mode (TEWG) which centers in the ITO layer is larger than $\frac{2\pi n_{EML}}{\lambda}$ and lays in the evanescent region. TEWG will be further discussed in chapter 3 of this dissertation.

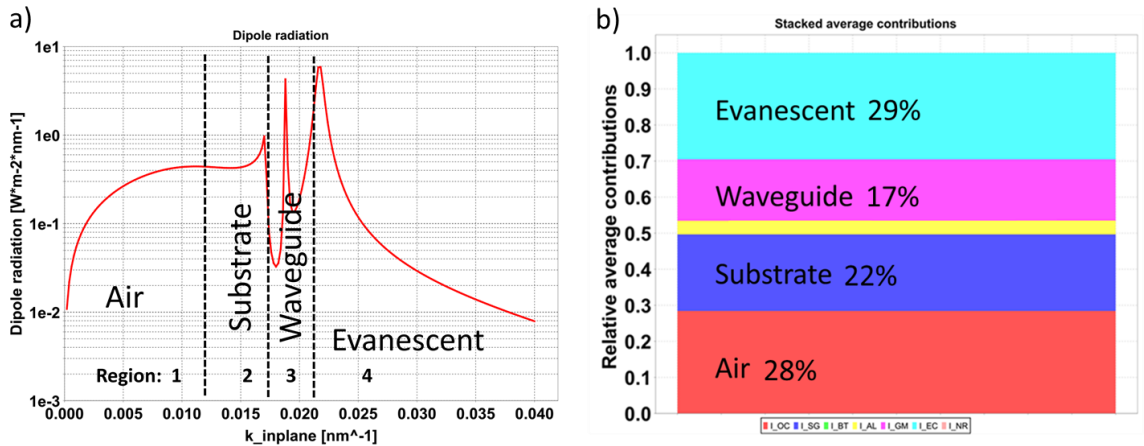


Figure 1.8. The calculated dipole radiation (power dissipation) can be categorized in four different regions depending on the magnitude of the inplane wave vector of the radiation: region 1, indicates the radiation that leaks to the ambient, and is so called “air-mode”. Region 2 indicates the “substrate-mode”. Regions 3 and 4 indicate the “waveguide-mode” and “evanescent-mode” respectively. Emitter dipole orientation and distance from the metal can heavily affect radiation coupling into surface plasmon polaritons and the evanescent-mode contributions. c) An example of optical-mode-distribution calculated from power dissipation results.

1.12.4. Emitter Dipole Orientation

The orientation of the transition dipole moment vectors (TDMVs) of the emitting molecules with respect to the plane of the OLED substrate has large effects on light extraction.[57][58][59] A horizontally oriented dipole, with its axis lying in the substrate plane, leads to maximum light extraction, since a dipole’s radiation is the strongest, normal to its axis. While, a vertically oriented dipole will strongly couple to the TM-polarized SPP modes of the metallic cathode, since the SPP electric field, which is normal to the plane of the substrate, will have complete overlap with the dipole vector. Figure 1.9 shows the effect of emitter dipole orientation on mode-contribution in an OLED device.

The orientation of the transition dipole moment of organic molecules in a thin film, can be measured using two main methods. The first method relies on measuring the anisotropy in

extinction coefficient (k), using variable angle spectroscopic ellipsometry (VASE).[60] The extinction coefficient is directly related to the absorption coefficient (α), through the equation:

$$k = \alpha \frac{\lambda}{4\pi} \quad (1.19)$$

and has a larger value in the direction of the transition dipole moment. After measuring the extraordinary and the ordinary components of the extinction coefficient, i.e. k_e and k_o , the orientation of the transition dipoles can be found using an order parameter defined as:

$$S = \frac{k_e^{max} - k_o^{max}}{k_e^{max} + 2k_o^{max}} = \frac{3\Theta - 1}{2} \quad (1.20)$$

where Θ indicates the ensemble average of vertically oriented transition dipole moments, i.e. $\Theta = \langle \cos^2(\theta) \rangle$, here θ is the angle between the collective ensemble TDMV and the normal to the substrate. Therefore, for completely vertically aligned TDMVs, $\Theta = 1$ and $S = 1$, for randomly oriented TDMVs, $\Theta = \frac{1}{3}$ and $S = 0$, and for completely horizontally aligned TDMVs, $\Theta = 0$ and $S = -\frac{1}{2}$. The VASE method for orientation measurement is especially popular for linearly-shaped molecules, since the anisotropy in optical constants (both n and k) can also provide information on physical orientation of the molecule, and in linearly shaped molecules the TDMV is mainly along the molecules axis.[60] The second method for measuring the TDMV orientation, is by measuring angular dependent p-polarized photoluminescence of the emissive thin film layer, and fitting the measurement results to optical simulations assuming different TDMV orientation for the emitter.

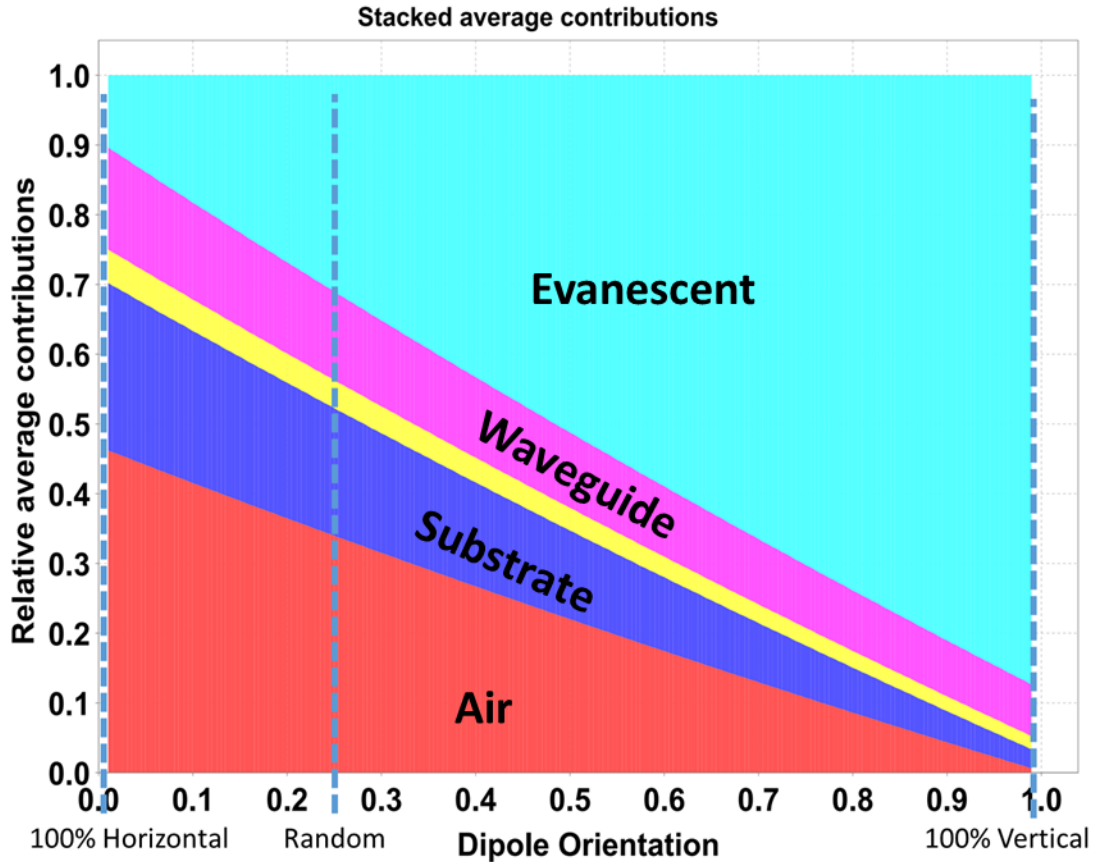


Figure 1.9. Effect of dipole orientation on mode-contribution in an OLED device. Vertically aligned dipole moments strongly couple to the surface plasmon polaritons and have significant loss in the evanescent region.

1.13. Conclusions

In conclusion, in the first chapter, I started by introducing organic molecular solids. The physical structure of OLED devices and methods of fabrications were introduced. Conventional understanding of charge injection in organic molecular solids and exciton formation were discussed. I argued that the conventional understanding regarding charge injection in organic semi-conductors does not hold for a large class of organic solids, which will be shown in the last chapter of this thesis. After introducing different types organic emitters, I outlined the electronic design rules for an efficient OLED, including: ohmic contacts, charge balance and exciton confinement.

I then summarized the optical design rules for efficient electroluminescence in OLED devices including: substrate light extraction, waveguide light extraction and suppression of evanescent loss. Optical design rules were then discussed. At the end of Chapter 1, I outlined a Hertzian dipole model that is prevalently used for optical calculations of OLED stacks.

CHAPTER 2

CHAPTER 2: Suppressing evanescent loss using low refractive index electron transport layer

2.1. Abstract

As I mentioned in the previous chapter, a low refractive index electron transporting layer (ETL) can be very effective in enhancing the out-coupling efficiency of an organic light emitting diode (OLED). However, most organic films show a refractive index close to 1.8. In this chapter, I will present the discovery of a low refractive index of tris-[3-(3-pyridyl)mesityl]borane (3TPYMB) $n=1.65$ (at 550 nm), which has the lowest refractive index ETL among the commonly used ETLs up to date. Using 3TPYMB as an ETL, I will demonstrate a solution processed OLED with nearly a 76% enhancement in external quantum efficiency (EQE). My optical simulation results show that 59% of the enhancement comes from the low refractive index 3TPYMB, and the remaining 17% from the change in charge balance due to the 3TPYMB ETL in the studied OLED devices.

2.2. Introduction

As I described in the previous chapter, in a typical OLED, about 20% of the generated radiation is out-coupled, and most radiation is lost to three main loss channels: substrate-mode, evanescent-mode and waveguide-mode. The radiation trapped in the substrate and waveguide-modes undergoes total internal reflection (TIR) from the substrate-air and anode-substrate boundaries respectively,[61] which can be extracted using scattering layers, corrugated substrates, half-spherical lenses or a combination of the above light extraction schemes.[62][63] However, when radiation is lost to evanescent-mode, it decays in the nearfield and cannot be extracted by

the latter methods. An effective way for suppressing the radiation loss to the evanescent-mode is to use a low refractive index electron transport layer (ETL).

According to the outlined electronic design rules mentioned in the previous chapter: to design a high efficiency OLED, it is important to have a multilayer structure to control the radiative recombination such that excitons are confined to the emissive layer (EML) using high triplet charge blocking layers. In addition to exciton confinement, the electron and hole transport layers should be chosen in such a way to maintain the charge balance to avoid triplet-polaron quenching. In a multilayer OLED, the ETL also plays a key role in determining the light extraction efficiency since it is the intermediate layer between the EML and the metallic cathode, and a large portion of the dipole radiation from the EML is lost to the evanescent region where the in-plane wave-vector is larger than the total wave-vector, resulting in radiation that is coupled to the surface plasmon polariton (SPP) and the “lossy surface waves” on the metallic cathode.[46] The magnitude of the loss to the SPP mode is determined by the dielectric constants of the metallic cathode and the ETL, therefore the refractive index of the ETL can significantly impact the out-coupling efficiency of an OLED. There have been some reports demonstrating the effect of the ETL’s refractive index on light extraction efficiency in OLEDs by simulation. [64][65] However, experimental study of the effect of ETL refractive index on device performance is rather limited.[66]

In this chapter, I demonstrate the effect of ETL’s refractive index on device efficiency using a solution processed OLED with a copper-based thermally activated delayed fluorescent (TADF) emitter, [(2-(Diphenylphosphino)-4-isobutylpyridine)(PPh₃)₂Cu²I₂] (Cu(I)-iBuPyrPHOS). The emitter has a photoluminescence quantum yield (PLQY) of 70%.[67] Based on the PLQY and assuming an outcoupling efficiency of 20%, a maximum EQE of 14% is expected. Using 2,9-di(naphthalen-2-yl)-4,7-diphenyl-1,10-phenanthroline (NBPhen) and 2,4,6-

tris(biphenyl-3-yl)-1,3,5-triazine (T2T) as ETLs, I showed that an optimized device has a maximum EQE of 12% which is close to the estimate of the maximum EQE of 14%. Surprisingly, using 3TPYMB as the ETL, I achieved a maximum EQE of 21%, showing nearly a 76% enhancement just by changing the ETL alone. Upon investigation of the origin of the efficiency enhancement, I found that the refractive index of 3TPYMB is 1.65, which is the lowest among all commonly used ETLs, resulting in a significant enhancement in light extraction efficiency. My device data are also confirmed by the optical simulation results.

2.3. Crosslinkable Hole Transporting Layer in Solution-processed OLED

Fabricating a multilayer OLED by solution processing is not straightforward owing to the intermixing of organic materials during fabrication. One solution is to use orthogonal solvents for adjacent layers, but most organic materials are soluble in both polar and non-polar solvents, which complicates this process.[68][69] To address this problem, solvent resistant materials such as crosslinkable small molecules hole transport layers (HTLs) have been developed.[70][69][71] In my device structure, I used PLEXCORE UT314 (UT314) as the crosslinkable HTL.[71] Figure 2.1 shows the chemical structures of UT314 and other materials used in this study. UT314 was prepared in solution form in toluene solvent, and spin casted on top of PEDOT:PSS layer. The spin-casted layer was then heat-cured to form a cross-linked layer. The highest occupied molecular orbital (HOMO) and lowest unoccupied molecular orbital (LUMO) levels of UT314 are 5.4 eV and 2.4 eV respectively, which are very close to the corresponding values for the commonly used HTL 4,40-bis[N-(1-naphthyl)-N-phenylamino]biphenyl (NPB).

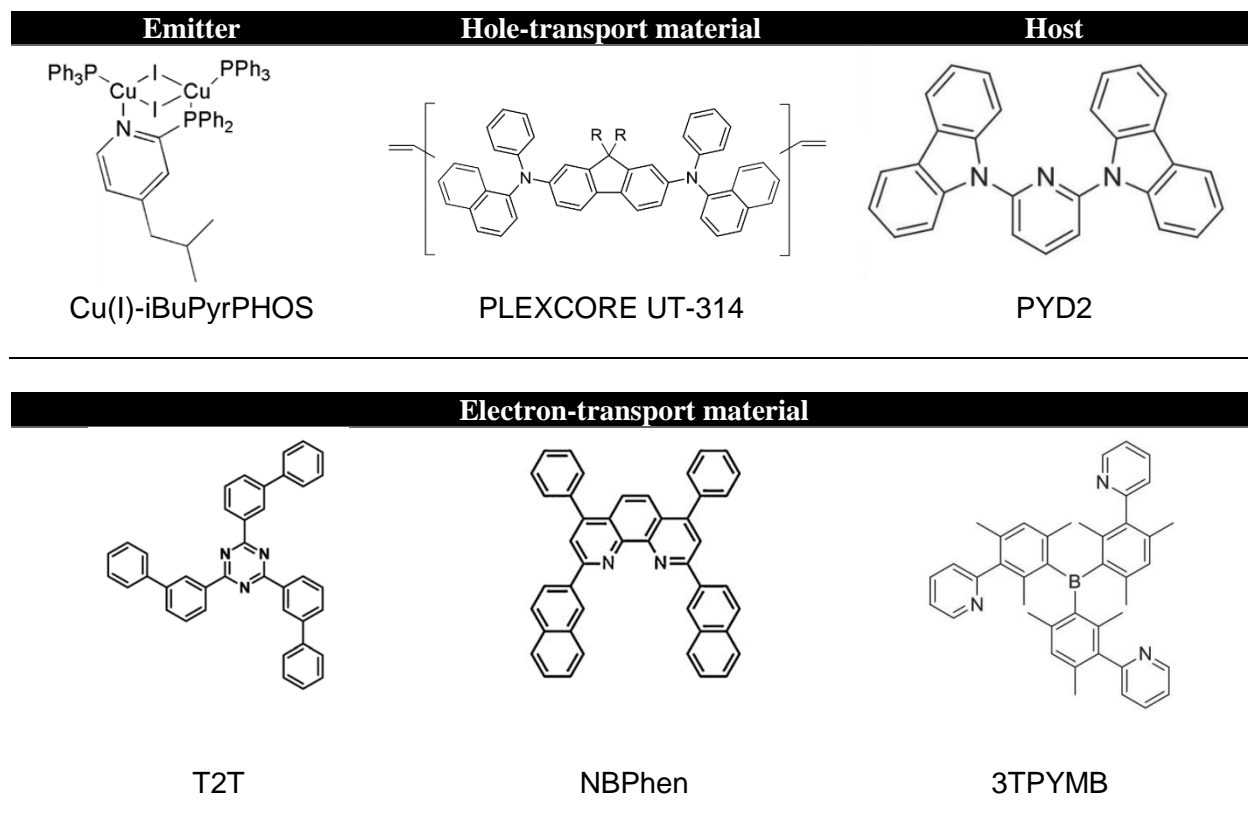


Figure 2.1. Molecular structures of materials used.

2.4. Design of the High Efficiency TADF OLED

For the emitting layer, I chose 2,6-dicarbazo-1,5-pyridine (PYD2) as the host because of its deep HOMO (5.9 eV) and shallow LUMO (2.4 eV), along with its high triplet energy of 2.9 eV, which is desirable for a host material.[72] For the ETL, I used T2T, which is an effective hole blocking layer (HBL) with a HOMO level of 6.7 eV and triplet energy of 2.8 eV.[73] High efficiency TADF devices have been demonstrated with T2T as an ETL.[21][74][75]

2.5. Optimized Devices Using Conventional Electron Transporting Layers

my optimized device using T2T (Device A) has the following structure: ITO (100 nm) /poly(3,4-ethylenedioxythiophene) polystyrene sulfonate (PEDOT:PSS) (35 nm) /PLEXCORE UT-314 (20 nm) /PYD2:Cu(I)-iBuPyrPHOS 1:1 (30 nm) /T2T (20 nm) /NBPhen (30 nm) /LiF (1

nm)/Al. I used NBPhen as the secondary ETL to reduce the electron injection barrier from the cathode. The results of Device A optimization are shown in Figure 2.2 and 2.3.

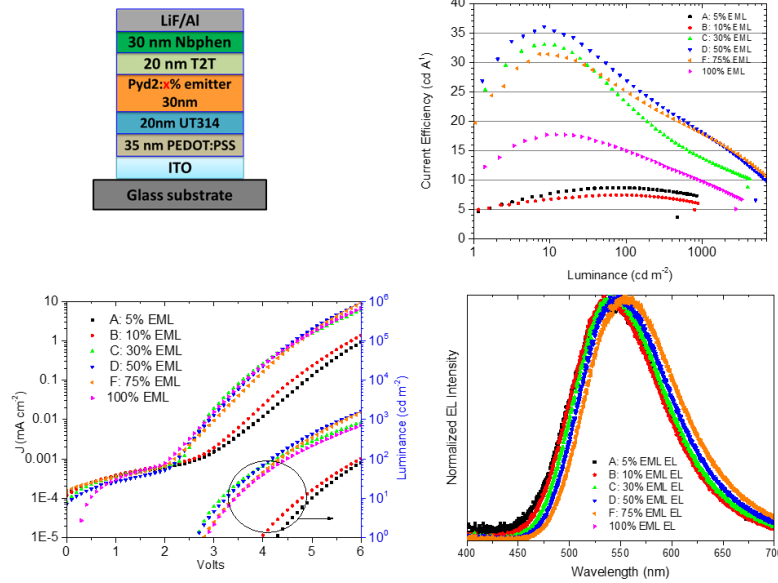


Figure 2.2. Characteristics of devices using T2T and NBphen, with different emitter concentrations. (EML concentration optimization)

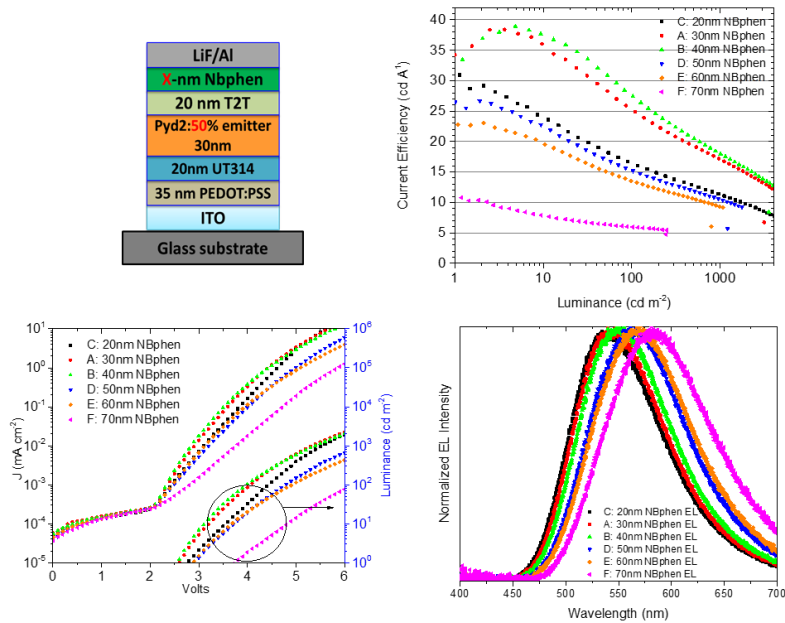


Figure 2.3. Characteristics of devices using T2T and NBphen, with different NBphen thicknesses. (ETL thickness Optimization)

2.6. Optimized Devices Using 3TPYMB as Electron Transporting Layers

In addition to the above ETLs, I also used 3TPYMB as an ETL in my study. There have been many reports of high efficiency OLEDs employing 3TPYMB as an ETL,[76][77][78][31] because of its deep HOMO of 6.8 eV and high triplet energy of 2.9 eV.[79] My optimized device with 3TPYMB (Device B) has the following structure: ITO (100 nm) /PEDOT:PSS (35 nm) /PLEXCORE UT-314 (20 nm) /PYD2:Cu(I)-iBuPyrPHOS 3:1 (30 nm) /3TPYMB (70 nm) /LiF (1 nm)/Al. The results of the optimization of Device B are also presented in Figure 2.4 and 2.5. The current density-voltage-luminance (J-V-L) characteristics, electroluminescence (EL) spectra and EQE of the two optimized devices are shown in Figure 2.6.

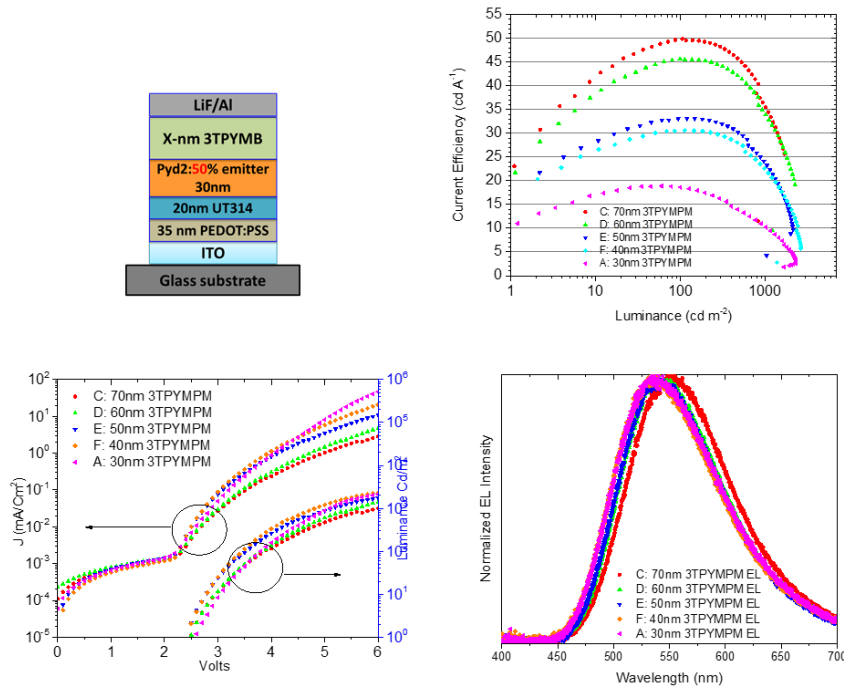


Figure 2.4. Characteristics of devices using 3TPYMB, with different 3TPYMB thicknesses. (ETL thickness Optimization)

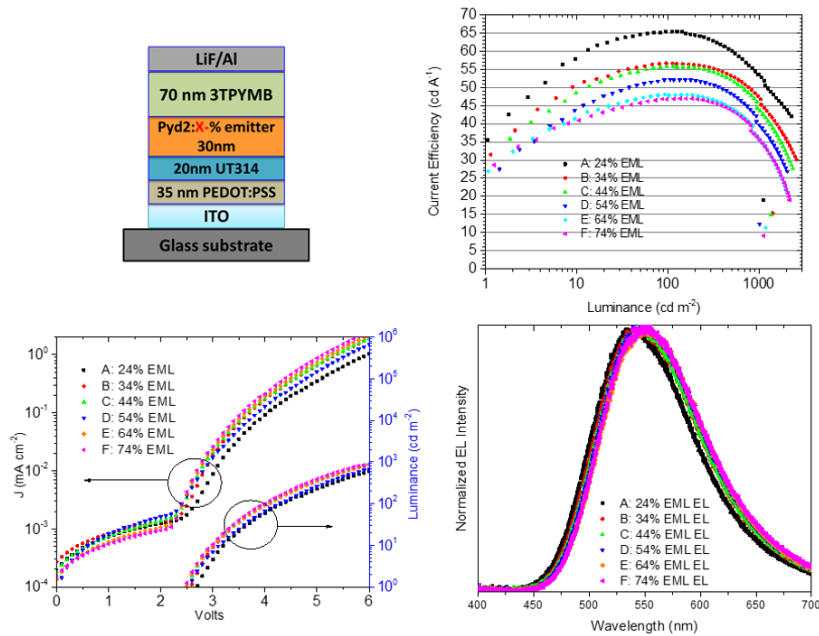


Figure 2.5. Characteristics of devices using 3TPYMB, with different emitter concentrations. (EML concentration optimization)

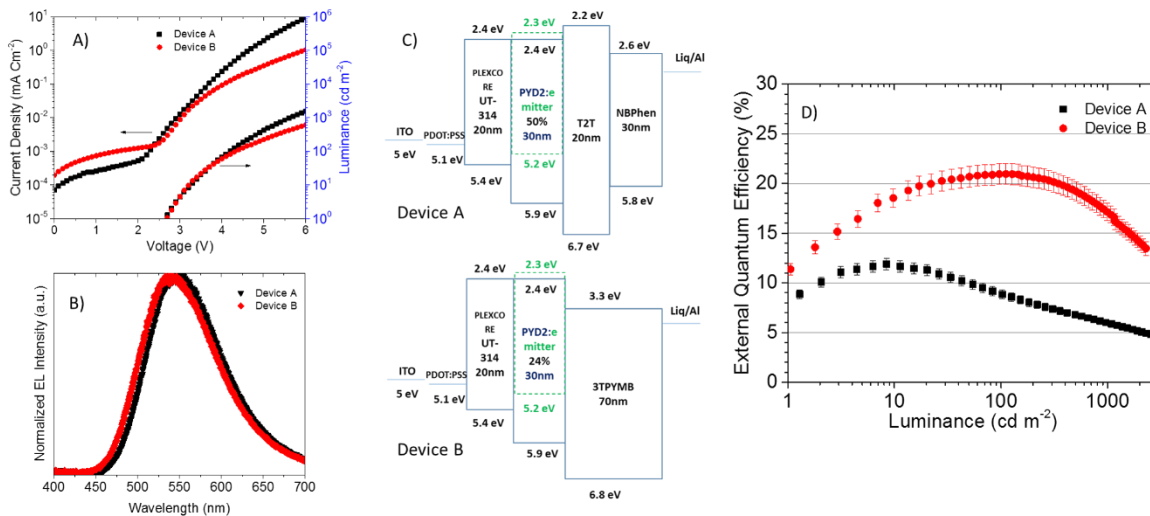


Figure 2.6. The performance of device A and device B: A) Current density -Voltage-Luminance (J-V-L) characteristics. B) The electroluminescence (EL) spectra. C) Device energy band diagram. D) EQE vs. Luminance.

2.7. Difference in Thicknesses of the Two ETLs

The electron mobility of 3TPYMB is about $1 \times 10^{-5} \text{ cm}^2 \text{ V}^{-1} \text{ s}^{-1}$, [22] while T2T and NBPhen have an electron mobility of about $1.2 \times 10^{-4} \text{ cm}^2 \text{ V}^{-1} \text{ s}^{-1}$ and $4.2 \times 10^{-4} \text{ cm}^2 \text{ V}^{-1} \text{ s}^{-1}$ respectively. [73][80][81] The electron mobility of both T2T and NBPhen is more than one order of magnitude higher than that of 3TPYMB. Since the emitter is responsible for hole transport through the EML, a higher emitter concentration is needed to reach charge balance when an ETL with a higher electron mobility is used. Since high concentrations of the Cu(I) emitter used in the EML do not lead to concentration quenching, [82] a higher emitter doping concentration is used in Device A to achieve charge balance. It should be noted that the total ETL thickness is larger in Device B to compensate for the optical path length difference resulted from the different refractive indices of the ETLs. It is important to note that an optimum ETL thickness ($d_{ETL} \propto \frac{\lambda_o}{4n_{ETL}}$) is larger for the ETL with a lower refractive index (see Figure 2.7). [83] Here, d_{ETL} is the thickness of the ETL, λ_o is the emission wavelength in vacuum and n_{ETL} is the refractive index of the ETL. I will show below that 3TPYMB has a lower refractive index compared to both T2T and NBPhen and that is why the 3TPYMB layer is thicker than the combined thickness of T2T and NBPhen.

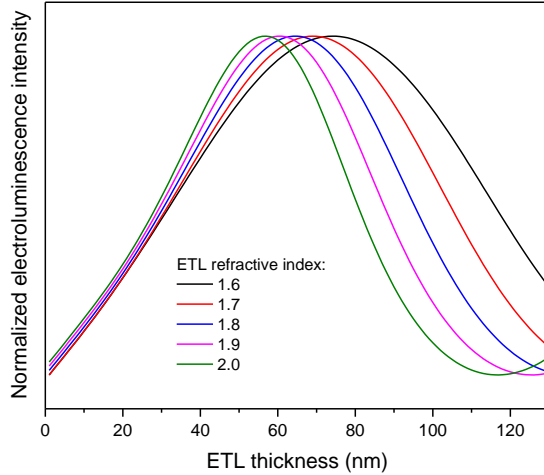


Figure 2.7. Simulation of normalized electroluminescence intensity versus ETL thickness for five different refractive indices of ETL. Maximum intensity happens at smaller ETL thicknesses for larger ETL refractive indices.

Table 2.1. Device performance summary.

	V_{on} ^{a)} [V]	$CE_{100}/EQE_{100}/V_{100}$ ^{b)} [$cd.A^{-1}/\%/V$]	$CE_{1000}/EQE_{1000}/V_{1000}$ ^{c)} [$cd.A^{-1}/\%/V$]	$CE_{max}/EQE_{max}/\lambda_{max}$ ^{d)} [$cd.A^{-1}/\%/nm$]
Device A	2.7	26.8/8.8/4.2	18.2/6.0/5.6	36.0/11.9/550
Device B	2.7	65.4/21.0/4.3	53.6/17.1/6.6	65.4/21.0/538

a) V_{on} is turn-on voltage at 1 cd.m^{-2} b) Current Efficiency (CE), EQE and Voltage at 100 cd.m^{-2} c) Current Efficiency (CE), EQE and Voltage at 1000 cd.m^{-2} d) Maximum Current Efficiency (CE), maximum EQE and wavelength of electroluminescence peak.

The details of performance of the devices are summarized in Table 2.1. Both devices have a low turn-on voltage of 2.7 V. Device A shows a maximum EQE of 11.9%. However, Device B shows a maximum EQE of 21%, which is a 76% enhancement compared to Device A. I will show that the difference in the performance of the two devices is mainly due to opto-electronic superiority of 3TPYMB.

2.8. Measuring Refractive Index of Electron Transport Layers

To understand the difference in optics due to the different ETLs, I first measured the refractive indices of the three ETLs and studied their effects on light out-coupling efficiencies. Refractive indices of T2T, NBPhen and 3TPYMB were measured using variable angle spectroscopic ellipsometry (VASE). The VASE data were fitted to a uniaxial Cauchy model in the transparent region. 3TPYMB shows an isotropic index of refraction with a low n value of 1.65 at $\lambda = 550$ nm, while T2T shows a positive in-plane birefringence ($n_o = 1.67$, $n_{ext} = 1.82$ at $\lambda = 550$ nm) and NBPhen shows a negative in-plane birefringence ($n_o = 1.87$, $n_{ext} = 1.69$ at $\lambda = 550$ nm), where n_o is the ordinary index of refraction and n_{ext} is the extraordinary index of refraction. The refractive index data are shown in Figure 2.8. Table 2.2 also shows the refractive indices of some commonly used ETLs at 550 nm. [7] Using the measured values of the refractive indices, I calculated optical light extraction efficiencies of the two optimized devices using the SETFOS simulation software.

Table 2.1. Refractive indices of different ETLs at 550nm

Material (ETL)	n_o ^{a)} ordinary	n_e ^{b)} extraordinary	$n_{isotropic}$
T2T	1.67	1.81	--
NBPhen	1.87	1.69	--
3TPYMB	--	--	1.65
Alq ₃ ^{c)}	--	--	1.72
TPBi ^{c)}	--	--	1.73
B3PYMPM ^{c)}	1.82	1.6	--
PO-T2T ^{c)}	--	--	1.70

a) n_o is the ordinary refractive index. b) n_e is the extraordinary refractive index. c) The refractive indices of these materials are from Reference [4].

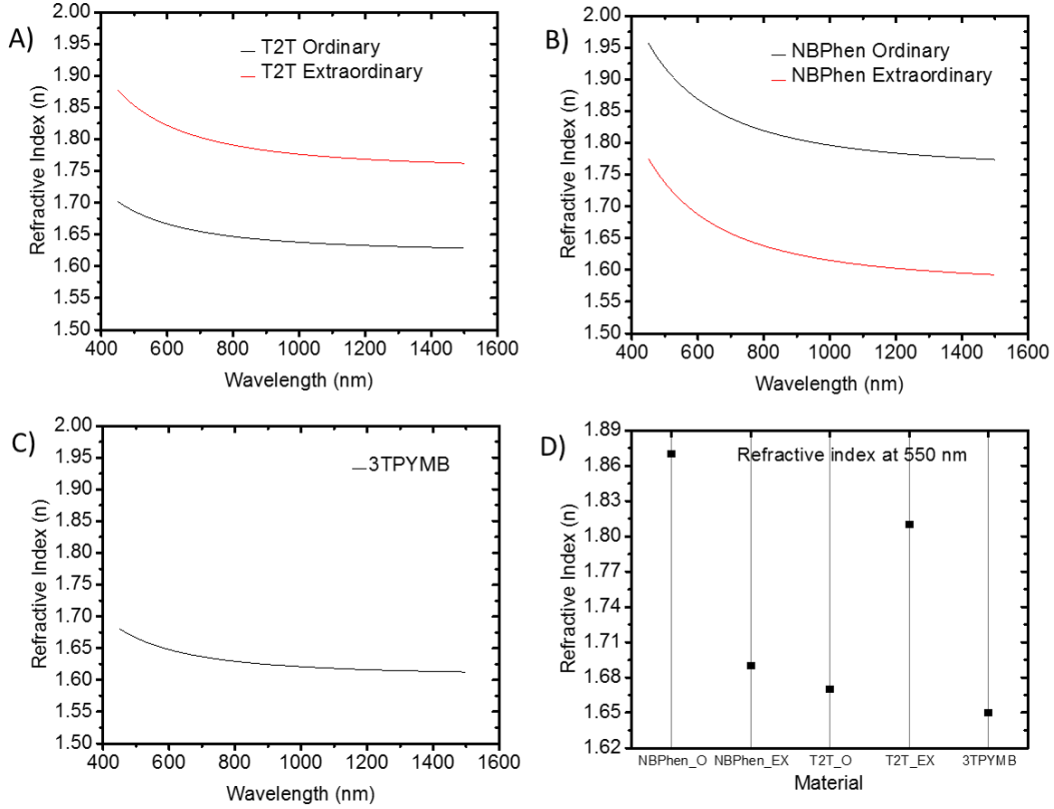


Figure 2.8. Measured refractive index of: a) T2T, showing positive in-plane birefringence. b) NBPhen, showing negative in-plane birefringence. c) 3TPYMB, showing an isotropic low refractive index. d) All measured refractive indices at $\lambda=550\text{nm}$. All refractive indices were measured using a spectroscopic ellipsometer and fitted to a uniaxial Cauchy model in transparent region.

2.9. Optical Simulations

2.9.1. Suppression of Evanescent Loss Following the SPP Dispersion Equation

As mentioned in section 1.12, in my optical simulation, excitons are treated as damped forced dipoles that are driven by a reflected electromagnetic field from the metallic cathode.[46] The power dissipation of these dipoles is calculated as a function of the in-plane wave-vector (k_x) of the generated electromagnetic waves. The normalized k_x with respect to EML is: $u_{in} = \frac{k_x}{\frac{2\pi n_{EML}}{\lambda}}$, where n_{EML} is the refractive index of the EML. The calculated power dissipation versus u_{in} can be divided into four different regions, as shown in Figure 2.9.[84] The first region corresponds to

the air-mode, where the normalized in-plane wave-vector is larger than zero and smaller than the inverse of the EML's refractive index ($0 < u_{in} < \frac{1}{n_{EML}}$). In this region, the power dissipation couples to the far field “leaky” radiation,[46] and escapes from the substrate into the air. The second region corresponds to the substrate-mode, where $\frac{1}{n_{EML}} < u_{in} < \frac{n_{substrate}}{n_{EML}}$, and the power dissipation here couples to the trapped radiation into the substrate. The third region corresponds to the waveguide-mode, where $\frac{n_{substrate}}{n_{EML}} < u_{in} < 1$, and the power dissipation in this region couples to the radiation trapped in the OLED waveguide-mode, which propagates between the OLED-substrate boundary and the cathode. The fourth region corresponds to the evanescent-mode where $u_{in} > 1$ and the power dissipation here couples to the surface plasmon polaritons and lossy surface waves.[46] Figure 2.9 shows the intensity profile under the power dissipation curve in each region, representing the amount of power that goes into the corresponding mode associated with that region. The dispersion equation for the SPP waves is given by $u_{in} = \frac{1}{n_{EML} \left(\frac{\epsilon_{cathode} \cdot \epsilon_{ETL}}{\epsilon_{cathode} + \epsilon_{ETL}} \right)^{\frac{1}{2}}}$, where $\epsilon_{cathode}$ is the dielectric constant of the metallic cathode and ϵ_{ETL} is the dielectric constant of the ETL. From the SPP dispersion equation, a smaller value of ϵ_{ETL} (or n_{ETL}^2) will result in a smaller value of u_{in} , thus shifting the power dissipation from the fourth region towards the first region. The power dissipation profiles for devices with six different values of n_{ETL} are shown in Figure 2.9. Here, the thickness of the ETL is assumed to be 50 nm. Figure 2.9 clearly demonstrates that the ETL's lower refractive index will result in a smaller evanescent (SPP) loss and a strong coupling to the substrate and air-modes. The percentage of power coupling to the evanescent-mode and to the substrate plus air-mode versus n_{ETL} is calculated from the power dissipation shown in Figure 2.9 and presented in Figure 2.10. As we can observe, by reducing the refractive index of

ETL from 2 to 1.5, the percentage of power coupled to the evanescent region decreases from 61% to 40%, while the percentage of power coupled to air plus substrate increases from 32% to 53%.

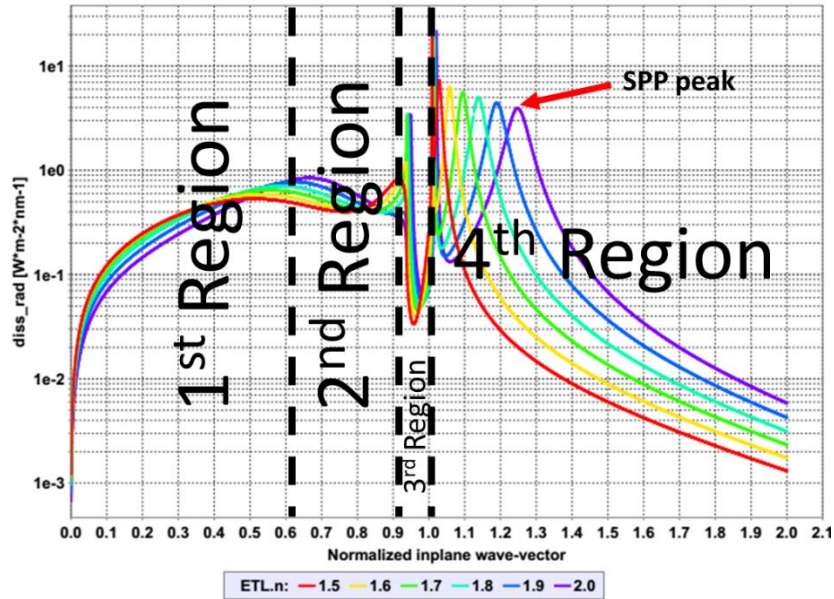


Figure 2.9. Power dissipation as a function of normalized in-plane wave-vector for six different refractive indices of ETL. The area under the curve in first region indicates the amount of light escaping to air (air-mode). The area under the curve in second region indicates the amount of light trapped in substrate (substrate-mode). The area under the curve in third region indicates the amount of light trapped in waveguide (waveguide-mode). The area under the curve in fourth region indicates the amount of power lost to SPPs (evanescent-mode). Lower refractive index for ETL, shifts the SPP peak from larger normalized inplane wave-vectors to smaller, resulting in less loss in the evanescent region. Here ETL thickness is assumed to be 50nm.

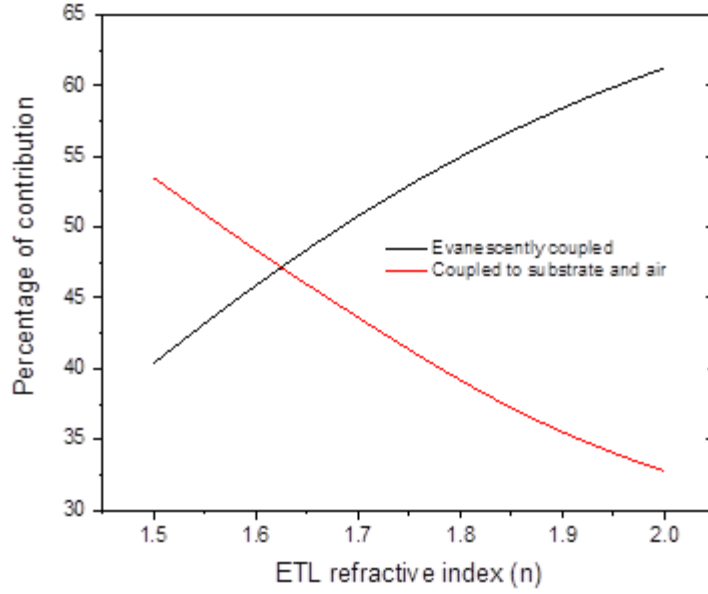


Figure 2.10. Percentage of power that is coupled to SPP (evanescently coupled) and to substrate plus air-modes as a function of refractive indices of ETL. Lower refractive index of ETL will result in more light out-coupling to air and substrate at expense of less power loss to SPPs (evanescently coupled). Contribution of each mode is calculated based on the power dissipation shown in Figure 2.9.

2.9.2. Optical Simulations: Suppression of Evanescent Loss Following the Fermi's Golden Rule

As mentioned earlier, an ETL with a lower refractive index requires a larger film thickness to compensate for the optical path difference to achieve optimum light extraction, as I have showed in Figure 2.7. This increase of ETL thickness will further reduce the power dissipation coupling to the SPP and lossy surface waves due to a smaller overlap between the dipole and the electric field of the SPP mode.[46][45] Following the Fermi's golden rule, the probability of dipole emission coupling into the SPP mode is given by:[45]

$$P(\omega) = \frac{2\pi}{\hbar} |\langle i | \vec{p} \cdot \vec{E}(z) | f \rangle|^2 \rho(\hbar\omega), \quad (2-1)$$

here \vec{p} is the dipole moment, $\rho(\hbar\omega)$ is the mode density of plasmons, i and f are the initial and final exciton state wavefunctions, z is the distance of dipole from metal which is determined by

ETL thickness, and \vec{E} is the electric field of SPP mode. The electric field of SPP decays exponentially as the distance from metal increases, leading to a smaller probability of SPP coupling for thicker ETL layers following equation 2-1.

The power dissipation intensity profiles, for different ETL thicknesses with the same refractive index, are shown in Figure 2.11. Here, the refractive index of ETL is assumed to be 1.65. As we can see, by increasing the ETL thickness, the SPP peak does not change; however, the area under the profile for $u_{in} > 1$ in the fourth region decreases, resulting in a smaller power loss to the SSPs and the lossy surface waves. The percentage of power coupling to the evanescent-mode and to the substrate plus air-mode versus ETL thickness is calculated from the power dissipation shown in Figure 2.11 and the results are presented in Figure 2.12. As we observe, by increasing the ETL thickness from 50 nm to 90 nm, the percentage of power coupled to the evanescent region decreases from 57% to 49%, while the percentage of power coupled to air plus substrate increases from 34% to 45%.

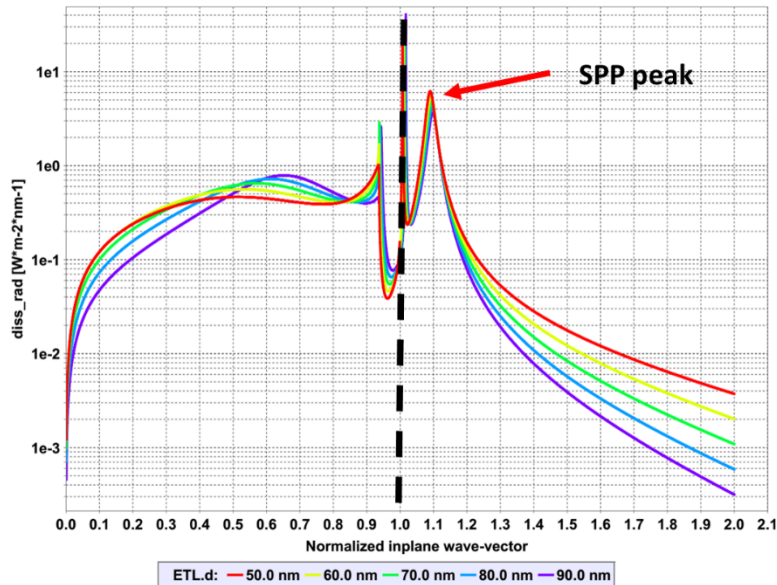


Figure 2.11. Power dissipation as a function of normalized in-plane wave-vector for six different thicknesses of ETL at 550nm. The area under each curve to the right of the black dashed line indicates the amount of power lost to the SPPs. Here refractive index of ETL is assumed to be 1.65

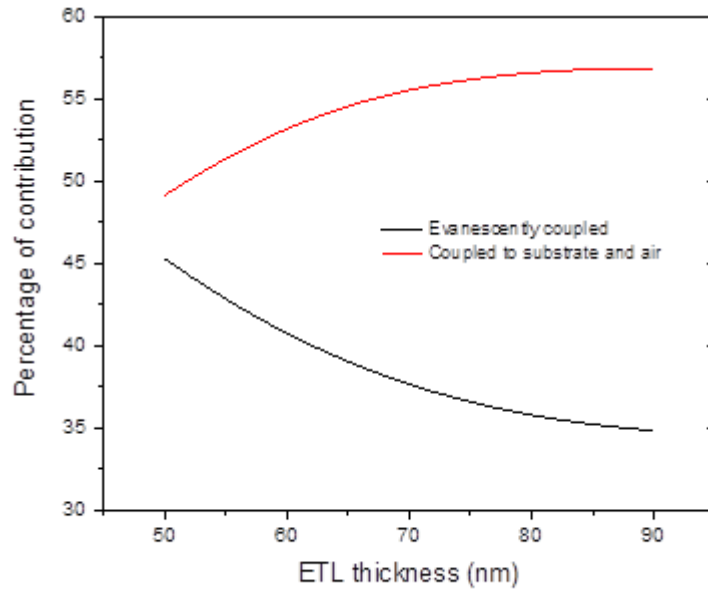


Figure 2.12. Percentage of power that is coupled to SPP (evanescently coupled) and to substrate (substrate + air-mode) as a function of ETL thickness. Increase in the thickness of ETL will result in more light out-coupling to air and substrate at expense of less power loss to SPPs (evanescently coupled). Contribution of each mode is calculated based on the power dissipation shown in Figure 2.11.

2.9.3. Optimized Device

I have presented the relative contributions of the different modes for Device A and Device B (at $\lambda = 550$ nm) in Figure 2.13a and 2.13b. The spectral power dissipation of the two devices are shown in Figure 4c and 4d. The blue double arrow in Figure 2.13c and 2.13d indicates the fourth region, where the power dissipation couples to the SPP waves, and the red double arrow shows the first plus the second region, where the power dissipation is coupled to radiation into the substrate

and air. We can see a clear increase in the radiation into the substrate and air and decrease in coupling into the evanescent region in Device B compared to Device A.

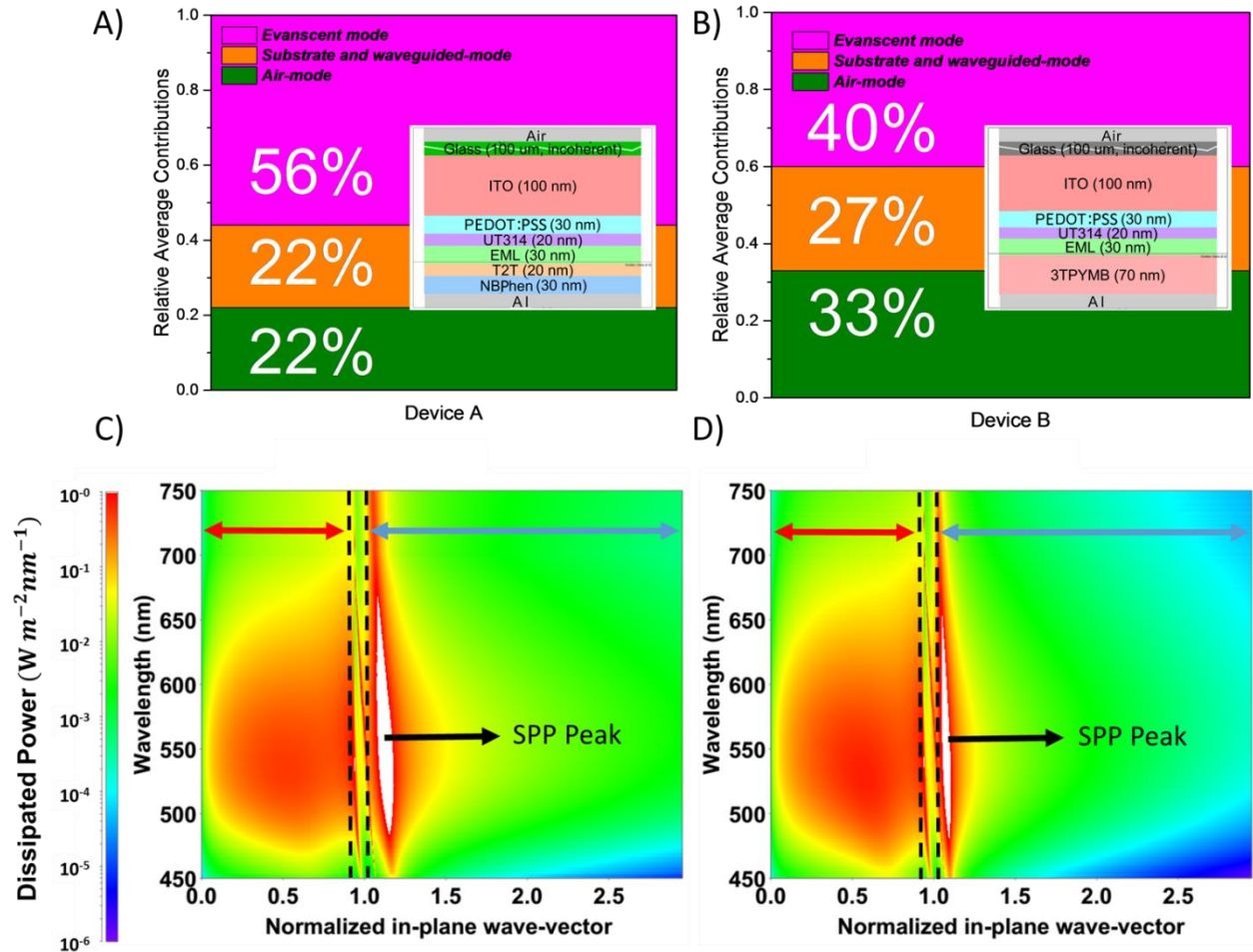


Figure 2.13. a) and b) Mode power contributions of Device A and Device B respectively. * Other loss channels include substrate modes, waveguide modes. Inset shows the corresponding device structure used in calculation. c) and d) Spectral power dissipation as a function of normalized in-plane wave-vector for Device A and Device B respectively. The region indicated by red double arrow is out-coupled to substrate and air, and the region indicated by blue double arrow is evanescent, the region between the two dashed lines is coupled to wave-guide mode.

The calculated contribution of the air-mode for Devices A and B are 22% and 33%, respectively as shown in Figure 2.13a and 2.13b, indicating a 50% enhancement in light extraction efficiency due to the 3TPYMB ETL. When we consider the 70% PLQY of the emitter, the

calculated EQEs for Device A and Device B are reduced to 15% and 23% respectively. The 21% experimentally obtained EQE for Device B is in good agreement with the calculated value of 23%. However, the 12% experimentally obtained EQE for Device A is significantly lower than the calculated value of 15%. It should be noted that the calculated values are based on pure optical calculations, and the larger discrepancy between the experimental and calculated EQE in Device A can be explained in terms of its electrical characteristics, compared with Device B. Based on what I discussed here, out of the 76% experimentally observed increase in efficiency, 59% is attributed to the optical enhancement of 3TPYMB and 17% is attributed to the change in charge balance due to 3TPYMB as explained below.

2.10. An Opto-Electronic Interplay

Considering the energetics of the device stack, the HOMO level and the triplet energy of 3TPYMB (HOMO = 6.8 eV, E_T = 2.9 eV) are slightly larger than those of T2T (HOMO = 6.7 eV, E_T = 2.8 eV), which results in a better hole blocking and exciton confinement in the 3TPYMB device. As it can be seen in Figure 2.6d, we observe a noticeably smaller efficiency roll-off at higher luminance levels for Device B, implying a better charge balance resulting from a more effective hole blocking under higher biases.[31] We have previously shown that a deeper HOMO for an effective hole-blocking ETL is required for solution processed EMLs due to a wider band-broadening and the energetic disorder at the EML/ETL interface.[85] As I have shown in Figure 2.6d, the EQE of Device A reduces to 5% at a high luminance of 2000 cd m⁻² from a maximum EQE value of 12%, showing a large efficiency roll-off of 58%. However, the EQE of Device B reduces to 14% at 2000 cd m⁻² from a maximum EQE value of 21%, showing a smaller efficiency roll-off of 33%. Furthermore, the larger electron injection barrier from 3TPYMB to EML is about

1 eV versus the injection barrier between NBPhen and T2T of 0.4 eV, along with a lower electron mobility of 3TPYMB can help shifting the recombination zone further toward the EML/ETL interface in Device B. Given that the triplet energy of UT-314 ($E_T = 2.4$ eV) is smaller than the triplet energy of Cu(I)-iBuPyrPHOS ($E_T = 2.8$ eV), having the recombination zone close to the HTL interface can lead to exciton quenching and efficiency roll-off. In summary, I attribute the 17% additional enhancement to the deeper HOMO, the larger triplet energy and better charge balance due to the 3TPYMB ETL.

2.11. Conclusions

In this chapter, I show that lowering the refractive index of the electron transporting layer reduces the optical loss due to dipole emission coupling into the cathode's plasmonic modes in two main ways. First following the dispersion equation of the SPP mode dependence on dielectric constant of the ETL and second by reducing the SPP-coupling following the Fermi's golden rule through requiring a thicker ETL for the case of the low refractive index ETL.

I further presented the discovery of the low refractive index of 3TPYMB. It is known that OLEDs employing 3TPYMB as ETL always have high efficiencies,[76][77][78][31] however, the reason for this superior performance was not understood. In this chapter, I presented that 3TPYMB has the lowest refractive index among commonly used ETLs and can dramatically enhance the light extraction efficiency.

Furthermore, I show how the quantum efficiency of a solution processed OLED using a TADF emitter is increased by 76% using 3TPYMB as the ETL. A low refractive index and a deep HOMO level and a large triplet energy, make 3TPYMB an ideal ETL for optimum light extraction.

It should be noted that the outlined optical and electrical designs here, for achieving high efficiency are applicable to other small molecule OLEDs as well.

2.12. Experimental Section

ITO substrates were cleaned in ultrasonic bath, first in acetone solution for 10 minutes and then in isopropanol for another 10 minutes. Next, the substrates were treated under UV-ozone for 10 minutes. PEDOT:PSS was spin casted at 4000 rpm for 40 seconds, followed by a 140°C thermal annealing in air for 20 minutes and another 160°C annealing in a nitrogen glovebox for 20 minutes. The solute concentration for HTL and EML was 7 mg.ml⁻¹ and 24 mg.ml⁻¹ in toluene and chlorobenzene, respectively. HTL and EML were sequentially spin casted at 4000 rpm for 45 seconds in a nitrogen glovebox. HTL was annealed for 20 minutes at 160°C in a nitrogen glovebox. The EML was not under thermal annealing. In order to remove the solvent in EML, the samples were kept in a high vacuum chamber overnight before the deposition of subsequent layers. Cu(I)-iBuPyrPHOS and PYD2 were provided by CYNORA (GmbH). T2T, NBPhen and 3TPYMB were purchased from Lumtec Incorporation. PLEXCORE UT-314 from Plextronics (Solvay) was used as the HTL. Ellipsometry measurement were carried out using a J.A. Woollam M-2000 ellipsometer. Ellipsometer data was fitted using J.A. Woollam WVASE software. Optical calculation was carried out using Setfos 4.4 software. Refractive index of PEDOT:PSS, PLEXCORE UT-314, and EML layers were assumed to be 1.5,[86] 1.6 and 1.6 respectively. Refractive indices of solution processed layers have been shown to be smaller than the evaporated films.[87] The refractive index of UT-314 from 1.5 to 1.9 shows a negligible effect (less than 5%) on the calculated light extraction, as shown in Figure 2.14. A larger refractive index for EML will result in more light extraction, as shown in figure 2.14. A Dirac delta distribution and a random

isotropic orientation is assumed for radiative dipoles. Spectral dipole power dissipation calculations were performed using the photoluminescence spectra obtained from the emitter.

Average mode distribution calculations were done at 550 nm.

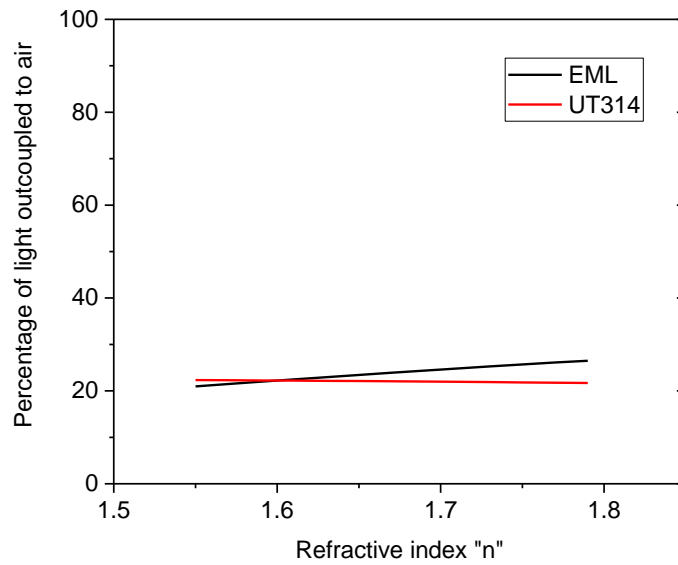


Figure 2.14. Effect of refractive index of UT-314 and EML on light extraction. Refractive index of UT314 has a small effect (<5%) on light extraction while assuming larger refractive index for EML will result in more light extraction.

CHAPTER 3

CHAPTER 3: Manipulating Refractive Index in Organic Light Emitting Diodes

3.1. Abstract

In the third chapter, I will continue building upon what I discussed in the previous chapter. I showed that reducing the refractive index of ETL can result in significant improvement in light extraction efficiencies of OLED devices. In this chapter I introduce a physical method by which refractive index of amorphous organic thin films can be reduced in a controlled manner, by pore inclusion. Oblique angle deposition (OAD) provides a straight forward way to manipulate the refractive index of a thin film by creating an ordered columnar void structure. However, before introducing this method to my OLED device fabrication, I carry out a systematic study of the effect of refractive index of each layer in an OLED multilayer, on optical loss and outcoupling. I further study effect of refractive index anisotropy on light extraction. I show that among all layers, refractive index of ETL plays the most important role on light extraction. Subsequently I fabricate an OLED device with an ultra-low index ETL layer and show a 30% increase in efficiency.

3.2. Introduction

In organic light emitting diodes (OLEDs), only a small fraction of light escapes from the device. A significant amount of the radiation is coupled to the bound photonic modes in the multilayered device and cannot be extracted to air or the substrate. The bound modes can either propagate in the bulk of the constituent thin films as waveguide modes or propagate along the metallic electrode interface as surface plasmon polaritons.

The density of both “leaky” and bound photonic modes in any optical multilayered stack is strongly dependent on the refractive indices of the organic as well as the ITO (Indium Tin Oxide)

layers.[61] I will show later that lowering the refractive index of the entire OLED stack to 1.5 can result in an extraction efficiency of almost 90% into the substrate and air. As for the individual layers in an OLED stack, lowering the refractive index of each layer can have a different impact on the specific loss channels. For instance, the SPP photonic mode dispersion is a strong function of the refractive index of the electron transport layer (ETL) which is the layer adjacent to the metal cathode.[46][20] A low refractive index ETL can significantly increase the light-outcoupling efficiency due to the reduced loss to surface plasmon polaritons.[20][66] In addition to the ETL, lowering the refractive index of the other organic and the ITO layers can reduce light coupling to the thin film guided modes and suppress Fresnel reflection from the boundaries. Therefore, the ability to manipulate the refractive index of the constituent layers of an OLED can significantly enhance the out-coupling efficiency.

3.3. Oblique Angle Deposition (OAD)

The refractive index of thin films can be reduced by pore inclusion using oblique angle deposition (OAD).[88][89][90] In the OAD process, substrates are positioned at an oblique angle with respect to the incident vapor flux. Upon adsorption of the initial vapor species on the substrate and formation of the first islands, self-shadowing of these islands prevents the vapor flux from reaching the shadowed regions, leading to an ordered, porous and columnar growth.[91] A schematic of oblique angle deposition, is shown in Figure 3.1. Self-shadowing can be controlled

via adjusting the angle of incident vapor flux. A wider angle results in a larger self-shadowing and therefore a larger porosity.

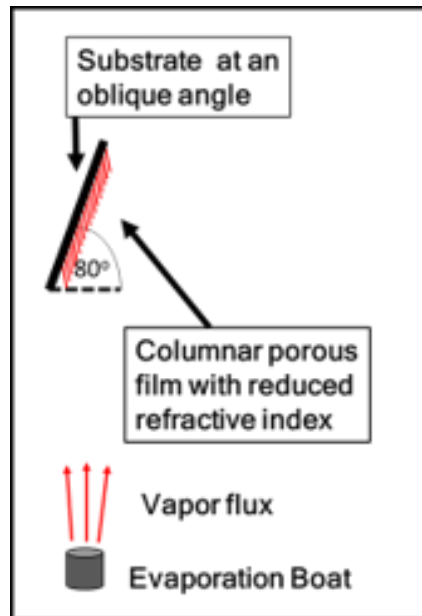


Figure 3.1. Schematic of Oblique Angle Deposition. A substrate is positioned at an oblique angle with respect to a collimated vapor flux. Upon initial islanding, a self-shadowing leads to an ordered porous columnar growth. The degree of porosity can be tuned by self-shadowing and therefore the angle which substrate makes with the vapor flux.

3.4. Fabrication of Porous Low Refractive Index OAD Films

Since the pore features are much smaller than the wavelength of the light, the resulting film does not scatter light.[88][89][91] Instead, it behaves as a homogeneous medium of void and solid material and the refractive index of the resulting film deposited by OAD can be significantly lower than that of the solid film.[88][90][91] The refractive index can be determined from the film porosity using an effective medium approximation (EMA) model[92][93] and the porosity can be tuned by the angle of incidence of the vapor flux. A larger angle leads to a larger self-shadowing and hence a larger porosity, and therefore OAD is a powerful tool to control the film porosity and hence the refractive index. This technique to deposit low refractive index films is applicable to most evaporable materials since it is a physical method and it merely depends on the surface

diffusion of the adsorbed species.[91] Low refractive index thin films, deposited using OAD have been reported for different transparent oxide materials, such as SiO₂ and ITO[94][93] and antireflection coatings using graded-index ITO thin films have been demonstrated in GaInN light emitting diodes.[89] While the use of OAD for OLEDs have been reported, the focus of the previous works was only limited to creating scattering surfaces to extract waveguide modes[94][95][96] and manipulating the refractive index of the organic layers for light extraction has not been explored. Here I show the low index ETL deposited by OAD can increase the external quantum efficiency (EQE) of a green phosphorescent OLED by nearly 30%.

3.5. Effect of Refractive Index of Each Individual layer in an OLED Device

A conventional OLED is comprised of an aluminum cathode, organic active layers including an electron transport layer (ETL), an emissive layer (EML), a hole transport layer (HTL), and an ITO transparent electrode on a glass substrate. Since reducing the refractive indices of the organic layers and the transparent anode can result in light-extraction enhancements.[20][66][65][97] I did optical simulations for an OLED to evaluate the effect of refractive indices of the constituent layers on light extraction. The device used for this optical study has the following structure: ITO (100 nm)/ TAPC (optically optimized thickness)/ CBP:Irppy2acac (20nm)/ Alq3 (optically optimized thickness)/ Aluminum (100nm). Here TAPC is Di-[4-(N,N-di-p-tolyl-amino)-phenyl]cyclohexane, CBP is 4,4'-Bis(carbazol-9-yl)biphenyl and Irppy2acac is Bis[2-(2-pyridinyl-N)phenyl-C](acetylacetonato)iridium(III). I varied the refractive indices of the constituent layers and calculated the maximum achievable EQE extracted to “air” (η_A) and to “air+substrate” (η_{A+S}) for 11 different cases, as presented in Table 3.1. In the case of the reference device, I calculated its light extraction efficiency using the actual refractive indices of the organic

as well as the ITO layers: $n_{ITO} = 2.1$, $n_{TAPC} = 1.68$, $n_{CBP} = 1.8$ and $n_{Alq3} = 1.75$. In the second and third cases, all layers have the same refractive index. For the rest of the cases, I kept the actual refractive indices of all the layers unchanged and only varied the refractive index of one constituent layer at a time to evaluate its effect on light extraction.

Table 3.1. Maximum achievable air (η_A) and air+substrate (η_{A+S}) EQEs.

Case	Reference Device	Device A	Device B	Device C	Device D	Device E	Device F	Device G	Device H	Device I	Device J
Refractive index of Anode (ITO)	2.1	<u>1.5</u>	<u>2.0</u>	2.1	2.1	<u>1.5</u>	<u>2.0</u>	2.1	2.1	2.1	2.1
Refractive index of HTL (TAPC)	1.68	<u>1.5</u>	<u>2.0</u>	1.68	1.68	1.68	1.68	<u>1.5</u>	<u>2.0</u>	1.68	1.68
Refractive index of EML (CBP)	1.8	<u>1.5</u>	<u>2.0</u>	1.8	1.8	1.8	1.8	1.8	1.8	<u>1.5</u>	<u>2.0</u>
Refractive index of ETL (Alq3)	1.75	<u>1.5</u>	<u>2.0</u>	<u>1.5</u>	<u>2.0</u>	1.75	1.75	1.75	1.75	1.75	1.75
Max Achievable Air (η_A)	31.6%	32.5%	21.0%	38.4%	25.2%	26.6%	31.0%	36.6%	25.0%	28.5%	32.5%
Max Achievable Air + Substrate (η_{A+S})	63.1%	87.8%	43.4%	73.2%	50.7%	69.4%	63.2%	63.0%	51.7%	59.4%	63.7%

Maximum achievable air (η_A) and air+substrate (η_{A+S}) for optically optimized OLED devices. All devices have the following structures: ITO (100nm) / TAPC (optically optimized thickness) / CBP:Irppy_{2acac} (20nm) / Alq3 (optically optimized thickness) / Aluminum (100nm). For the reference device, the following indices of refraction are used: $n_{ITO}=2.1$, $n_{TAPC}= 1.68$, $n_{CBP}=1.8$, $n_{Alq3}=1.75$ at 525 nm. To evaluate the effect of refractive index, η_A and η_{A+S} are calculated using different values of indices of refraction (under lined in the table) for different cases.

3.5.1. All Layers Having the Same Refractive Index

For the reference device, the maximum achievable η_A and η_{A+S} are 31.6% and 63.1% respectively. In Devices A and B, where the indices of all layers are equal to each other, as the refractive indices of all the organic and ITO layers are reduced from 2.0 to 1.5, η_A and η_{A+S} increase from 21% and 43.4% to 32.5% and 87.8% respectively. The results show that when the OLED stack is a homogeneous medium with an index of refraction of 1.5, η_{A+S} reaches almost 90% because of the elimination of thin film guided modes and Fresnel reflections and suppression of the SPP mode due to the low index ETL.

3.5.2. Electron Transporting Layer's Refractive Index

In the cases where I only changed the refractive index of the ETL in Devices C and D, I found that decreasing the ETL's refractive index from 2 to 1.5 increases η_A and η_{A+S} from 25.2% and 50.7% to 38.5% and 73.2% respectively. Compared to the other constituent layers, the refractive index of ETL has the largest impact on light extraction. An ETL with a low refractive index can dramatically increase the light extraction efficiency through suppressing the loss to surface plasmon polaritons, following the surface plasmon polaritons dispersion equation and the Fermi's golden rule.[20][66][65]

3.5.3. Transparent Anode (ITO) Layer's Refractive Index

In the cases where I only changed the refractive index of the ITO layer in Devices E and F, reducing the refractive index of ITO decreases the air contribution (η_A) but increases the overall air+substrate (η_{A+S}) contribution. The results are consistent with the previous results that using poly(3,4-ethylenedioxythiophene) polystyrene sulfonate (PEDOT:PSS) (refractive index of 1.5) as an anode can increase η_{A+S} to more than 60%.[97][98][99][41] In an OLED, the transverse electric waveguide (TEWG) mode centers at the ITO layer, and I will show later that reducing the refractive index of the ITO layer will extract this waveguide mode into the substrate mode.

3.5.4. Hole Transporting Layer's Refractive Index

In Devices G and H, where I changed the refractive index of the HTL, decreasing the refractive index of this layer from 2.0 to 1.5 increases η_A and η_{A+S} from 25.0% and 51.7% to 36.6% and 63.0% respectively. However, comparing Device G with the reference device, while η_A increases from 31.6% to 36.6%, there is no change in η_{A+S} . The lack of changes in η_{A+S} implies that lowering the refractive index of HTL will increase air contribution at the expense of a smaller substrate contribution.

3.5.5. Emissive Layer's Refractive Index

Finally, in Devices I and J where I changed the refractive index of EML, I found that the refractive index of EML has a very small effect on light extraction. However, unlike other layers, decreasing the refractive index of the EML has a negative effect on light-extraction. When the refractive index of the EML is smaller than that of the ETL, the entire dipole radiation will be coupled into the ETL, resulting in a slightly stronger coupling to the SPP loss modes of the metallic cathode. When the refractive index of the EML is larger than the ETL, there is total internal reflection (TIR) at the EML/ETL boundary and a portion of the dipole radiation is not coupled into the ETL due to the kinematic restriction of the wavevector. Moreover, the total radiated power by a dipole in an infinite dielectric medium is expressed as:[53]

$$P = \frac{e^2 \hbar k_0^3 n}{6 \pi \epsilon_0 m} \frac{1}{q_0} \quad (3-1)$$

Here, k_0 is the vacuum wave-vector, e is the elementary charge, m is the effective mass of the dipole, q_0 is the radiative quantum efficiency of the dipole and n is the refractive index of the medium. A larger n leads to a larger power radiated by the dipole.

3.6. Effect of Anisotropy in Refractive Index

3.6.1. Birefringence in Organic Thin Films

Majority of organic thin films show a uniaxial optical anisotropy, i.e. birefringence, with the refractive index having two components: 1. n_o , the ordinary component, also called “horizontal” or “in-plane of substrate” component, 2. n_e , the extraordinary component, also called “vertical” or “normal to the substrate” component. Birefringence is calculated by subtracting the ordinary component from the extraordinary component, i.e. $\Delta n = n_e - n_o$, see Figure 3.2. When n_e is larger than n_o , birefringence is called a “positive birefringence” and vice versa. as I will show later in table 3.2 majority of organic thin films show a negative birefringence .[40][20][100][101]

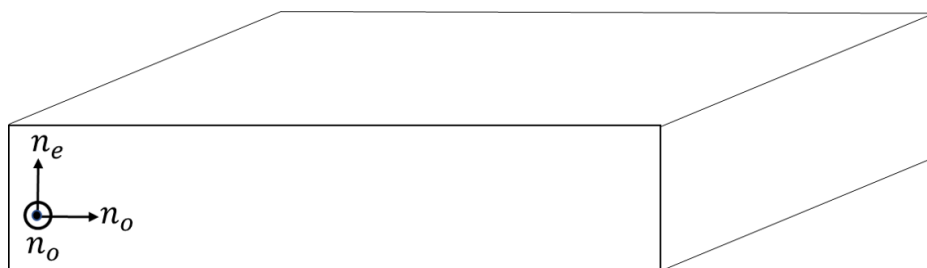


Figure 3.2. Demonstrating ordinary, n_o , and extraordinary, n_e , components of refractive index with respect to substrate.

3.6.2. Origins of Birefringence

Optical anisotropy is a consequence of anisotropy in the permittivity tensor, (dielectric constant) of organic thin films, meaning that polarization in the plane of substrate, i.e. ordinary polarization, is different with polarization normal to the plane of the substrate, i.e. extra-ordinary polarization. Yokoyama argued that the uniaxial anisotropy is due to two reasons: 1. Geometrical, anisotropic shape of organic molecules that comprises the thin film, and 2. An intermolecular hydrogen bonding that results in a preferred alignment of molecules.[101] Organic molecules with a linear rod-shape geometry would lead to thin films with negative birefringence, because of a larger polarizability along the molecular axis, see Figure 3.3.

Yokoyama also showed that increased birefringence in electron transporting organic thin films such as B3PYMPM and B4PYMPM, leads to decreased electronic disorder and increased charge carrier mobility.[101]

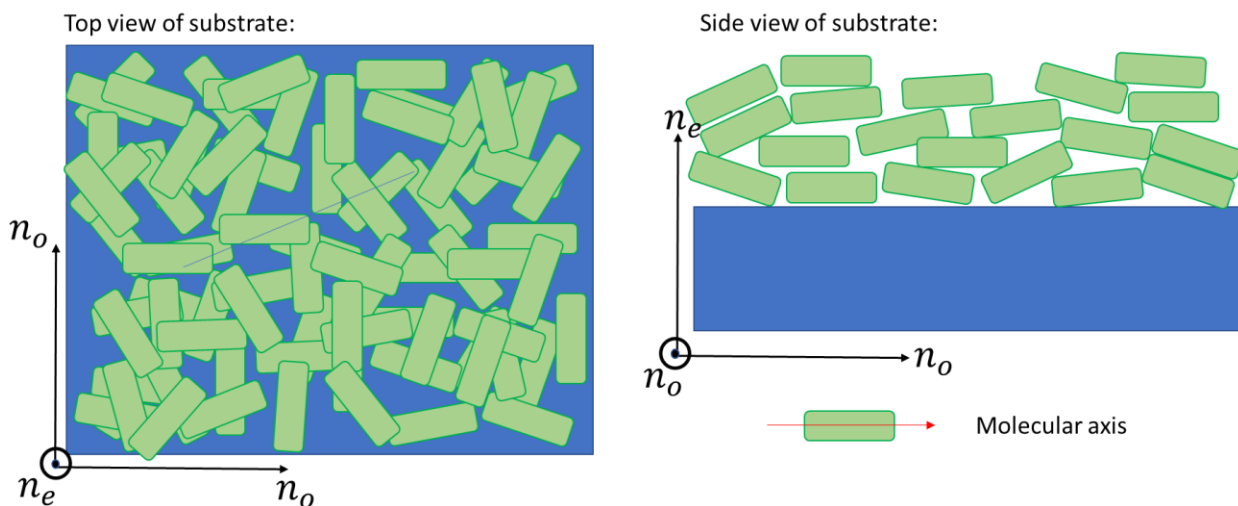


Figure 3.3. On the left, a schematic of top view of an anisotropic organic film, with negative birefringence, due to rod-shape geometry of organic molecule, is displayed. On the right, side-view (cross-section) of the film is illustrated. Organic molecules are represented as rod-shaped “sticks”, with the molecular axis being along the “stick”.

3.6.3. Anisotropy and Light Extraction in OLEDs

In a metal-dielectric optical microcavity (2D slab) such as a conventional OLED stack, bound eigen-modes can be categorized within two main polarization states, transverse magnetic (TM) polarization and transverse electric (TE) polarization. TM-polarized modes, such as SPP and TMWG, have their electric field mainly oscillating normal to the plane of substrate, and therefore TM-polarized modes interact with the extraordinary component of refractive index, n_e , for the most part. TE-polarized modes, on the other hand, have their electric field parallel to the plane of the substrate and therefore interact with the ordinary component of refractive index. Ergo it is expected to see a larger dependence of TE (TM) loss channels on n_o (n_e). Electric field direction and propagation direction of TE and TM polarized mode are depicted in figure 3.4.

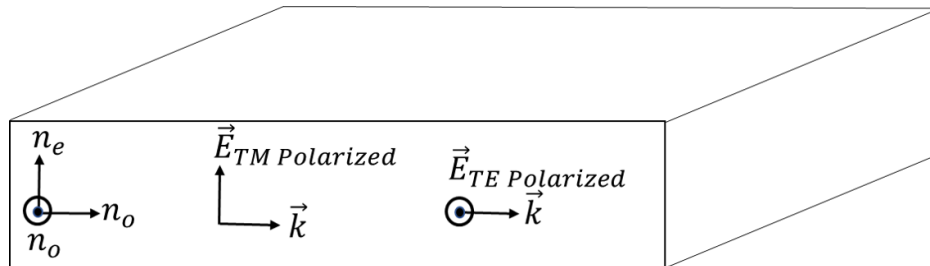


Figure 3.4. Both TE and TM polarized modes propagate in plane of the substrate (slab), i.e. have their \vec{k} vector in plane of the slab. However, the electric field component of the TE-polarized radiation lies in the plane of the substrate, making a complete overlap with the ordinary component of refractive index and normal to the extraordinary component of refractive index, while TM-polarized radiation is normal to the ordinary refractive index and overlaps completely with the extraordinary refractive index.

TM and TE polarized bound modes are not uniformly distributed in an OLED stack. For instance, in a conventional OLED stack which I studied in table 3.1, the first order TMWG and SPP modes have their highest intensity close to the metallic cathode and exponentially decay as the distance from cathode increases, and the first order TEWG mode, has its maximum intensity in the ITO layer, and decays going towards the cathode or the substrate, see figure 3.5. Therefore, the ordinary refractive index of ITO and HTL layers and the extraordinary component of ETL's

refractive index are expected to affect light extraction, since the TEWG modes are mainly distributed in HTL and ITO layers and the TMWG modes are mainly distributed in the ETL.

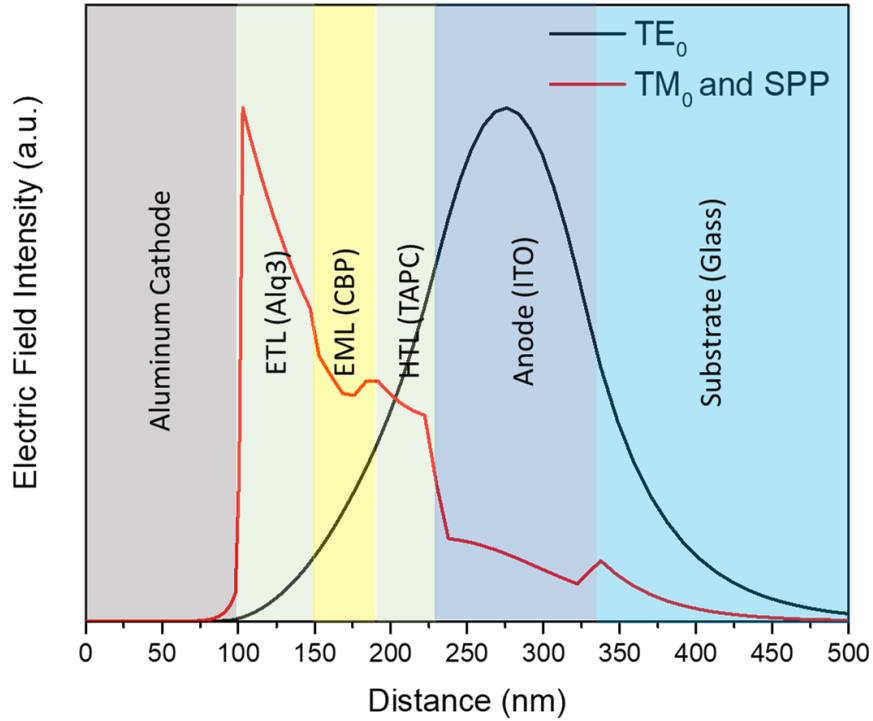


Figure 3.5. Distribution of intensity of lossy modes in a conventional OLED stack. TM-polarized modes, including SPP and $TMWG_0$ are mainly distributed near the metal cathode, therefore it is expected for refractive index of ETL to have the largest impact on TM-polarized modes. Since TM-polarized modes have their electric field normal to the plane of the substrate, as shown in figure 3.4, the extraordinary component of ETL is expected to have much larger impact on the modes rather than the ordinary component of the ETL's refractive index. $TEWG_0$ mode is mainly distributed in the HTL and ITO layer, and therefore refractive index of HTL and ITO is expected to mainly influence this mode. Since TE-polarized modes have their electric field parallel to the plane of the substrate, as shown in figure 3.4, it is expected for the ordinary refractive index of ITO and HTL to have much larger impact on light-extraction, rather than the extraordinary refractive index of the two layers. The mode distributions above is calculated using Lumerical software.

Optical simulations of light-extraction efficiency as a function of ordinary and extraordinary refractive indices of HTL and ETL are displayed in figure 3.6. As expected reducing the ordinary refractive index of HTL and extraordinary refractive index of ETL results in larger light-

extraction efficiencies. Isotropic low refractive index, results in the highest light extraction efficiency, however choosing from birefringent materials, positive (negative) birefringence is preferred for HTL (ETL). My results are also confirmed by Callens et al.[100]

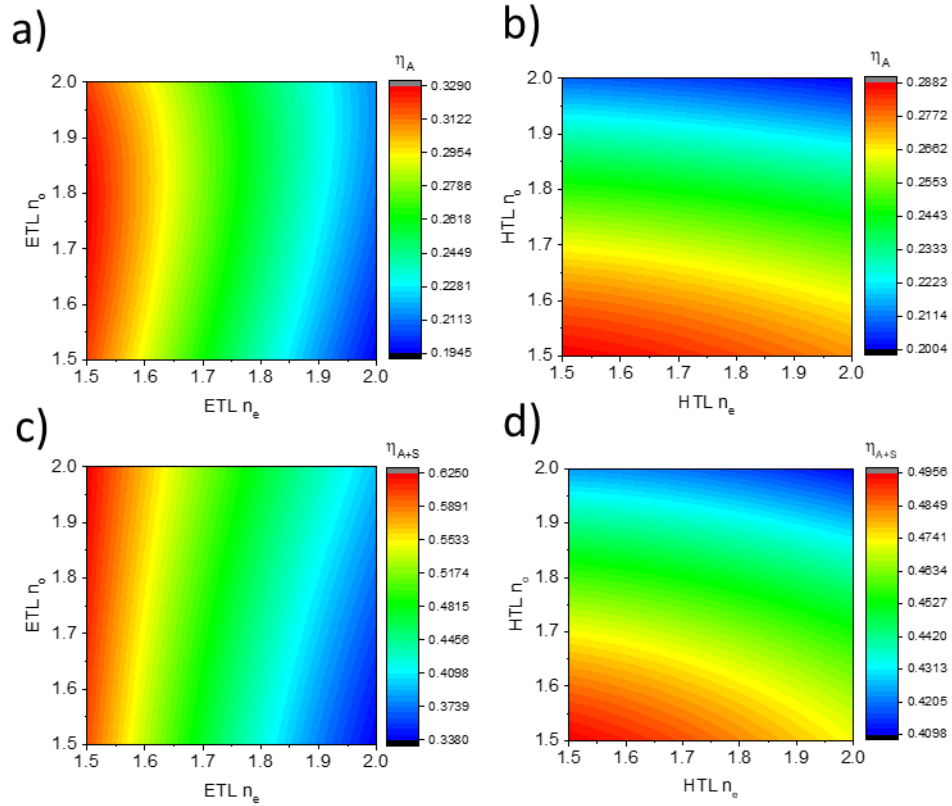


Figure 3.6. Calculated Air, η_A , contribution as a function of ordinary and extraordinary refractive indices of a birefringent: a) ETL, and b) HTL. Calculated Air+Substrate η_{A+S} contribution as a function of ordinary and extraordinary refractive indices of a birefringent: c) ETL, and d) HTL.

3.7. Ultra-Low Refractive Index Organic Layers using Oblique Angle Deposition

As the refractive index of the electron transport layer has the largest impact on light extraction, in this work I will attempt to reduce the refractive index of the ETL in an OLED device by OAD. I chose Alq3 as the electron transport material for my study. Alq3 has a moderate

isotropic refractive index of 1.75 at 525 nm. It has been previously shown that the refractive index of Alq3 can be tuned from 1.75 to 1.2 using OAD.[92]

3.7.1. Characterization of Porous Alq3 films Deposited using Oblique Angle Deposition

In my experiment, my OAD deposited Alq3 film at 80° degrees showed a reduced refractive index of 1.45 at 525 nm as determined by variable angle spectroscopic ellipsometry (VASE). A cross-sectional SEM image of the sample used for ellipsometry measurement is shown in Figure 3.7. A 1mm thick Si wafer with a 300nm thermal oxide layer was used as substrate. To measure the refractive index of the solid Alq3 film as well as the porous Alq3 film, first a 200nm thick solid Alq3 film was deposited at 0 degrees on the substrate and then a 700nm thick Alq3 film was deposited at 80 degrees on top of the solid Alq3 film, following Szeto et. al approach.[92] A general oscillator model based on Gaussian oscillators was used to determine the refractive index of the bottom solid Alq3 layer. A Bruggman effective medium approximation (BEMA) model based on the refractive index of the bottom solid Alq3 layer and void was then employed to determine the refractive index of the top porous Alq3 film.[92] Figures 3.8a and 3.8b show the dispersive optical constants of Alq3 when deposited at 0 degrees (normally) and at 80 degrees, respectively. Figure 3.8c shows the refractive index of Alq3 at 525nm as a function of the angle of deposition.

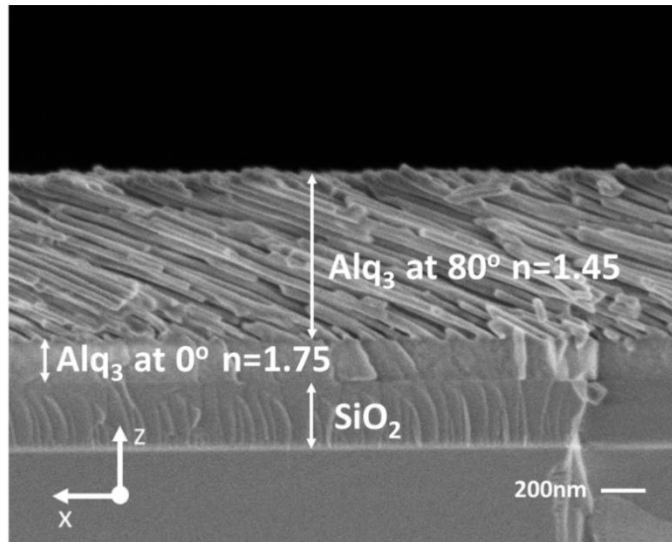


Figure 3.7. Cross-sectional SEM image of the sample used for ellipsometry measurement. Substrate is a 1mm thick Si wafer with 300nm of thermal oxide layer. A 200nm thick solid Alq₃ film at 0 degrees is first deposited to measure the refractive index of the solid Alq₃ film. Then a 700nm thick Alq₃ layer is deposited at 80 degrees on top of the solid Alq₃ film to measure the refractive index of the porous Alq₃ film. A Bruggeman Effective Medium Approximation (BEMA) model using the refractive index of the solid Alq₃ layer and void is used to find the refractive index of the porous film.

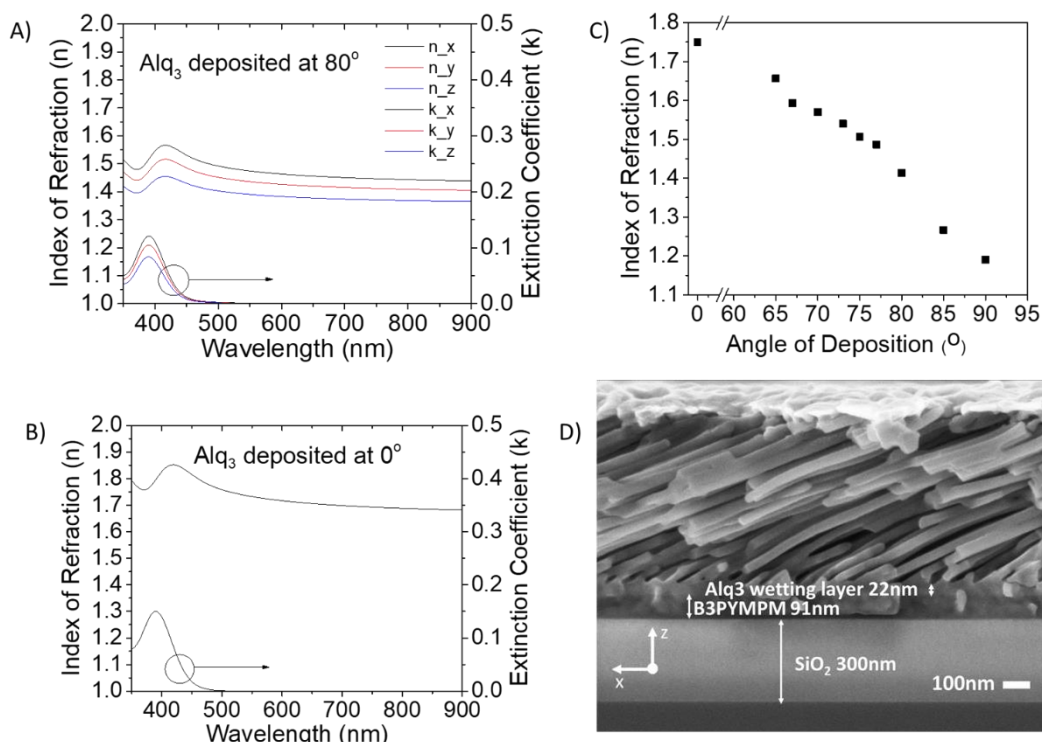


Figure 3.8. a) Optical constants of Alq₃ film deposited at 80°. b) Optical constants of Alq₃ deposited normally. c) Refractive index of Alq₃ deposited thin films as a function of angle of deposition at 525nm, from ref. [92] d) Cross sectional SEM image of ~ 600nm of Alq₃ deposited at 80° on top of 90nm B3PYMPM deposited at 0° on top of 300nm of SiO₂.

3.7.2. Formation of Wetting Layer

In oblique angle deposition, organic molecules can form an initial solid wetting layer when deposited at an oblique angle.[92][102][103][104] The formation of the wetting layer is due to the polar nature of organic molecules and polarity of the underlying surface, and can be completely avoided by rendering the underlying surface apolar through surface passivation.[103][104] In my OLED devices, Alq₃ is directly deposited on top of 4,6-Bis(3,5-di-3-pyridylphenyl)-2-methylpyrimidine (B3PYMPM). Subsequently, to measure Alq₃'s wettability on B3PYMPM, I deposited Alq₃ at 80° on top of a solid B3PYMPM film and measured the thickness of the wetting layer using cross-sectional SEM and VASE. I found that Alq₃ forms approximately a 20 nm-thick

wetting layer on top of B3PYMPM when deposited at 80 degrees. The cross-sectional SEM image is shown in Figure 3.8d.

3.7.3. Oblique Angle Deposition of Other Organic Thin Films

I also attempted oblique angle deposition of CBP and TAPC. However, the films did not show any porosity when oblique angle deposition was carried out at room temperature. This is due to the much lower glass transition temperature of TAPC and CBP compared to Alq3. According to Thornton's structure zone model (SZM),[105] the ratio between substrate temperature (T_s) and the melting temperature (T_m) of the evaporated material must be smaller than 0.2, i.e. $\frac{T_s}{T_m} < 0.2$, for a columnar porous film to form in OAD. The SZM is an empirical model explaining film morphology of mainly metal thin films,[91]:[106] and has been modified for other materials, such as oxides, composites, etc.[107]:[108] Although the melting temperature of Alq3 (441°C),[109] is much higher than TAPC (186°C) and CBP (283°C),[110] all three materials have $\frac{T_s}{T_m} < 0.2$ in room temperature, i.e. $T_s \sim 20^\circ\text{C}$, and are expected to form porous columnar structure according to the original SZM. However, as I mentioned earlier the SZM is an empirical model observed for metals. If we consider the glass transition temperature (T_g) of Alq3 (175°C),[111] TAPC (82°C),[110] and CBP (62°C) instead of the melting temperature,[112] then only Alq3 has the $\frac{T_s}{T_g} < 0.2$ criteria and can satisfy the condition for forming a columnar porous structure in room temperature. Porous columnar TAPC, CBP or any other organic thin films using OAD are attainable by lowering the temperature of the substrate. Fortunately, Alq3 is an electron transporting material and as I have shown above, refractive index of ETL has the largest impact on light extraction.

3.8. Optimized OLED Multilayer

For the OLEDs studied in this work, I used TAPC as the hole transport layer. TAPC is chosen for its high triplet energy ($T_1 = 2.9$ eV)[113] that can effectively block exciton diffusion. TAPC also has one of the lowest refractive indices among the commonly used HTL materials ($n = 1.68$ at 525 nm). The dispersive refractive indices and extinction coefficients of all the materials used in this study are presented in Figure 3.9. CBP is chosen as the host for its good charge balance when used in combination with my green phosphorescent emitter, Irppy2acac.[114] Here, a thin layer of B3PYMPM is used as the hole blocking layer, and Alq3 is used as the electron transport layer as mentioned before. I made two devices with the same structures and layer thicknesses: OAD Device with the Alq3 layer deposited at 80° and Control Device with the Alq3 layer deposited at 0° . The device structure for the both devices was: ITO (100nm)/TAPC (50nm)/CBP:Irppy2acac 1:0.07 (20nm)/B3PYMPM (10nm)/Alq3 (10nm)/Alq3:Cs₂CO₃ 1:0.05 (50nm)/Cs₂CO₃ (1nm)/Al. I doped the last 50 nm of the Alq3 film with Cs₂CO₃ in both devices with the same concentration to increase the ETL conductivity.[32] The OAD Device achieved a maximum EQE of 33.8%, which shows nearly 30% increase in efficiency compared to the Control Device with a maximum EQE of 26.4%. The current, voltage and luminance characteristics and the EQE of the devices are presented in Figure 3.10. The EQE was calculated from measured current efficiency and angular dependence of electroluminescence of the devices.

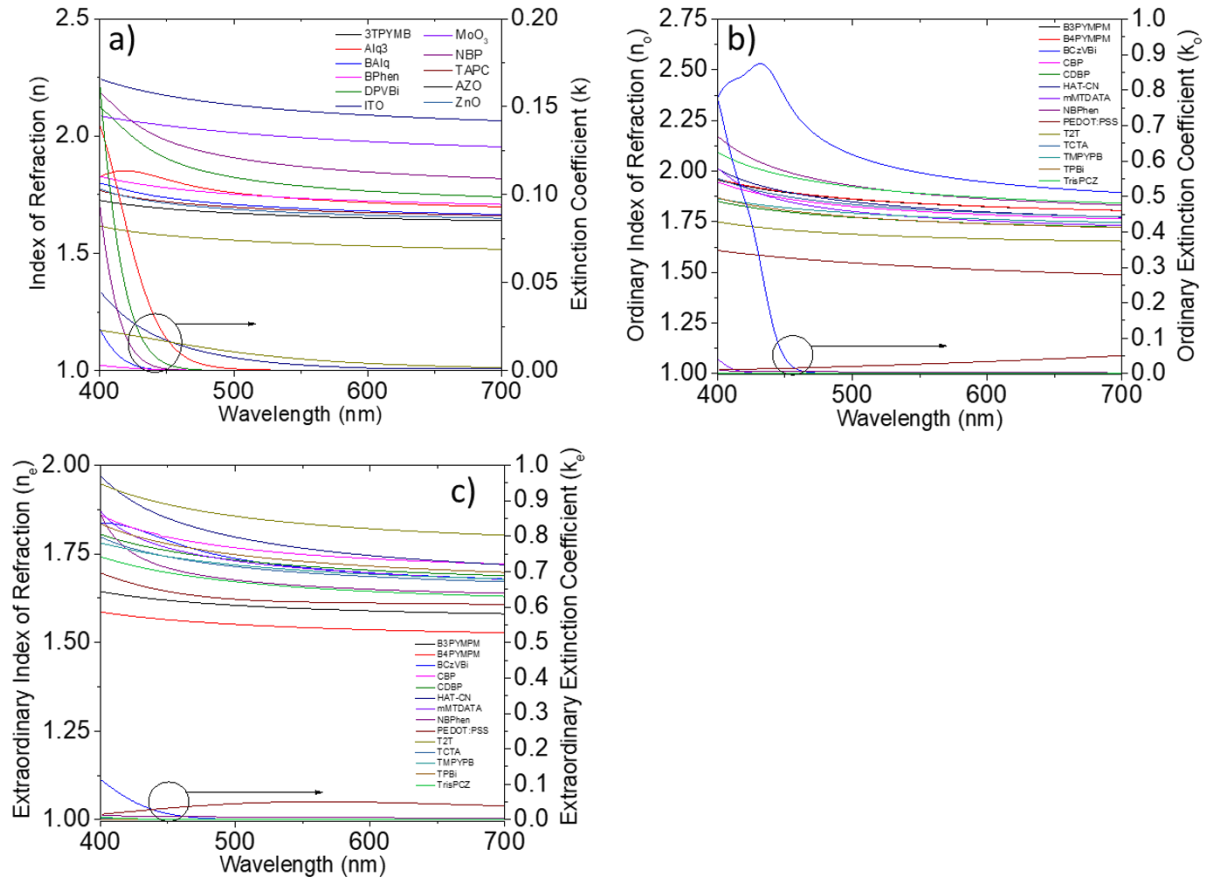


Figure 3.9. a) Dispersive refractive index and extinction coefficient of some of isotropic materials used in OLED devices. b) Dispersive ordinary refractive index and extinction coefficient of some of birefringent materials used in OLED device. c) Dispersive extraordinary refractive index and extinction coefficient of some of birefringent materials used in OLED devices.

3.9. Refractive Indices of Common Materials Used in OLED Devices

Refractive index of some of the common materials used in OLEDs are presented in Table

3.1. The dispersive refractive indices and extinction coefficients of all the materials used in this study are presented in Figure 3.9. Table 3.1 displays the refractive indices of some of commonly used materials in OLED stacks.

Table 3.1. Refractive indices of some of commonly used materials in OLED devices at 550nm.

Material	Complete Chemical name	Common Role	n_o ^{b)}	n_e ^{c)}	n ^{d)}	Ref.
3TPYMB	Tris(2,4,6-trimethyl-3-(pyridin-3-yl)phenyl)borane	ETL	N/A	N/A	1.65	Ref.[20]
Alq3	Tris(8-hydroxy-quinolino)aluminium	ETL	N/A	N/A	1.73	Measured.
AZO ^{a)}	Aluminum Zinc Oxide	Anode	N/A	N/A	1.59	Measured.
B3PYMPM	4,6-Bis(3,5-di(pyridin-3-yl)phenyl)-2-methylpyrimidine	ETL	1.84	1.59	N/A	Measured.
B4PYMPM	4,6-Bis(3,5-di(pyridin-4-yl)phenyl)-2-methylpyrimidine	ETL	1.84	1.54	N/A	Measured.
BALq	Bis(2-methyl-8-quinolinolate)-4-(phenylphenolato)aluminium	ETL	N/A	N/A	1.69	Measured.
BCP	2,9-Dimeth+B8:B29+B8:B28yl-4,7-diphenyl-1,10-phenanthroline	ETL	N/A	N/A	1.71	Ref.[115]
BCzVBi	4,4'-Bis(9-ethyl-3-carbazovylene)-1,1'-biphenyl	Emitter	1.99	1.71	N/A	Measured.
Bphen	4,7-Diphenyl-1,10-phenanthroline	ETL	N/A	N/A	1.73	Measured.
C60	(C ₆₀ -I _h)[5,6]fullerene	ETL	N/A	N/A	2.23	Ref.[115]
CBP	4,4'-Bis(carbazol-9-yl)biphenyl	Host	1.8	1.74	N/A	Measured.
CDBP	4,4'-Bis(carbazol-9-yl)-2,2'-dimethylbiphenyl	Host	1.75	1.71	N/A	Measured.
CzPA	9-[4-(10-phenylanthracen-9-yl)phenyl]carbazole	Host	1.79	1.76	N/A	Measured.
DPVBi	4,4'-Bis(2,2-diphenylethenyl)-1,1'-biphenyl	Host	N/A	N/A	1.78	Measured.
HAT-CN	Dipyrazino[2,3-f:2',3'-h]quinoxaline-2,3,6,7,10,11-hexacarbonitrile	HIL ^{e)}	1.81	1.76	N/A	Measured.
HfO	Haffnium Oxide	Dielectric	N/A	N/A	2.04	Measured.
ITO	Indium Tin Oxide	Anode	N/A	N/A	2.10	Measured.
IZO ^{a)}	Indium Zinc Oxide	Anode	N/A	N/A	2.12	Ref.[115]
mCBP	3,3-Di(9H-carbazol-9-yl)biphenyl	Host	N/A	N/A	1.74	Ref.[66]
mCP	1,3-Bis(carbazol-9-yl)benzene	Host	N/A	N/A	1.75	Ref.[66]
mMTDATA	4,4',4''-Tris(N-3-methylphenyl-N-phenyl-amino)triphenylamine	HTL	1.77	1.71	N/A	Measured.
MoO ₃	Molybdenum(VI) Oxide	HIL	N/A	N/A	1.99	Measured.
NBPhen	2,9-Bis(naphthalen-2-yl)-4,7-diphenyl-1,10-phenanthroline	ETL	1.87	1.69	N/A	Ref.[20]
NiO	Nickel Oxide	HIL	N/A	N/A	2.79	Ref.[115]
NPB	N,N'-Bis(naphthalen-1-yl)-N,N'-bis(phenyl)-benzidine	HTL	N/A	N/A	1.87	Measured.
P3HT	Poly(3-hexylthiophene-2,5-diyl)	HIL	N/A	N/A	1.89	Ref.[115]
PEDOT:PSS ^{a)}	Poly(3,4-ethylenedioxythiophene)-poly(styrenesulfonate)	HIL	1.52	1.61	N/A	Measured.
PO-T2T	2,4,6-Tris[3-(diphenylphosphinyl)phenyl]-1,3,5-triazine	ETL	N/A	N/A	1.71	Ref.[66]
sDPVBi	4,4'-bis(2,2'-diphenylvinyl)-1, 1'-spirobiphenyl	Host	N/A	N/A	1.78	Ref.[115]
T2T	2,4,6-tris(biphenyl-3-yl)-1,3, 5-triazine	HTL	1.67	1.83	N/A	Ref.[20]
TAPC	Di-[4-(N,N -di-p -tolyl-amino)-phenyl]cyclohexane	ETL	N/A	N/A	1.68	Measured.
TcTa	4,4',4''-Tris(carbazol-9-yl)triphenylamine	ETL	1.81	1.69	N/A	Measured.
TmPyPB	1,3,5-Tri[(3-pyridyl)-phen-3-yl]benzene	ETL	1.77	1.7	N/A	Measured.
TPBi	1,3,5-Tris(1-phenyl-1Hbenzimidazol- 2-yl)benzene	ETL	1.75	1.72	N/A	Measured.
TrisPCZ	9,9'-Diphenyl-6-(9-phenyl-9H-carbazol-3-yl)-9H,9'H-3,3'-bicarbazole	HTL	1.89	1.65	N/A	Measured.
ZnO ^{a)}	Zinc Oxide	ETL	N/A	N/A	1.67	Measured.

a) Solution processed films. b) n_o , stands for ordinary refractive index. c) n_e , stands for extraordinary refractive index. d) n , stands for isotropic refractive index. e) HIL stands for hole injection layer. Dispersive refractive indices of all measured materials are shown in Figure 3.9.

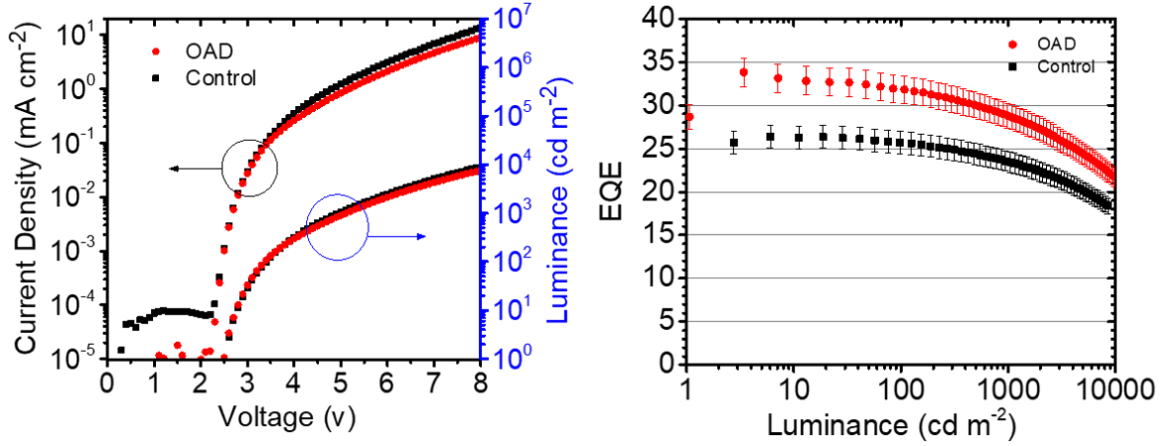


Figure 3.10. Device characteristic of OAD Device and Control Device.

3.10. Optical Simulation of Experimentally Fabricated Devices

3.10.1. Power Dissipation Calculations

To better understand the device optics, I did optical simulation using the SETFOS simulation software.[52] In my model, excitons are regarded as damped forced dipoles, driven by a reflected electromagnetic field from the metallic cathode.[46]:[39]:[52] Based on this model I can calculate the power dissipation of the dipoles as a function of the in-plane wavevector of the generated electromagnetic waves. Depending on the magnitude of the in-plane wave-vector (k_{in}), radiation can be categorized in four different regions.[39] In the first region, light with $0 < k_{in} < \frac{2\pi n_{air}}{\lambda}$ will escape the glass substrate and “leak” to air. Here, $\frac{2\pi n_{air}}{\lambda}$ is equal to 0.0119 nm^{-1} at $\lambda = 525 \text{ nm}$. The amount of radiation escaping to the air, i.e. air-mode, can then be calculated by integrating the radiation from $0 < k_{in} < 0.0119 \text{ nm}^{-1}$. When k_{in} becomes larger than $\frac{2\pi n_{air}}{\lambda}$, light will be totally-internally-reflected back into the glass substrate, and for $\frac{2\pi n_{air}}{\lambda} < k_{in} < \frac{2\pi n_{glass}}{\lambda}$, light is trapped in the glass substrate, this second region corresponds to the substrate-

mode. In the third region, where k_{in} becomes larger than $\frac{2\pi n_{glass}}{\lambda}$ light will be totally-internally-reflected from the glass/ITO boundary, and for $\frac{2\pi n_{glass}}{\lambda} \leq k_{in} < \frac{2\pi n_{EML}}{\lambda}$, radiation is coupled to the ITO-organic waveguide-mode. In the fourth region, where k_{in} becomes larger than the total magnitude of the wavevector in the organic thin film, i.e. $k_{in} > \frac{2\pi n_{EML}}{\lambda}$, the wavevector acquires an imaginary part and becomes evanescent.[56] Therefore light with $k_{in} > \frac{2\pi n_{EML}}{\lambda}$ is regarded as the evanescent-mode.

I calculated the power dissipation versus the in-plane wave-vector (k_{in}) as a function of refractive index of ETL at $\lambda = 525 \text{ nm}$. The calculation was done using the actual refractive indices for all the layers except for the last 40 nm of the ETL. The refractive index of the last 40 nm of the ETL was varied from 1.4 to 2. The results are shown in Figure 3.11a. In Region 4 of Figure 3.11a corresponding to the evanescent region of the power dissipation plot, we observe a major loss corresponding to the surface plasmon polariton (SPP) peak. The SPP peak is given by the SPP dispersion equation, $k_{in} = \frac{2\pi}{\lambda} \left(\frac{\epsilon_{cathode} \cdot \epsilon_{ETL}}{\epsilon_{cathode} + \epsilon_{ETL}} \right)^{\frac{1}{2}}$, [46] where $\epsilon_{cathode}$ is the dielectric constant of the metallic cathode and ϵ_{ETL} is the dielectric constant of the ETL. When the refractive index of the ETL is reduced, the radiation is shifted from the evanescent region toward the out-coupled region following the SSP dispersion equation, leading to a reduction of the TM-polarized loss modes, i.e. evanescent loss and TMWG, leading to an increased light outcoupling efficiency.[20]:[66]

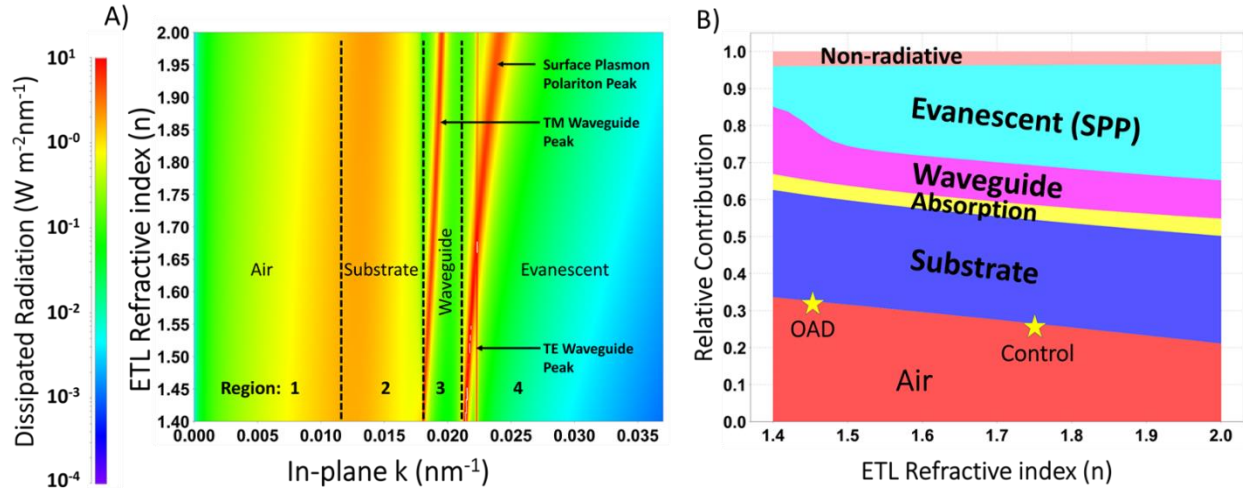


Figure 3.11. a) Power dissipation as a function of refractive index of the ETL and in-plane wavevector, at $\lambda=525\text{nm}$. Region 1 presents “air-mode”, region 2 presents “substrate-mode“, region 3 presents “waveguide-mode“ and region 4 presents “evanescent-mode“. b) Relative mode contribution calculated from the power dissipation. The star marks indicate the experimental maximum EQE achieved by OAD Device and Control Device. The calculations are based on the structure of OAD Device and Control Device. The refractive index of the last 40nm of the ETL (Alq3) layer was varied from 1.4 to 2.

3.10.2. Transvers Magnetic Modes

As I illustrated in Figure 3.5., Surface Plasmon Polaritons have a TM nature, that means that they have an oscillating electric field component normal to the surface of the metal. In the same manner, TMWG modes have their electric field normal to the plane of the substrate. This translates into both modes having their electric field mainly distributed in the dielectric layer next to the metal, i.e. the electron transporting layer. Therefore, any change in the optical properties of the ETL, is expected to significantly influence SPP and TMWG modes, as seen in Figure 3.11.

3.10.3. Transvers Electric Modes

Another peak in the evanescent region is the transverse electric waveguide (TEWG) peak, with less intensity compared to the SPP peak. The TEWG peak appears in the evanescent region, because it centers at the ITO layer, as manifested in Figure 3.5., and the refractive index of ITO is larger than the organic EML. The effect of the ETL refractive index is minimal on TEWG, since TEWG is centered at the ITO layer. However, reducing the refractive index of ITO can weaken or eliminate this peak altogether. It is worth noting that the refractive index of ITO can also be reduced using OAD.[89] Figure 3.12 shows the TE-polarized dipole power dissipation as a function of refractive index of ITO with the TEWG peak merging into the substrate-mode when the refractive index of ITO is reduced to 1.5.

Aside from the intensity of a mode, which is directly correlated with the refractive index, the electric field profile of the mode at the position of the dipole, determines the probability (intensity) of the dipole coupling to the mode. For instance, if we place an ultra-high index layer, which can sustain multiple waveguide modes, far enough from the EML, no radiation will be lost/coupled to the waveguide modes of the high index layer.

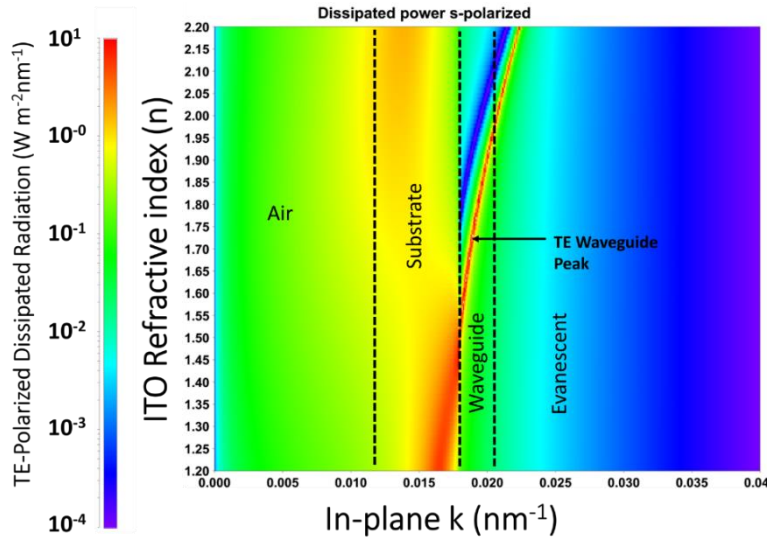


Figure 3.12. TE-polarized power dissipation vs. in-plane wavevector as a function of ITO refractive index.

3.10.4. Mode Distributions of Power Dissipation

I determined the relative contributions of different modes based on the calculated power dissipation in Figure 3.11a. The different mode contributions are shown in Figure 3.11b as a function of the refractive index of the ETL. As I explained above, reducing the refractive index of ETL increases the EQE due to reduced coupling to surface plasmon polaritons. The star symbols in Figure 3.11b are the experimental maximum EQEs achieved by the OAD Device and Control Device, indicating that lowering the ETL refractive index from 1.75 to 1.45 increases the out-coupling efficiency by 30%, which is in excellent agreement with my experimental results.

3.10.5. Validation of Effect of Low Index ETL in Electroluminescent Spectra

Given the optical constants and thicknesses of all the constituent layers and knowing the photoluminescence spectrum of the emitter, we can simulate the electroluminescent spectrum of an OLED device using transfer matrix formalism.[51][52] To further verify the effect of the low refractive index ETL, I simulated the electroluminescent spectra of the OAD Device and Control Device. In my simulation, I used Irppy2acac photoluminescence spectrum, and the actual measured refractive indices and thicknesses of the constituent layers in the OAD Device and Control Device as the input parameters. Both the experimental and simulated electroluminescent spectra are shown in Figure 3.13. The experimental electroluminescent spectra show a small blue shift on the right shoulder of the spectrum, going from the Control Device to the OAD Device. The same shift in the simulated spectra can be seen when the refractive index of the last 40 nm of the Alq3 layer is lowered from 1.75 to 1.45, further verifying the effect of the low refractive index ETL on the device performance.

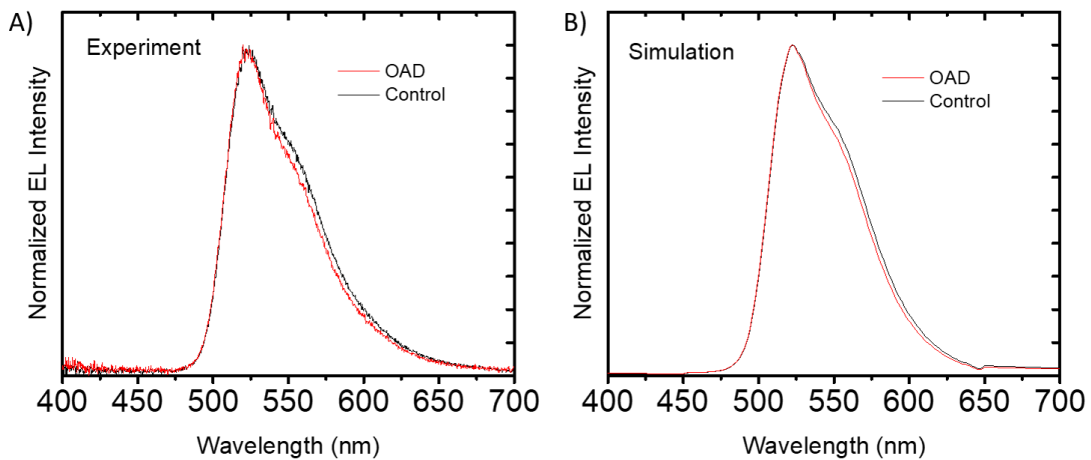


Figure 3.13. A) Experimental electroluminescence spectrum obtained from OAD Device and Control Device. B) Simulated electroluminescence spectrum of OAD Device and Control Device.

3.11. Conclusions

In the third chapter I did an in-depth study of the effect of refractive index of each single layer on light extraction in a conventional OLED stack. I discussed the origin of birefringence in organic thin films, and showed that the majority of organic thin films show a negative in-plane birefringence due to geometrical factors. The transverse magnetic loss modes in a conventional OLED stack, including TMWG and SPP modes have the largest contribution among all loss modes. I showed that TM-modes are largely distributed in the ETL close to the metallic cathode, and reducing refractive index of ETL can have a significant effect on suppressing these modes. Reducing refractive index of ETL has the largest impact on improving light extraction compared to other layers. Further I showed that the TEWG mode is mainly distributed in the ITO and HTL layers and reducing the refractive index of ITO layer can improve light extraction into the substrate, by suppressing the TEWG mode.

I discussed the effect of refractive index anisotropy on light extraction. I showed that the extraordinary (ordinary) refractive index of ETL (HTL) have the largest impact on light extraction, since the TM-polarized modes have their electric field normal to the substrate and therefore align with the extraordinary refractive index, while TE-polarized modes have their electric field parallel to the substrate and therefore align with the ordinary refractive index.

Oblique angle deposition (OAD), which is a physical method by which the refractive index of thin films can be reduced in a controlled manner, was introduced in this chapter. I show that the refractive index of a common ETL, Alq3, can be reduced to 1.45 when deposited at 80° using OAD. I then employ the low refractive index Alq3 layer in an OLED stack and achieve a 30% increase in efficiency, compared to the control device. To verify my experimental data, I did optical

simulation to study the effect of a low refractive index ETL on the evanescent loss and showed that the experimental data are consistent with my simulation results.

3.12. Experimental

Substrates were cleaned using ultrasonic bath, in acetone and isopropanol solutions. Vacuum pressure was kept under $2e-6$ torr during evaporation. A Woollam M2000 variable angle spectroscopic ellipsometer (VASE) was used for measuring the optical constants. WVASE software was used for ellipsometry modelling. All the organic materials were purchased from Lumtec incorporation. A field emission scanning electron microscope – FEI Verios 460L was used to obtain SEM images. EQE was measured from current efficiency and assuming a Lambertian distribution of emission. FLUXiM SETFOS 4.4 software package was used for optical calculations and simulations. Refractive index of all constituent layers was imported from real measured values using VASE. Irppy2acac photoluminescence spectrum was used in simulations.[57] An internal quantum efficiency of 95%, and horizontal orientation of 73% was assumed for the emitter, as reported elsewhere.[114]

CHAPTER 4

CHAPTER 4: Hyper-Fluorescent OLEDs with Sub-bandgap Operating Voltages

4.1. Abstract

In contrary to conventional understanding that a voltage equal or greater than the HOMO-LUMO gap of an organic molecule is required to achieve electroluminescent, in this chapter of this thesis, for the first time, I present overwhelming evidence, indicating that organic molecules with large triplet-singlet splitting, which show delayed fluorescence due to triplet-fusion, can have electroluminescence at voltages as low as half of their bandgap, by direct triplet exciton formation, without providing the voltage corresponding to the HOMO-LUMO bandgap. Based on the observed principle, a state-of-the-art hyper-fluorescent blue organic light emitting diode with ultra-low sub-bandgap operating voltages is presented with a performance comparable to the best TADF and phosphorescent blue OLEDs.

4.2. Introduction

4.2.1. Catastrophic Failure of Blue Phosphorescent and TADF OLEDs

Since the first invention of blue phosphorescent and thermally-activated-delayed-fluorescence (TADF) organic light emitting diodes (OLEDs), their operational lifetime has remained short for practical applications.[116]:[117]:[118]:[119] It is well understood that the short operational lifetime of these blue devices is due to the highly energetic triplet excited state of the emitter and even more energetic triplet excited state of the host materials used with these emitters. The triplet excitons on these emitters has undesirable annihilation with other triplet excitons or polarons, called triplet-triplet annihilation (TTA) and triplet-polaron annihilation (TPA), resulting in “hot” highly energetic excited states (>6.0 eV) and subsequently dissociation of organic bonds and degradation of the

OLED.[117][15][120] Added to the lifetime problem, TADF and phosphorescent OLEDs suffer from severe efficiency roll-off, and their external quantum efficiencies is usually less than half of its maximum value at practical required luminance ranges, due to the same destructive annihilation processes, i.e. TTA and TPA, which also further contributes to their short operational lifetime.[120][16][17] Moreover, the operating voltage of TADF and phosphorescent blue OLEDs is always larger than the energy of the triplet excited state of the emitter, which leads to low power efficiencies for blue devices.

4.2.2. Band-gap Energy “Requirement” for Exciton Formation in Organic Solids

As I discussed in the first chapter, to form excitons in organic materials via electronic excitation, electrons and holes must be injected to the frontier orbitals, i.e. the lowest-unoccupied-molecular-orbital (LUMO) and the highest-occupied-molecular-orbital (HOMO) of the emitting molecule in the emissive layer. Excitons form, when the injected electron-hole pair have a coulombic potential larger than the room-temperature kT , which is approximately a distance of $\sim 20\text{nm}$ apart from each other.[10][121][122] Upon formation, triplet and singlet excitons have the same degenerate energy state which is equal to the HOMO-LUMO gap energy, and as the electron and the hole approach each other, the triplet and the singlet energy levels split from one another. The magnitude of the singlet-triplet splitting is determined by the exchange energy or the HOMO-LUMO orbital overlap.[123][22] Although the triplet excitons can have much lower energy compared to the single excitons, to form either one, an energy equivalent to the HOMO-LUMO gap is required.

4.2.3. This Work’s Breakthrough

In this chapter I present overwhelming evidence, for the first time, that organic molecules with large triplet-singlet splitting, which show delayed fluorescence due to triplet-fusion, can have

electroluminescence at voltages as low as half of their bandgap, by direct triplet exciton formation, without providing the voltage corresponding to the HOMO-LUMO bandgap. Furthermore I present a state of the art blue hyper-fluorescent OLED with sub-bandgap turn-on voltage of 2.4 volts at 0.1 cd/m² and CIE(x,y) color coordinates of (0.15, 0.21), using direct triplet exciton formation and triplet-fusion on both the emitter and the host molecules. My device achieves 100 cd/m² at 2.9 volts and 1000 cd/m² at 3.4 volts, and a maximum external quantum efficiency (EQE) of 9.8% at 1000 cd/m² and a maximum power efficiency (PE) of 16.4 lm/W and a PE of 14.5 lm/W at 1000 cd/m².

I found that using a host and an emitter molecule, with both having a large singlet-triplet energy splitting and delayed fluorescence by triplet-fusion (p-type delayed fluorescence) sub-bandgap turn-on voltages and high PE and EQE can be achieved. The EQE and PE of my blue device is on-par with the state of the art blue TADF and phosphorescent OLEDs at practical luminance ranges, e.g. 500 cd/m² and higher. Not only my device is comparable with the best phosphorescent and TADF OLEDs, it also lacks the inherent problem that is responsible for the short operational lifetime of the blue phosphorescent and TADF OLEDs, that is the large, blue triplet energy states, >2.6 eV. My blue emitting molecule has a triplet energy of 1.94 eV and my blue host molecule has a triplet energy of 1.77 eV.

4.2.4. Triplet-Triplet Annihilation (Triplet-Fusion)

Triplet-triplet annihilation (TTA), also called triplet-fusion (TF), is an interaction where two triplet excitons annihilate and produce another triplet or singlet exciton with a higher energy. Due to the much longer exciton lifetime of triplet excitons compared to the singlet excitons, in fluorescent molecules, TF leads to a delayed fluorescence, also called “p-type delayed fluorescence”. Initially it was believed that a TF interaction would create a singlet exciton with a 25% probability and a triplet exciton with a 75% probability, following the spin statistics. However, Kondakov showed that TF can

produce radiative singlet excitons with a 100% probability, in systems where the first excited triplet state (T_1) is exactly half of the first excited singlet state (S_1), i.e. $2T_1=S_1$.^{[124],[125]} Monkman et al. observed that for efficient TF for singlet emission, the higher-order triplet states (T_n) must be larger than twice the first triplet state, i.e. $T_n>2T_1$.^[126] The most well-known material which satisfies all the energetic requirements for a 100% singlet yield from TF is rubrene, which was first reported by Kondakov.^[124] There are many organic single molecules that show delayed fluorescence due to TF, with different singlet production efficiencies and rates.^[127] Tetracene-based molecules, such as rubrene are known to have green-red delayed fluorescence due to TF and anthracene-based molecules such as 9,10-Diphenylanthracene (DPA) are known to have blue delayed fluorescence due to triplet fusion.^[125]

4.2.5. Exciplex Assisted Triplet-Fusion

Triplet excitons can be generated by energy transfer from a charge-transfer (CT) exciton or “exciplex”. OLEDs with electroluminescence at sub-bandgap voltages have been demonstrated before using a low-energy CT excited state, to transfer energy to the triplet state of the triplet-fusing (TF) molecule, e.g. rubrene or ADN (9,10-Di(naphth-2-yl)anthracene).^{[128],[129]} In these types of OLEDs there is always a requirement for a transport material, such as C60 or m-MTDATA (4,4',4'' -Tris(N-3-methylphenyl-N-phenyl-amino)triphenylamine), to form a low energy CT-state with the up-converting TF emitter, such as rubrene or ADN.^{[128],[129]} Figure 4.1 shows a schematic diagram of energy transfer and emission mechanism in such OLEDs. Although these devices can have electroluminescence at sub-bandgap voltages corresponding to the energy of the CT exciton, they are inherently flawed due to the emission from the exciplex and the energy down-flow (quenching) from the emitter to the CT-state, and therefore they fail to achieve any meaningful (>1%) EQE, and remain impractical.^{[128],[129],[130],[131]} In this work, I demonstrate that organic molecules with large

singlet-triplet splitting which exhibit p-type delayed fluorescence (triplet-fusion) such as rubrene, can form direct triplet excitons and show electroluminescence at sub-bandgap voltages, as low as their triplet energy, without the presence of any CT-excited or exciplex states, and be employed in devices with ultra-low sub-bandgap operating voltages and high efficiencies.

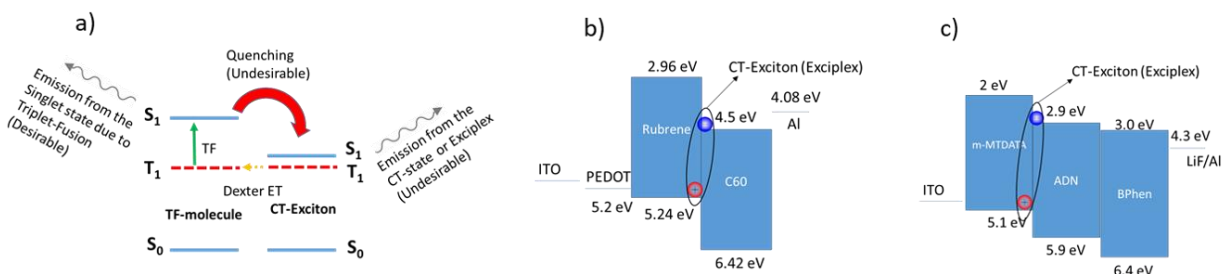


Figure 4.1. a) Energy transfer schematic and mechanism of previously reported OLEDs with electroluminescence at sub-bandgap voltages. Upon the formation of the low energy CT-excited, the energy is transferred to the triplet exciton of the emitter via Dexter energy transfer (ET). The triplet excitons on the emitter will then undergo fusion and excite a radiative singlet exciton through energy up-conversion b) and c) show two examples of OLED devices with sub-band gap electroluminescence. In the Rubrene device the CT-excited forms between Rubrene and C60 and then transfers to the triplet of the rubrene. In the ADN device the CT-excited forms between ADN and m-MTDATA and then transfers to the triplet exciton of the ADN molecule.

4.3. Results and Discussion

4.3.1. The Hyper-Fluorescent OLED with Sub-Bandgap Operating Voltage

In this section, I first present the characteristics of my efficient, optimized, blue fluorescent OLED which indicates electroluminescence at sub-bandgap voltages. I do a series of experiments to probe existence of any exciplex state between the transport layers and the emissive layer, and between the host and the guest molecules in the emissive layer of my optimized OLED. Eventually, I remove all the transport layers and characterize single-layer devices using a pure, undoped layer. After showing that the single-layer devices, using my emitter and host, show electroluminescence at sub-bandgap

voltages, I investigate more materials by making more single-layer devices and verify that the observed phenomena can be seen in a large class of materials.

4.3.2. Structure of the Multilayer Hyperfluorescent Device

The device structure for my optimized device is: ITO (50nm) / TAPC:MoO₃ 1:0.1 (30nm) / TAPC (20nm) / CzPA (3nm) / CzPA:BCzVBi 1:0.1 (30nm) / BCzVBi (3nm) / BPhen (30nm) / Cs₂CO₃ (1nm) / Aluminum (100nm). Here TAPC is 1,1-Bis[(di-4-tolylamino)phenyl]cyclohexane, CzPA is 9-[4-(10-phenyl-9-anthryl)phenyl]-9H-carbazole, BCzVBi is 4,4'-Bis(9-ethyl-3-carbazovinylene)-1,1'-biphenyl and BPhen is Bathophenanthroline.

4.3.3. Guidelines for Choosing the Emitter and Host Molecules

To achieve maximum efficiency from an electronic perspective, I followed three important guidelines in selection of my emitter and host molecules:

1. Both emitter and host molecules show p-type delayed fluorescence in pure form.
2. There is efficient Forster energy transfer from host to emitter: Overlap between host emission and emitter absorption.
3. Host molecules have a smaller triplet energy than the emitter molecules. In other words, diffusion of triplet excitons is from the emitter to the host and host molecules act as triplet traps.

From an optical perspective to have the highest efficiency, added to the above criteria for the emitter I made sure that the emitter has:

4. Preferred horizontal orientation of transition dipoles moment vectors.

The above points are further discussed below.

4.3.4. Anthracene-based Host with Small Triplet Energy

I used CzPA as my host, which has been previously reported in efficient blue fluorescent OLEDs with impressively long operational lifetime.[132] CzPA is the Diphenyl-Anthracene (DPA) compound, with a carbazole side group. DPA has been long known for photochemical up-conversion via TF in chemistry, and a carbazole group is known to help film amorphity and enhancement of hole carrier mobility.[133][134][135][136]

4.3.5. Horizontally Oriented Emitter with P-type Delayed Electroluminescence

I chose BCzVBi as my blue fluorescent dopant for three main reasons. First, I found that BCzVBi has a 90% horizontal orientation of transition-dipole-moment-vectors (TDMVs), as shown Figure 4.2, which leads to an increased light extraction efficiency, as I outlined in section 1.12.4. Second, due to the larger triplet energy of BCzVBi (1.94 eV) compared to CzPA (1.77 eV), triplet excitons will diffuse to the host molecules and have a larger annihilation (fusion) probability due to the larger concentration of the host molecules. Third, overlap between BCzVBi's absorption and CzPA's emission, as shown in Figure 4.3, would lead to Forster energy transfer (ET) from CzPA to BCzVBi. The device characteristics are shown in Figure 4.4. BCzVBi and CzPA have a HOMO-LUMO bandgap of 3.03 eV and 3.17 eV respectively and my device shows EL emission with photon energies up to 3.0 eV, yet the device turns-on at 2.4 volts (0.1 cd/m^2) and achieves a luminance of 100 cd/m^2 at 2.9 volts, as shown in Figure 4.4.

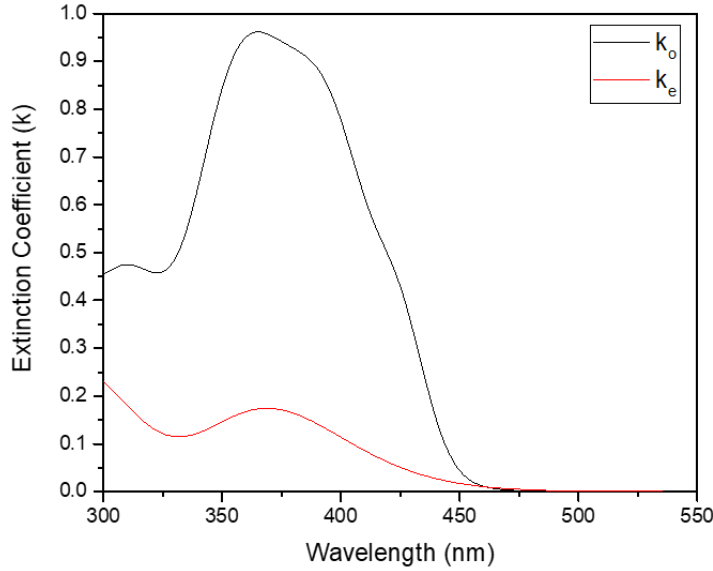


Figure 4.2. Ordinary and extraordinary extinction coefficient of BCzVBi thin film. I calculated the dipole orientation of BCzVBi in pure film, using the order parameter calculated from the equation: $S = \frac{k_e^{\max} - k_o^{\max}}{k_e^{\max} + 2k_o^{\max}} = \frac{3\Theta - 1}{2}$, where Θ indicates the ensemble average of vertically oriented transition dipole moments. The film showed $\Theta = 0.101$ or 89.9% horizontal orientation of dipole moments.

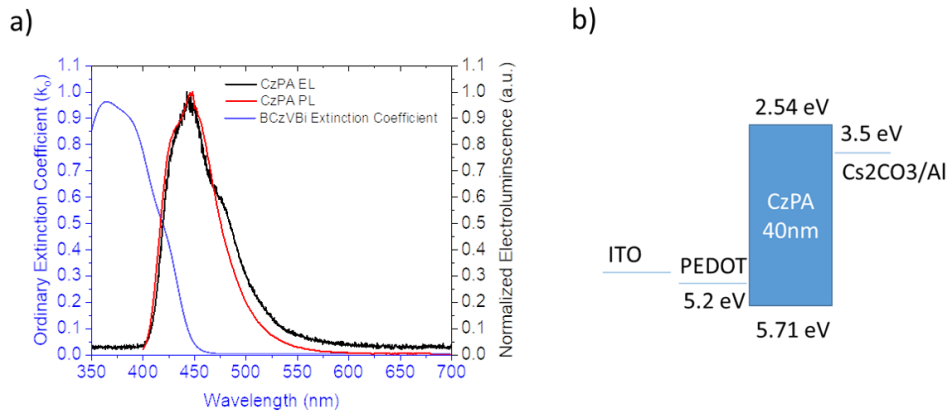


Figure 4.3. a) Overlap between absorption (extinction coefficient) of BCzVBi and PL and EL emission of CzPA, indicates efficient Förster energy transfer from singlet state of CzPA to the singlet state of BCzVBi. b) Device structure of the device corresponding to the EL spectrum of pure single-layer CzPA device shown in a).

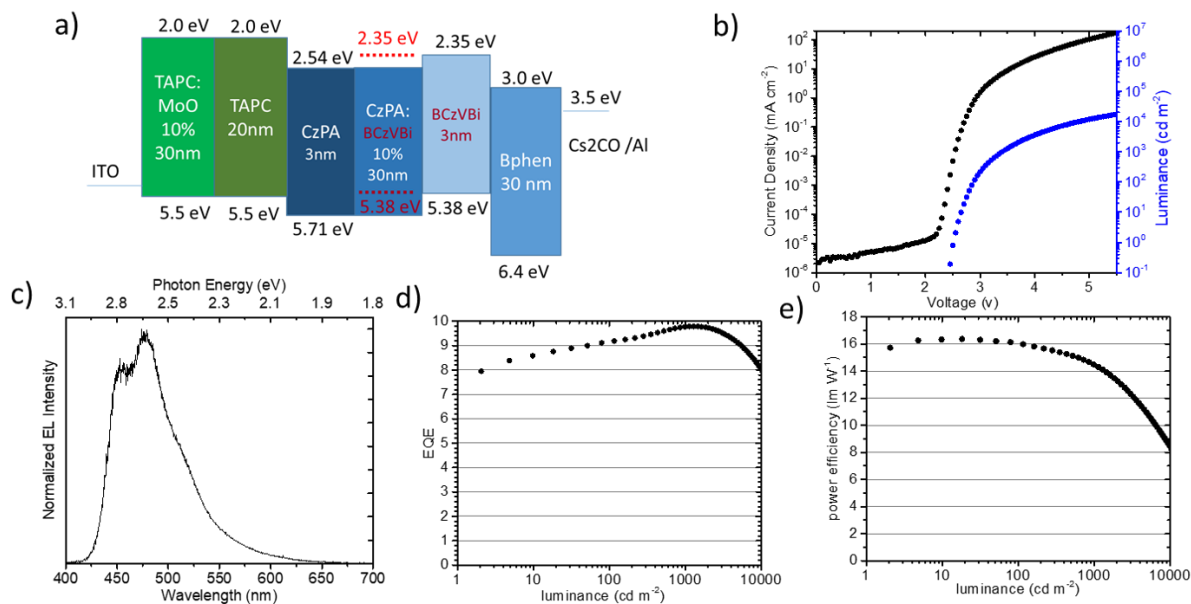


Figure 4.4. Device Characteristics: a) Device structure. b) JVL graph. c) Electroluminescent spectrum. d) External quantum efficiency. e) Power efficiency.

4.3.6. Investigation of Exciplex Formation

To investigate existence of any exciplex formation in my device, that may be activating triplet states of either the host or the emitter, I first examined electroluminescent (EL) spectrum of my OLED at different voltages. The emission from a low-energy exciplex state would dominate the EL spectrum, specially at sub-bandgap voltages close to the exciplex energy, if there is a low-energy exciplex which is responsible for the energy transfer to the triplet-state of the emitter or the host. Such dramatic changes in EL spectra as a function of voltage has been previously reported for exciplex-based devices with EL at sub-bandgap voltages.[129] However as shown in Figure 4.5., I did not observe any changes in the EL spectra of my optimized device as a function of the voltage.

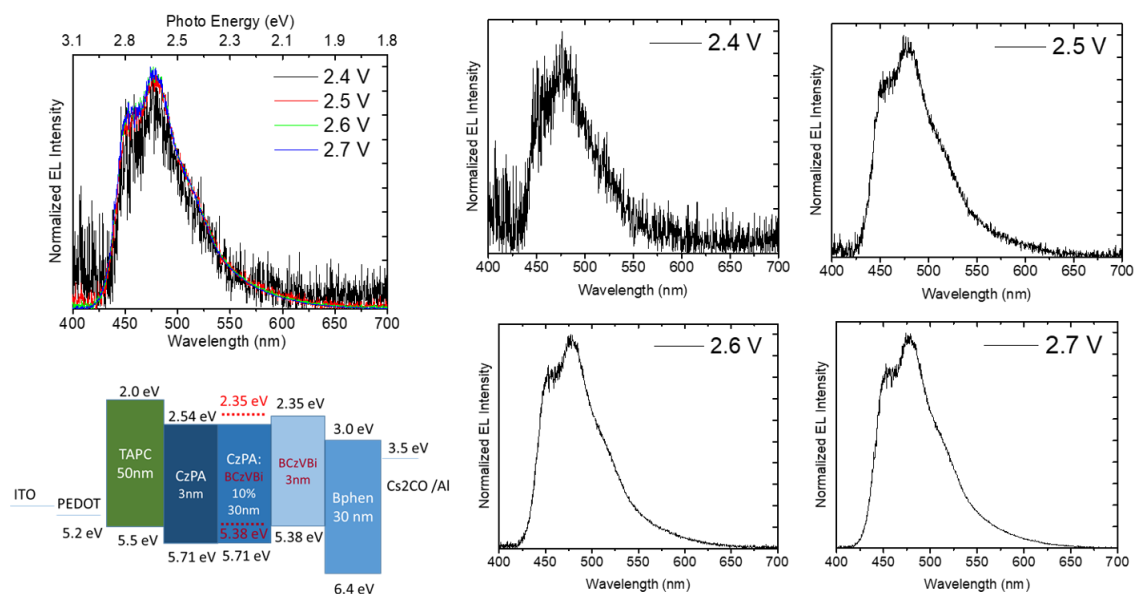


Figure 4.5. OLED device structure and the electroluminescent spectra of the optimized device at different voltages. A low energy exciplex emission would dominate the EL spectra specially at low voltages. Lack of change in the EL spectra as a function of voltage refutes existence of any exciplex state.

To see if either the host molecule (CzPA) or the emitter molecule (BCzVBi) is forming any CT or exciplex state with either the hole transporting layer (HTL), TAPC, or the electron transporting layer (ETL), BPhen, I made four different devices, putting a thin layer of pure emitter or host at the TAPC and BPhen interfaces. The device structures and characteristics are shown in Figure 4.6. As it can be seen in Figures 4.6, all four devices show visible EL at 2.4 volts and have similar EL spectra, indicating lack of any exciplex formation between either the guest or host molecules and the transport molecules. If exciplex formation between the host/emitter and the HTL/ETL was responsible for the

2.4 volts turn-on voltage, at least one of the four devices shown in Figure 4.6 should have indicated a higher turn-on voltage compared to the others.

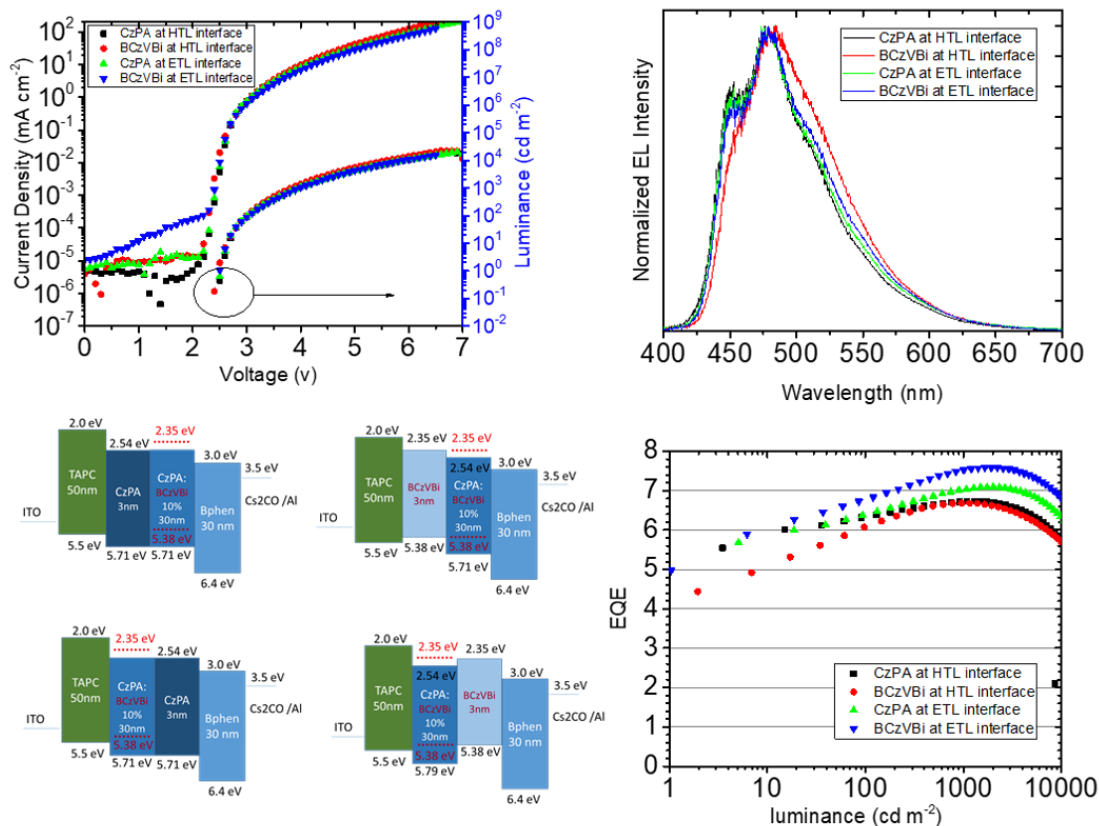


Figure 4.6. Device structures and characteristics of OLEDs with a thin layer of pure host (CzPA) or emitter (BCzVBi) at the HTL (TAPC) or ETL (BPhen) interfaces.

Furthermore, I made another four devices using emitter/host and host/emitter bilayers and pure emitter and pure host in the emissive layer between TAPC and BPhen, to see if there are any exciplex formation between the host molecule and the emitter molecule. The device characteristics, structures and EL spectra at different voltages are shown in Figures 4.7, 4.8, 4.9, 4.10 and 4.11. The lack of change in EL at different voltages, specially at sub-bandgap voltages, again points to an exciplex-free guest host system as seen in Figures 4.8, 4.9, 4.10 and 4.11.

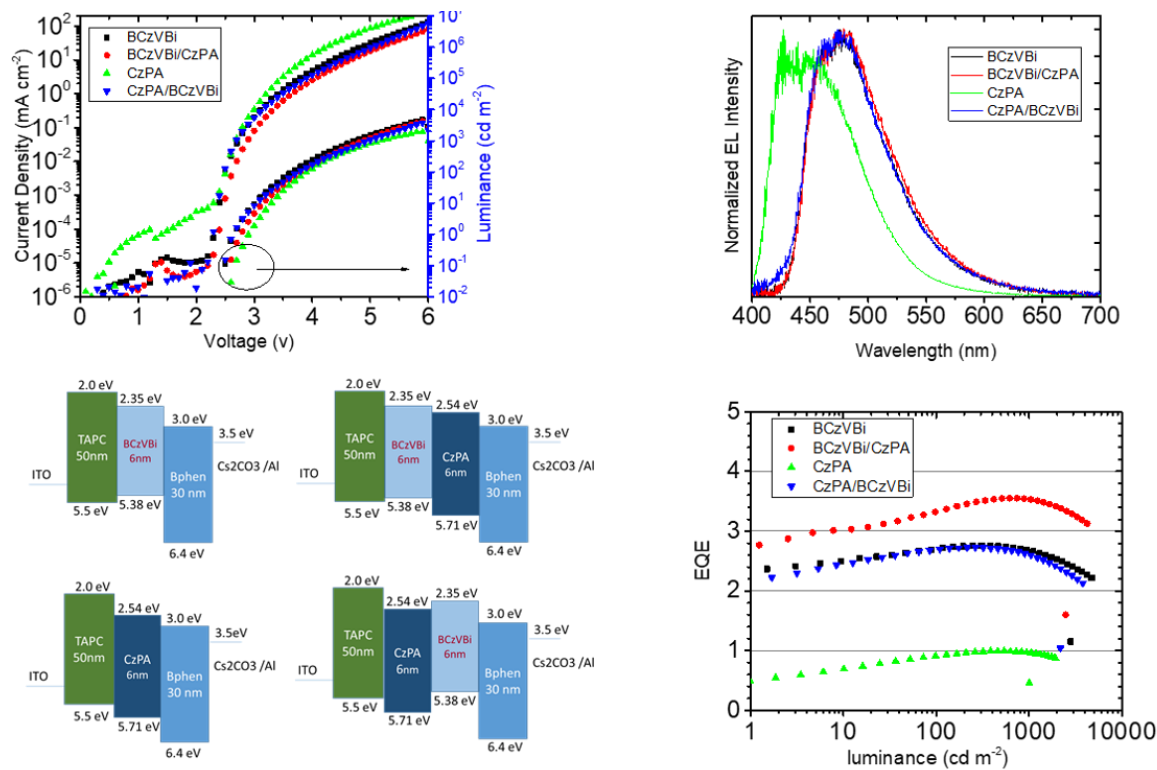


Figure 4.7. Device structures and characteristics of OLEDs with pure host (CzPA) or emitter (BCzVBi) at the HTL (TAPC) or ETL (BPhen) interfaces.

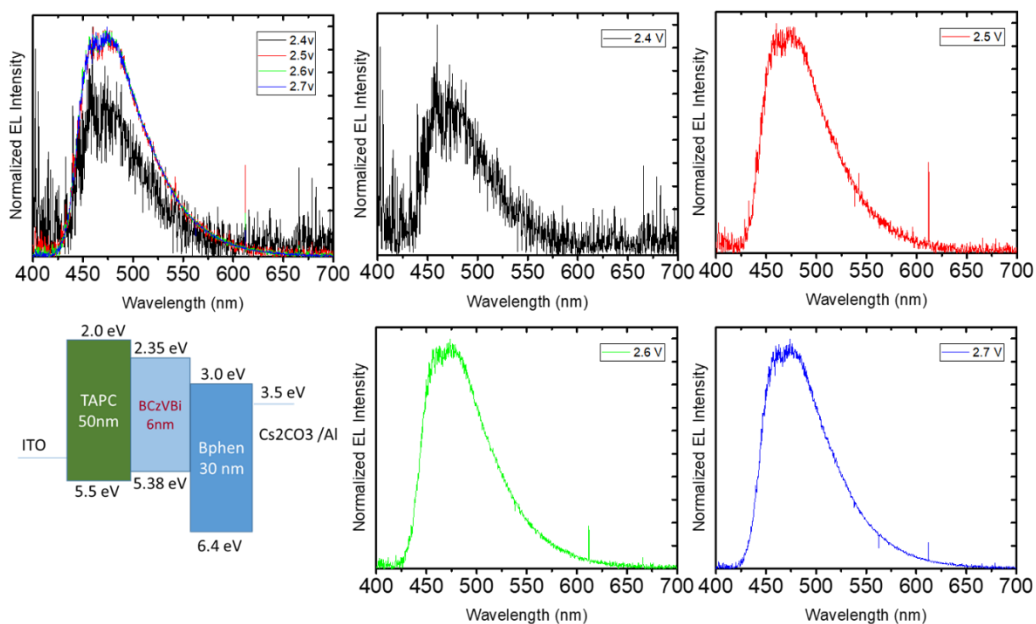


Figure 4.8. Device structure and EL spectra at different voltages of the OLED device made of pure BCzVBi EML between TAPC and BPhen.

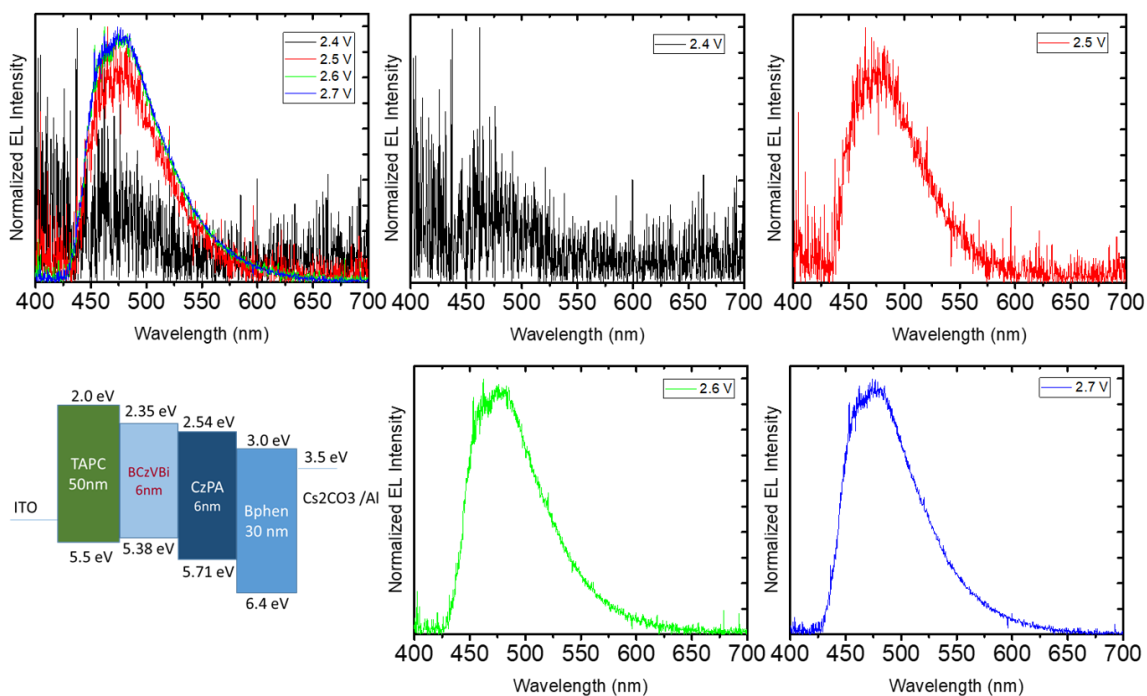


Figure 4.9. Device structure and EL spectra at different voltages of the OLED device made of pure BCzVBi/CzPA bilayer EML between TAPC and BPhen.

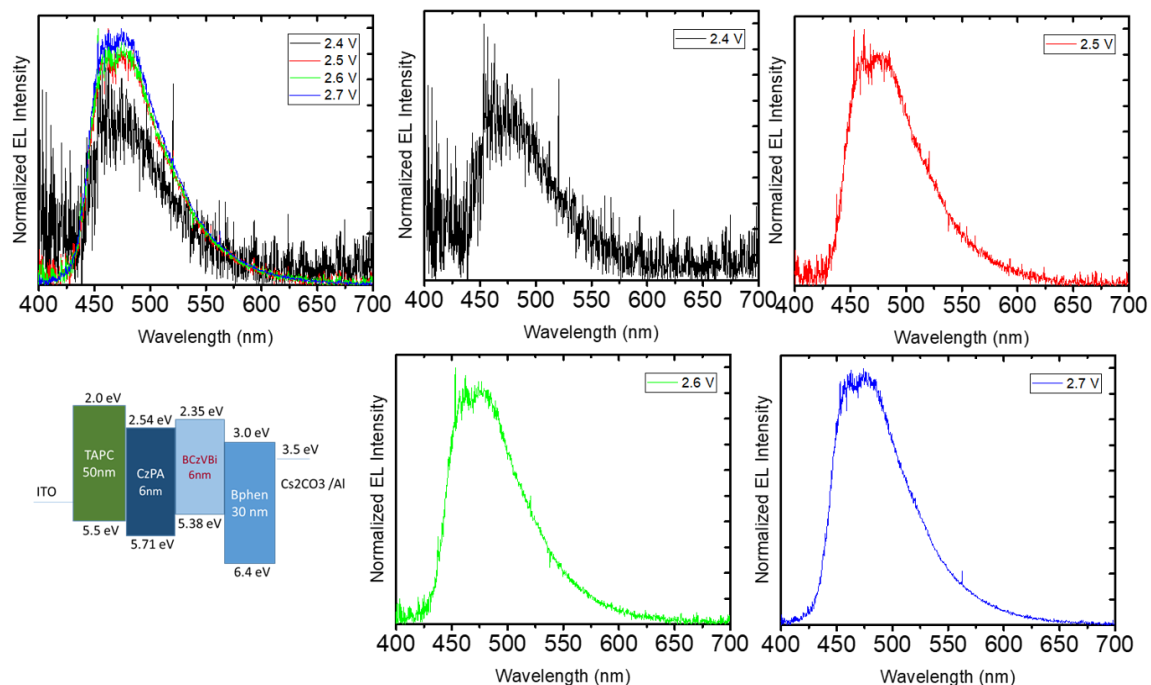


Figure 4.10. Device structure and EL spectra at different voltages of the OLED device made of pure CzPA/BCzVBi bilayer EML between TAPC and BPhen.

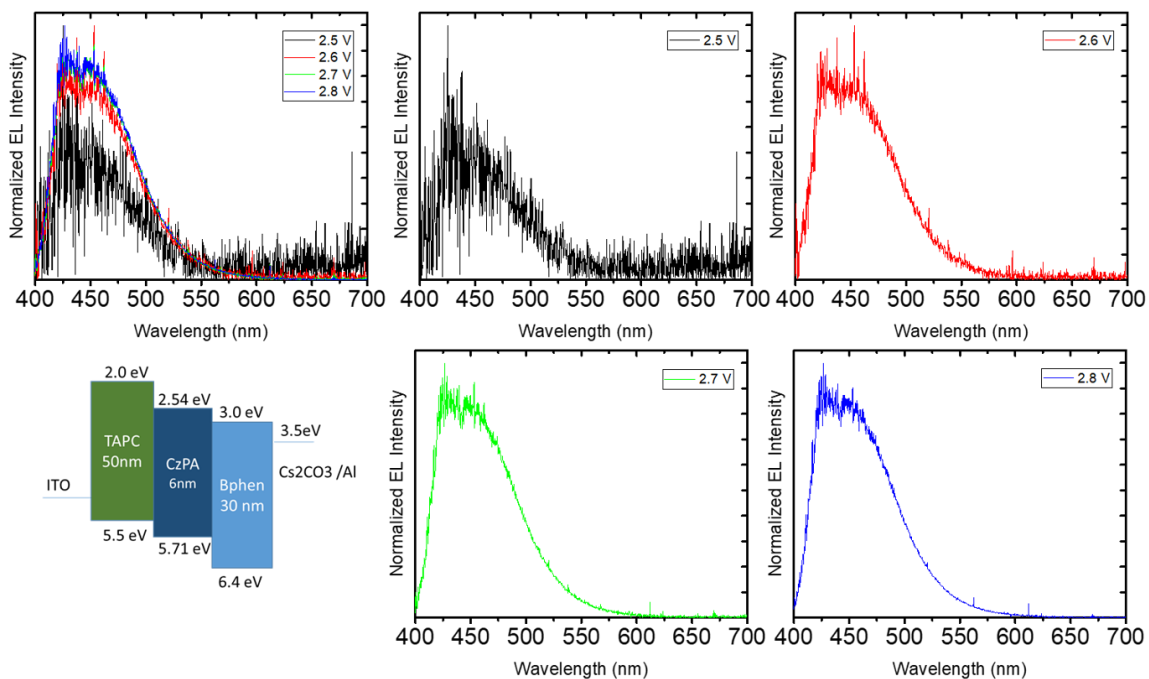


Figure 4.11. Device structure and EL spectra at different voltages of the OLED device made of pure CzPA EML between TAPC and BPhen.

4.3.7. Single-layer OLEDs

After not observing any emission from any low-energy CT-excitons to justify the electroluminescence at sub-bandgap voltages, I decided to remove the HTL (TAPC) and ETL (BPhen) and make single-layer devices. The structure of the single-layer devices was: ITO/ PEDOT (30nm) / pure layer of emitter (or host) (40nm) / Cs₂CO₃ (1nm) /Aluminum (100nm). In this work PEDOT refers to PEDOT:PSS with chemical formula of: poly(3,4-ethylenedioxythiophene) polystyrene sulfonate, and is used as the hole injection layer (HIL).

Surprisingly, for the single-layer device, using BCzVBi, I observed electroluminescence at voltages as low as 2.1 volts, with emitted photon energies up to 3.0 eV. Figure 4.12a shows the device's current density and photocurrent versus bias voltage. To detect the electroluminescence, I used two detectors; a photomultiplier tube (PMT) detector for low light intensities and a Si-photodiode for higher light intensities. The photocurrent corresponding to a luminance of 0.1 cd/m² is marked on the graph in Figure 4.12a. Figure 4.12b shows the molecular structure of BCzVBi and device structure of the single-layer OLED using BCzVBi. Figure 4.12c shows the EL spectra of the device. I observed no change in the EL spectra of the device as a function of voltage, as shown in Figure 4.13.

In the context of photo-chemical TF-upconversion it is well understood that the upconverted photoemission has a quadratic/linear dependence on the input excitation intensity.[137] Kondakov and others also observed a quadratic/linear behavior of the photocurrent (light intensity) as a function of current-density for low/high driving currents, namely “quadratic regime” vs. “linear regime”, in OLEDs with TF.[125] Figure 4.12d and 4.12e show the “quadratic regime” and the “linear regime” for the BCzVBi single-layer device, indicating a TF mechanism. Beside the quadratic/linear behavior, another proof of emission due to TF is delayed electroluminescence after device turn-off, which is shown in Figure 4.12f, for the case of the BCzVBi device.

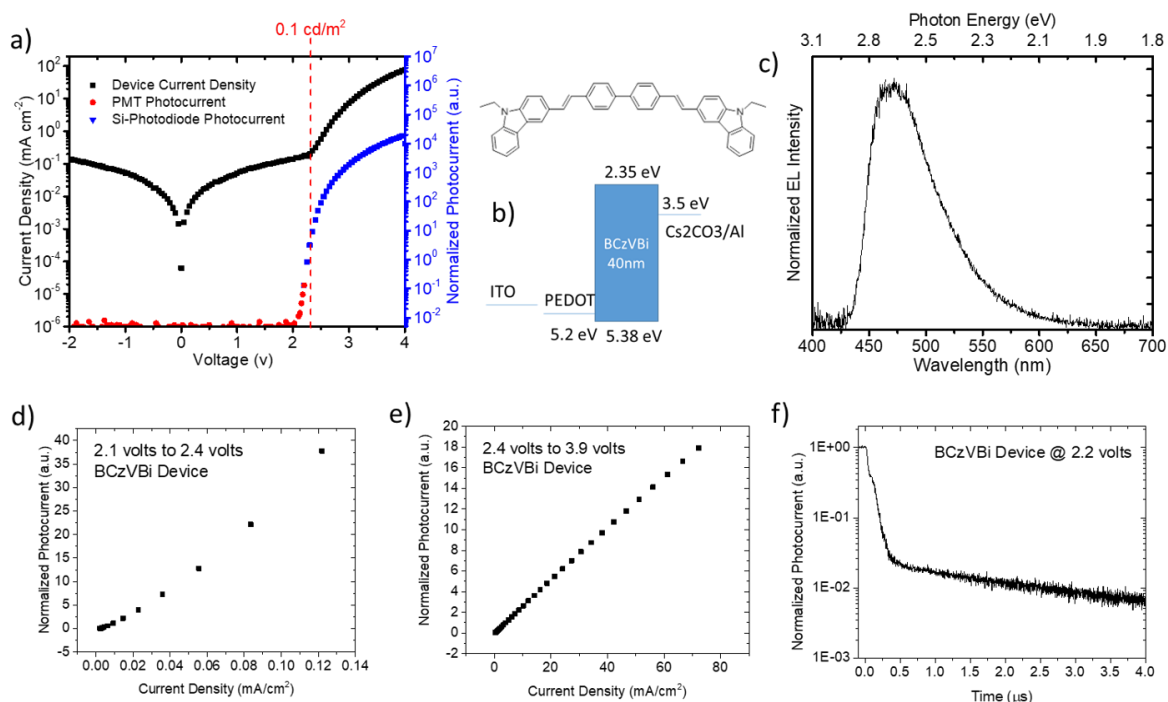


Figure 4.12. a) Device current density and photocurrent versus bias voltage. Two detectors were used to detect the electroluminescence; a photomultiplier tube (PMT) was used for low light intensities and a Si-photodiode was used for higher light intensities (due to PMT saturation). The photocurrent corresponding to a luminance of 0.1 cd/m² is marked on the graph. b) Molecular structure of BCzVBi and device structure of the OLED with a single-layer of BCzVBi. c) Electroluminescent (EL) spectra of the device. d) Photocurrent vs. current density in the low voltage region showing a quadratic behavior, which is indicative of emission due to triplet-fusion, “quadratic regime”. e) Photocurrent vs. current density in the high voltage region showing a normal linear behavior, “linear regime”. f) Transient EL dynamic of the device after turn-off shows microsecond scaled delayed fluorescence which is indicative of fluorescence due to triplet-fusion. A reverse bias of -5.0 volts was applied at the onset of turn-off.

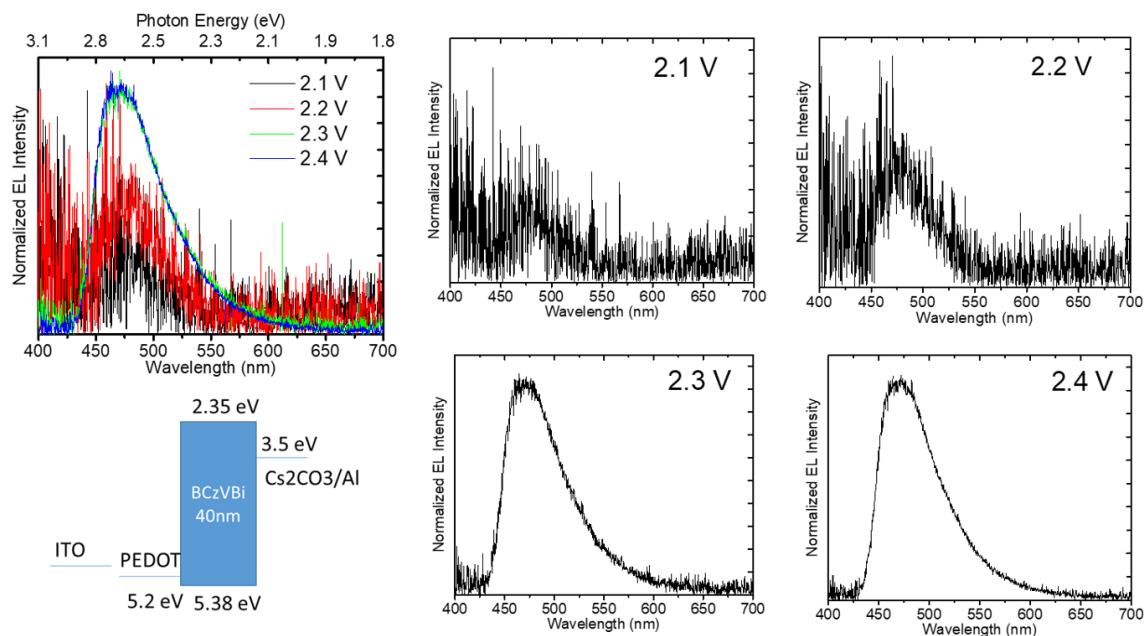


Figure 4.13. Device structure of the BCzVBi single-layer device and its EL spectra at different voltages.

I made another single-layer OLED using CzPA. Device characteristics of the CzPA single-layer device are shown in Figure 4.14. The CzPA single-layer device showed electroluminescence at voltages as low as 2.35 volts. Similar to the BCzVBi single-layer device, the photocurrent vs. the current density of the CzPA device shows quadratic behavior for low current region and linear behavior for the high current region, and the transient EL of the device shows microscale delayed fluorescence, indicative of emission due to triplet-fusion. EL spectra of the CzPA single-layer device also shows no change at different voltages, as shown in Figure 4.15.

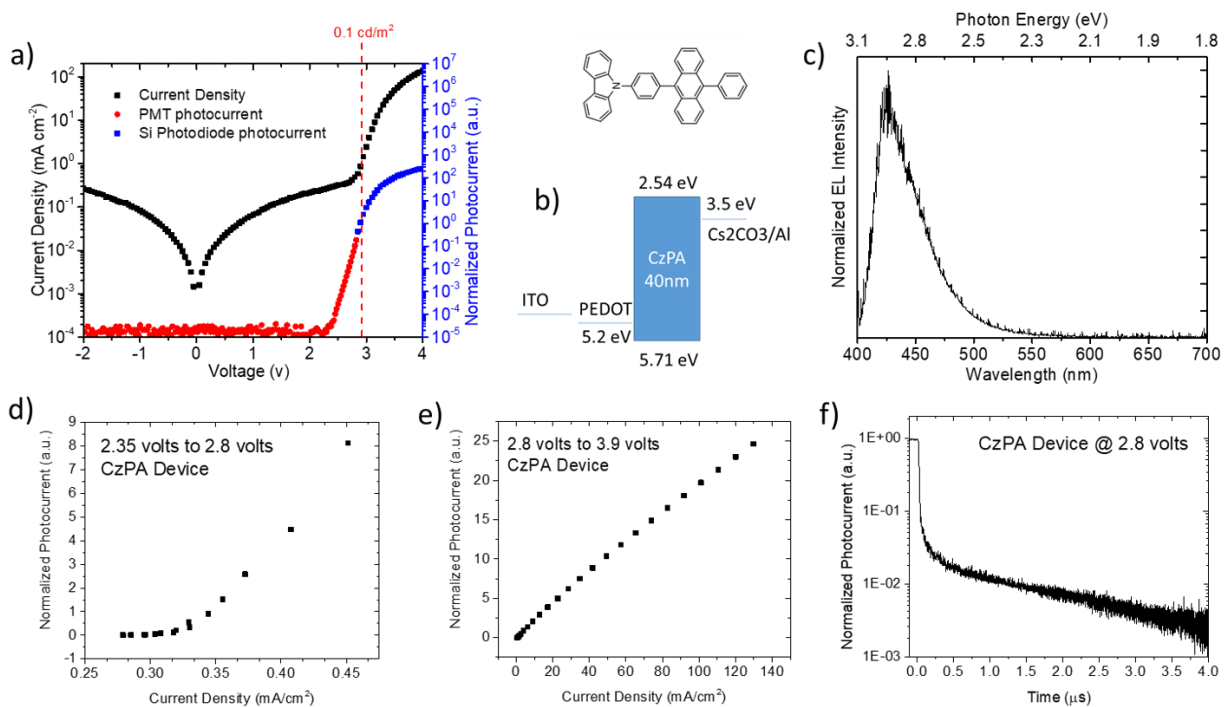


Figure 4.14. a) Device current density and photocurrent versus bias voltage. The photocurrent corresponding to a luminance of 0.1 cd/m^2 is also marked on the graph. b) Molecular structure of CzPA and the device structure of the OLED with a single-layer of CzPA. c) Electroluminescent (EL) spectra of the device at 2.8 volts. d) Photocurrent vs. current density in the low voltage region showing a quadratic behavior, which is indicative of emission due to triplet-fusion, “quadratic regime”. e) Photocurrent vs. current density in the high voltage region showing a normal linear behavior, “linear regime”. f) Transient EL dynamic of the device after turn-off shows microsecond scaled delayed fluorescence which is indicative of fluorescence due to triplet-fusion. A reverse bias of -5.0 volts was applied at the onset of turn-off.

As shown in Figure 4.12b and 4.14b, there are no other organic semiconductors in the CzPA and BCzVBi single-layer devices that can form a CT exciton, and yet we see electroluminescence at sub-bandgap voltages, we also observe evidence of fluorescence due to triplet-fusion in both devices. It appears that the voltage at the onset of electroluminescence for the single-layer devices corresponds to the added value of the Schottky barrier for hole injection, from PEDOT, and the first triplet excited states. Given the 5.2 eV HOMO energy of PEDOT, the Schottky barrier for hole injection for the CzPA and the BCzVBi single-layer devices are 0.51 eV and 0.18 eV respectively. Adding the triplet energy of the two materials, that is 1.77 eV for CzPA and 1.94 eV for BCzVBi to the Schottky barrier we get

energies of 2.28 eV and 2.12 eV which are very close to the experimental value of the voltage at onset of electroluminescent for the single-layer devices, i.e. 2.35 volts and 2.10 volts.

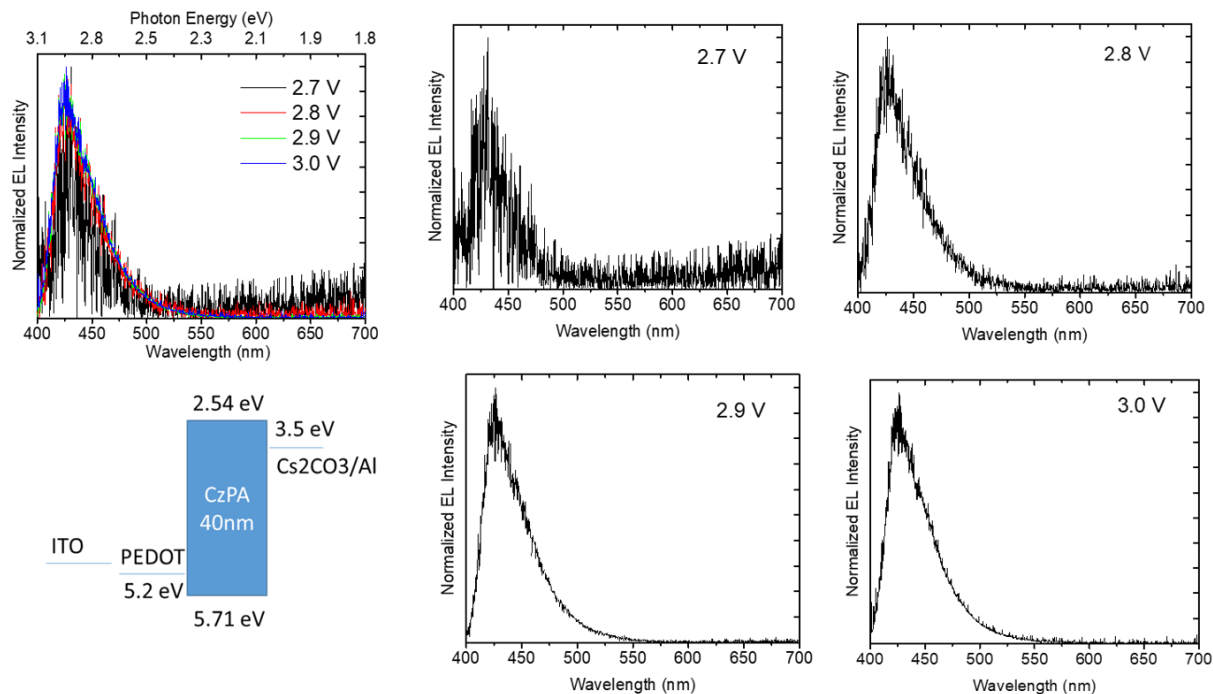


Figure 4.15. Device structure of the CzPA single-layer device and its EL spectra at different voltages.

4.3.8. Examining Other Wide-Bandgap Organic Semiconductors

I further made three other single-layer devices with three other organic molecules with large singlet-triplet splitting and triplet-fusion: BDAVBi (4,4'-Bis[4-(diphenylamino)styryl]biphenyl), DMPPP (1,1'-(2,5-Dimethyl-1,4-phenylene)dipyrene) and TBADN (2-tert-Butyl-9,10-di(naphth-2-yl)anthracene). All three devices showed electroluminescence at sub-bandgap voltages close to the added value of their triplet energy and the hole injection Schottky barrier, similar to BCzVBi and CzPA. The device structure and characteristics of the BDAVBi, DMPPP and TBADN single-layer devices are shown in Figure 4.16 and 4.17 and 4.18.

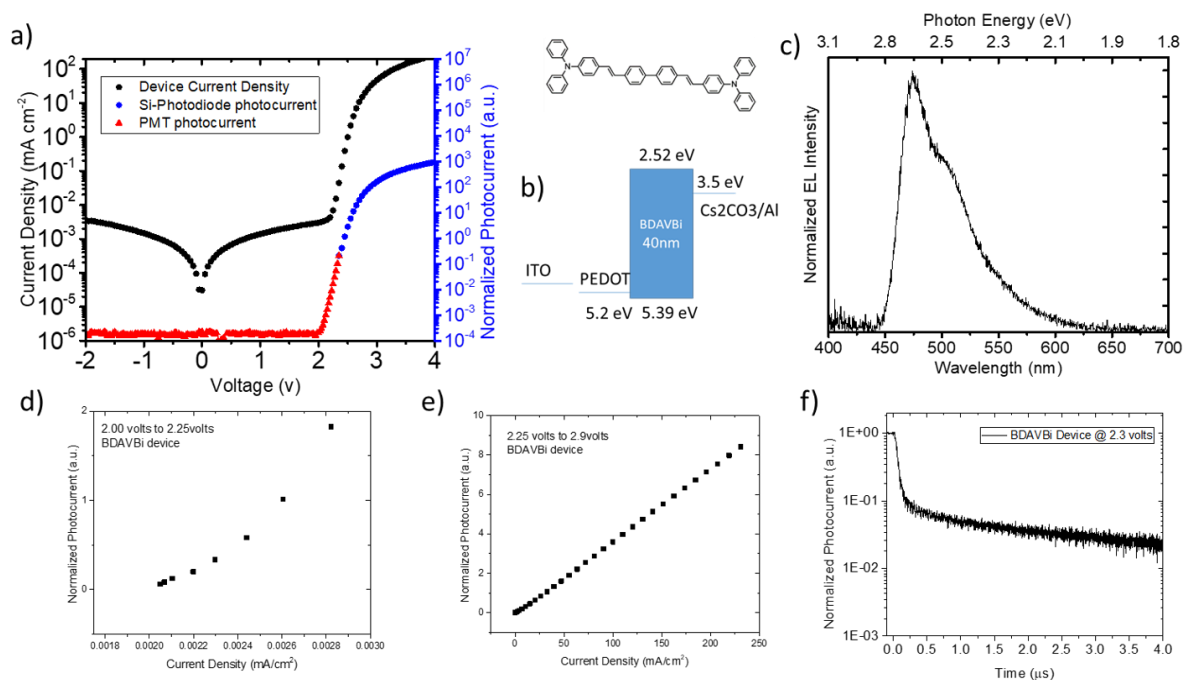


Figure 4.16. a) Device current density and photocurrent versus bias voltage. Two detectors were used to detect the electroluminescence; a photomultiplier tube (PMT) was used for low light intensities and a Si-photodiode was used for higher light intensities (due to PMT saturation). b) Molecular structure of BDAVBi and the device structure of the OLED with a single-layer of BDAVBi. c) Electroluminescent (EL) spectra of the device. d) Photocurrent vs. current density in the low voltage region showing a quadratic behavior, which is indicative of emission due to triplet-fusion, “quadratic regime”. e) Photocurrent vs. current density in the high voltage region also showing a quadratic behavior. f) Transient EL dynamic of the device after turn-off shows microsecond scaled delayed fluorescence which is indicative of fluorescence due to triplet-fusion. A reverse bias of -5.0 volts was applied at the onset of turn-off.

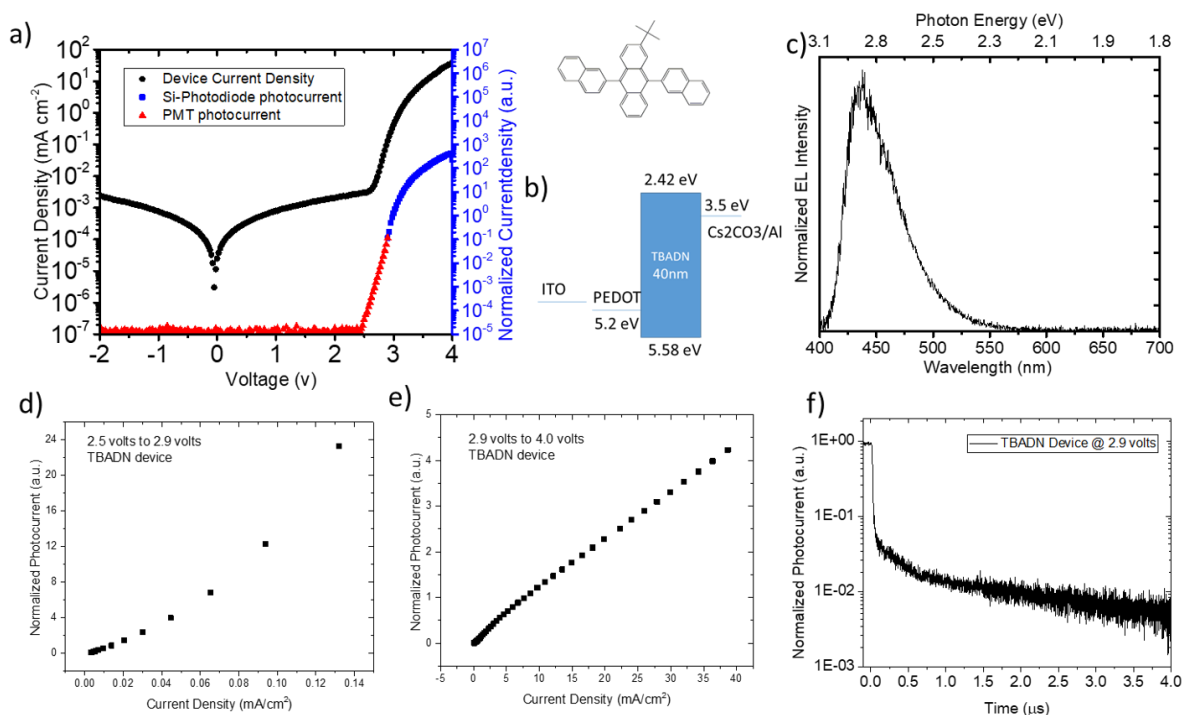


Figure 4.17. a) Device current density and photocurrent versus bias voltage. b) Molecular structure of TBADN and the device structure of the OLED with a single-layer of TBADN. c) Electroluminescent (EL) spectra of the device. d) Photocurrent vs. current density in the low voltage region showing a quadratic behavior, which is indicative of emission due to triplet-fusion, “quadratic regime”. e) Photocurrent vs. current density in the high voltage region also showing a quadratic behavior. f) Transient EL dynamic of the device after turn-off shows microsecond scaled delayed fluorescence which is indicative of fluorescence due to triplet-fusion. A reverse bias of -5.0 volts was applied at the onset of turn-off.

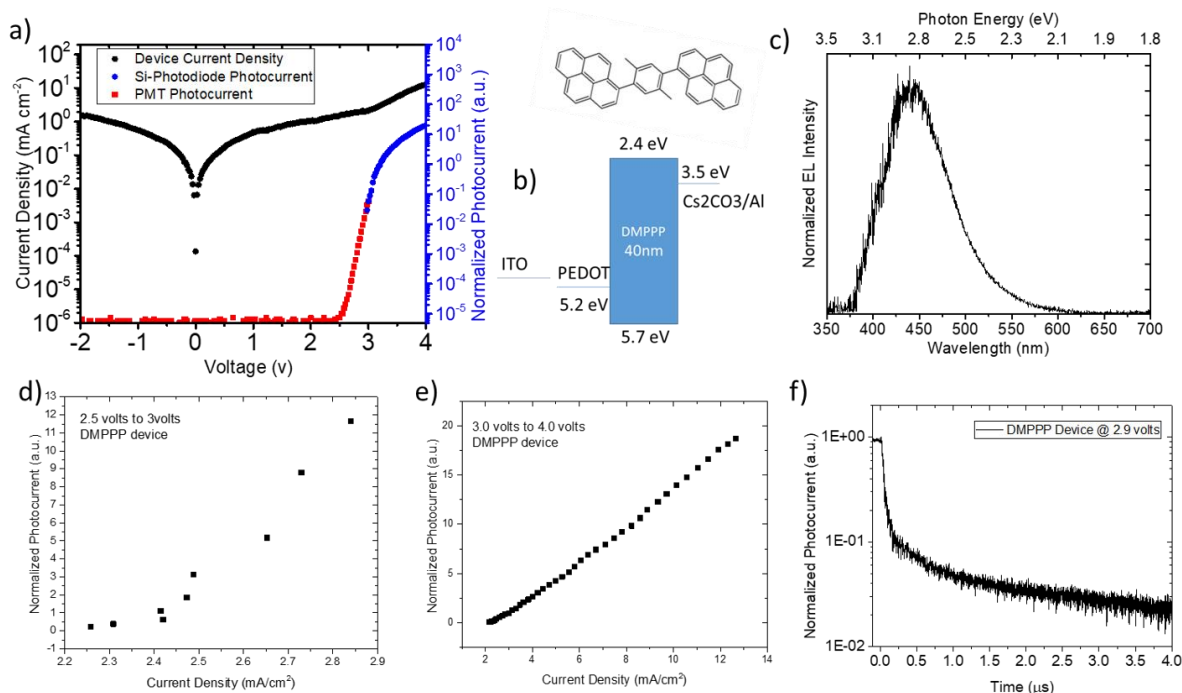


Figure 4.18. Device current density and photocurrent versus bias voltage. b) Molecular structure of DMPPP and the device structure of the OLED with a single-layer of DMPPP. c) Electroluminescent (EL) spectra of the device. d) Photocurrent vs. current density in the low voltage region showing a quadratic behavior, which is indicative of emission due to triplet-fusion, “quadratic regime”. e) Photocurrent vs. current density in the high voltage region also showing a quadratic behavior. f) Transient EL dynamic of the device after turn-off shows microsecond scaled delayed fluorescence which is indicative of fluorescence due to triplet-fusion. A reverse bias of -5.0 volts was applied at the onset of turn-off.

4.3.9. Examining Narrow-Bandgap Organic Semiconductors: Rubrene

Witnessing the overwhelming evidence that all the organic molecules I examined above show electroluminescence and triplet-fusion at sub-bandgap voltages, I decided to revisit rubrene and see if this phenomenon is only limited to wider bandgap organic semiconductors. Rubrene is the most well-known organic single molecule which shows p-type delayed fluorescence, or triplet-fusion, with 100% efficiency, i.e. all of the triplet-fusion will lead to radiative singlet excited states.[124] Kondakov assigned the high efficiency of the singlet-yielding triplet-fusion, to the energy favorability in rubrene. Since the first excited triplet state ($T_1=1.1\text{eV}$) is exactly half of the first singlet excited state ($S_1=2.2$

eV) and the higher order triplet excited state is larger than the first singlet state ($T_n \sim 3.6\text{eV}$).[124][127] Pandey et al. and Xiang et al. previously reported single-layer devices using rubrene, similar to the single-layer devices I reported here.[128][138] They reported turn-on voltages as low as ~ 1 volt, for the rubrene devices which used C60 as the electron transport layer, with the structure: ITO/PEDOT/rubrene/C60/cathode. However, they both reported turn-on voltages larger than 2.2 volts for the devices that lacked C60, with the structure ITO/PEDOT/rubrene/cathode. Xiang et al. attributed the electroluminescence at sub-bandgap voltages, for the case of the rubrene/C60 device, to the CT-exciton formed between the C60 and rubrene.

I made a single-layer device with the following structure: ITO / PEDOT (30nm) / Rubrene (40nm) / Aluminum (100), following the work reported by Xiang et al, as shown in Figure 4.19. I neither used C60 nor any other electron injection/transport material in my device, I deposited just bare aluminum on top of bare rubrene and characterized the device. Aluminum work function (4.08 eV from vacuum) and the triplet level of rubrene (4.10 eV from vacuum) align perfectly with each other. The device characteristics of the bare rubrene single-layer device is shown in Figure 4.19. Figure 4.19a shows clear diode turn-on of about 1 volt and onset of electroluminescence at about 1.1 volts. The electroluminescence at sub-bandgap voltages of a bare rubrene single-layer device at voltages close to its triplet energy, without the presence of any other semiconductors in the device that can form any CT-excitons, is conclusive evidence that materials that show delayed fluorescence due to triplet-fusion can be turned-on at voltages close to the triplet energy and directly form triplet excitons without providing the bandgap energy for injection into the HOMO-LUMO levels. This significant experimental finding challenges the fundamental understanding of organic semiconductors, where it is always assumed that there should be enough energy (voltage) for electron and hole to be injected into the HOMO-LUMO levels, before any triplet or singlet excitons can form. We should note here that the

device characteristics of my single-layer rubrene device contradicts the results reported by Xiang et al.

[128]

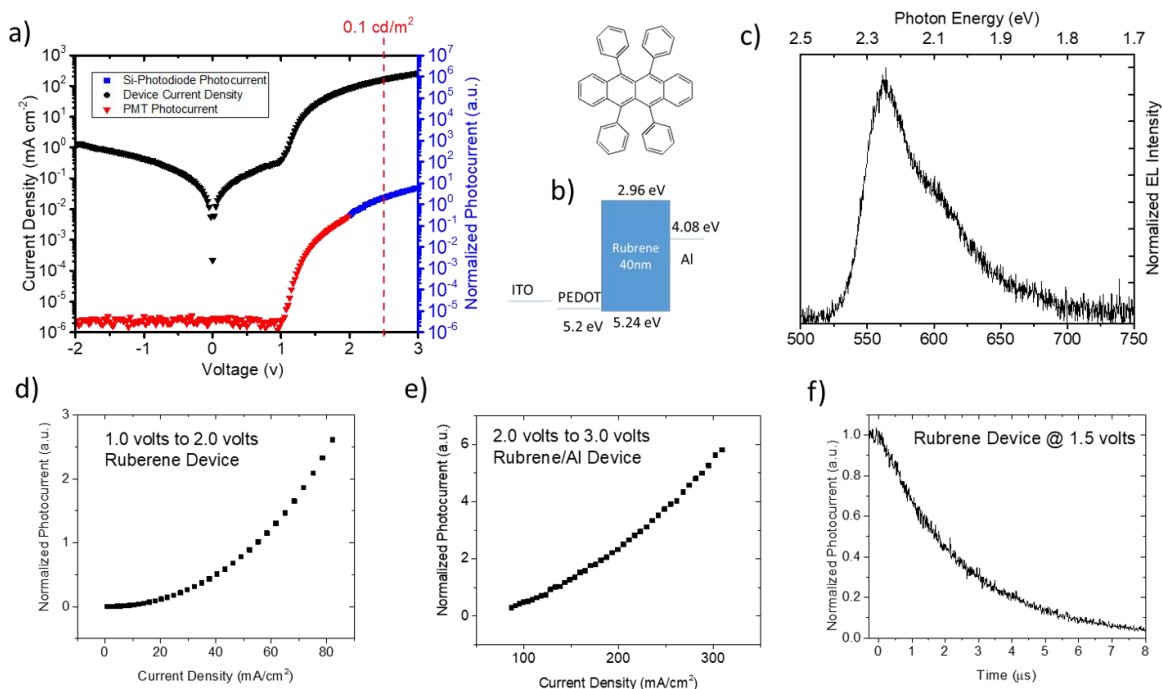


Figure 4.19. a) Device current density and photocurrent versus bias voltage. Two detectors were used to detect the electroluminescence; a photomultiplier tube (PMT) was used for low light intensities and a Si-photodiode was used for higher light intensities (due to PMT saturation). The photocurrent corresponding to a luminance of 0.1 cd/m^2 is also marked on the graph. b) Molecular structure of rubrene and the device structure of the OLED with a single-layer of rubrene. c) Electroluminescent (EL) spectra of the device. d) Photocurrent vs. current density in the low voltage region showing a quadratic behavior, which is indicative of emission due to triplet-fusion, “quadratic regime”. e) Photocurrent vs. current density in the high voltage region also showing a quadratic behavior. f) Transient EL dynamic of the device after turn-off shows microsecond scaled delayed fluorescence which is indicative of fluorescence due to triplet-fusion. A reverse bias of -5.0 volts was applied at the onset of turn-off.

Intriguingly, in the case of the rubrene single layer OLED adding a thin layer of Cs_2CO_3 or LiF increases both the operating voltage of the OLED, compared to the OLED with bare aluminum as cathode, Figure 4.20.

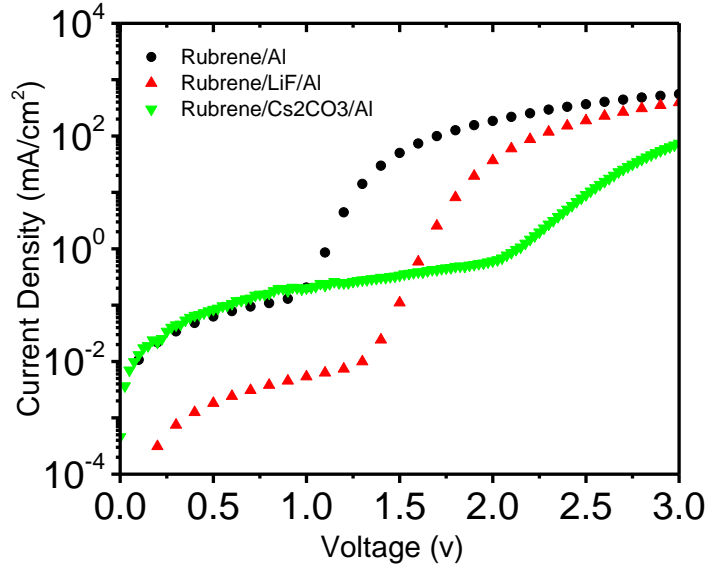


Figure 4.20. Current density as a function of voltage of rubrene single-layer OLEDs, when cathode is bare aluminum, LiF (1 nm) /Aluminum or Cs₂CO₃/Aluminum.

Shaheen et al observed a decrease in the “effective workfunction” of aluminum cathode in OLED devices, when a thin layer of LiF was added before aluminum deposition. [139] The change in work-function was reported to be dependent on the thickness of the LiF layer. It is plausible to expect a similar behavior from a thin layer of Cs₂CO₃. When a thin layer of Cs₂CO₃ or LiF is added, aluminum workfunction decreases and a better energy alignment with LUMO level of the emitter rather than the triplet level appears. This mis-alignment with the triplet level and better-alignment with the LUMO level can result into a competition between injection into the LUMO level and the triplet level. I should not here that the observed phenomena can also be explained in terms of exciplex formation between the cathode and the organic emitter. However in case of exciplex, an emission corresponding to the exciplex is expected. I did not observe any emission from a proposed exciplex states in none of the devices reported in this chapter.

4.3.10. Direct Formation of Triplet Excitons by Charge Injection

My results for all the organic molecules that I have characterized in OLED devices and reported here contradicts the HOMO-LUMO injection understanding of organic semiconductors for materials that show electroluminescence due to triplet-fusion. I believe that once holes are injected into the HOMO level of the organic molecule with TF property, the electrons directly form triplet excitons on the molecules without injection to the LUMO level and result in electroluminescence due to triplet-fusion. Therefore, for the single-layer devices, the onset of electroluminescence would be at the voltages that can provide enough energy for the holes to overcome the hole injection Schottky barrier (ϕ_h) from PEDOT's HOMO into the HOMO of the TF molecule, and enough energy for the electrons to excite the first triplet excited state (T_1) of the molecule, i.e. $V_{on} \sim \phi_h + T_1$, as shown in Figure 4.21a. Table 4.1 shows a list of molecules studied in this work in single-layer devices which show electroluminescence at sub-bandgap voltages due to TF, with the structure: ITO / PEDOT (30nm) / molecule studied (40nm) / Cs₂CO₃ (1nm) / Al (100nm). No Cs₂CO₃ was used for the rubrene single-layer device, similar to the device reported by Xiang et al.[128]

4.3.11. Exciton Formation and Energy Transfer in the Multilayer Device

Looking back at the optimized device, despite having luminance of 0.1 cd/m² at 2.4 volts, the device current density suggests a turn-on voltage much lower than 2.4 volts, Figure 4.4b. The 0.1 cd/m² luminance is the detection limit of the Si-photodetector. When I measured electroluminescence of the optimized multilayer device using the PMT, Figure 4.22, I could detect electroluminescence at voltages as low as 2.1 volts, similar to the BCzVBi single-layer device. The onset of electroluminescence at the same voltage of 2.1 volts, for both the single-layer BCzVBi device and the high-efficiency optimized device, suggests that the initial triplet exciton formation occurs on BCzVBi molecules and that BCzVBi is responsible for electroluminescence at initial sub-bandgap voltages, as shown in Figure 4.21b. After the triplet excitons are formed on BCzVBi molecules, three scenarios can occur which

would ultimately lead to the creation of singlet excitons on BCzVBi, as shown in Figure 4.21c. First, BCzVBi triplet excitons can annihilate (TF) with each other and create radiative singlet excitons on BCzVBi molecules, much like the case in BCzVBi single-layer device. Second, BCzVBi triplet excitons can transfer their energies to CzPA triplet excitons via Dexter energy transfer (ET). The CzPA triplet excitons can then annihilate (TF) and create a singlet exciton on CzPA molecules. The singlet excitons on the CzPA molecules would then transfer their energy by Forster energy transfer (ET) to the singlet excitons on BCzVBi, due to the overlap between CzPA's emission and BCzVBi's absorption. Third, CzPA and BCzVBi triplet excitons can hetero-annihilate and ultimately lead to formation of singlet excitons on BCzVBi. The formation of triplet excitons without direct injection of the electrons into the LUMO level of the TF molecules and having both the emitter and the host showing fluorescence due to TF, explains the electroluminescence at sub-bandgap voltages of my state-of-the-art blue fluorescent device which I initially reported and its high luminance at such low voltages.

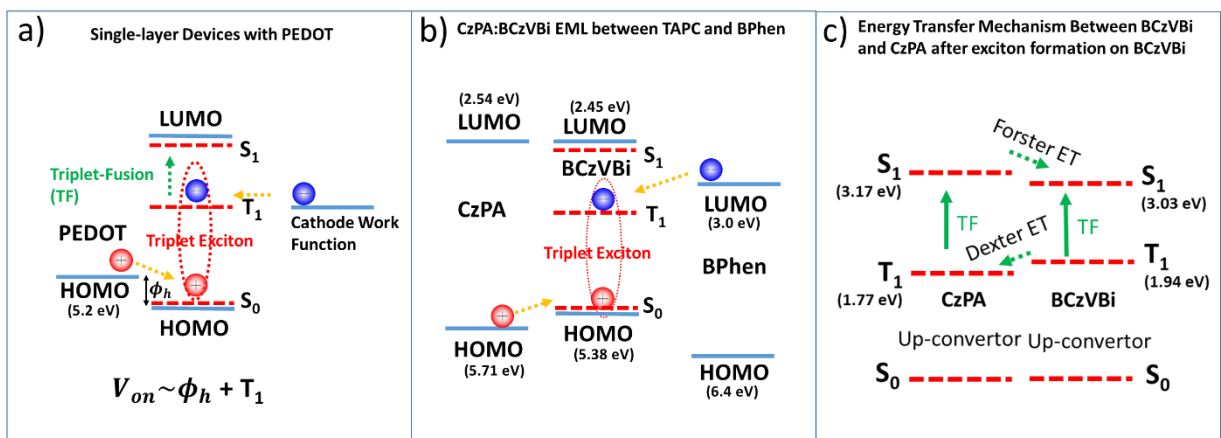


Figure 4.21. a) Direct triplet exciton formation in single-layer devices with the structure ITO/PEDOT/Emitter/Cathode. Once holes are injected into the HOMO of the emitter, triplet excitons would form directly without injection of the electrons to the LUMO level. Therefore, the onset of electroluminescence would be the required energy for the triplet exciton plus the Schottky barrier for the hole injection into the HOMO of the emitter. b) Direct triplet exciton formation on BCzVBi molecule, in CzPA:BCzVBi EML placed between TAPC and BPhen as HTL and ETL respectively. Once holes are injected into the HOMO of CzPA they will transfer to the HOMO of the BCzVBi and then the electrons directly form triplet excitons without injection to the LUMO of BCzVBi. c) Energy transfer mechanism and interaction between CzPA and BCzVBi. At sub-bandgap voltages. Triplet excitons are initially formed on Figure 4.21. (continued) BCzVBi molecules, they can then, either directly undergo fusion and create a radiative singlet exciton on BCzVBi or they can diffuse to the triplet state of CzPA via Dexter energy transfer (ET). The triplet excitons on CzPA then undergo fusion and create a radiative singlet exciton on CzPA, which will transfer its energy to the singlet state of BCzVBi via Forster energy transfer (ET), due to the overlap between CzPA's emission and BCzVBi's absorption. The triplet excitons on BCzVBi and CzPA can also have hetero-fusion which would further enhance emission due to triplet fusion.

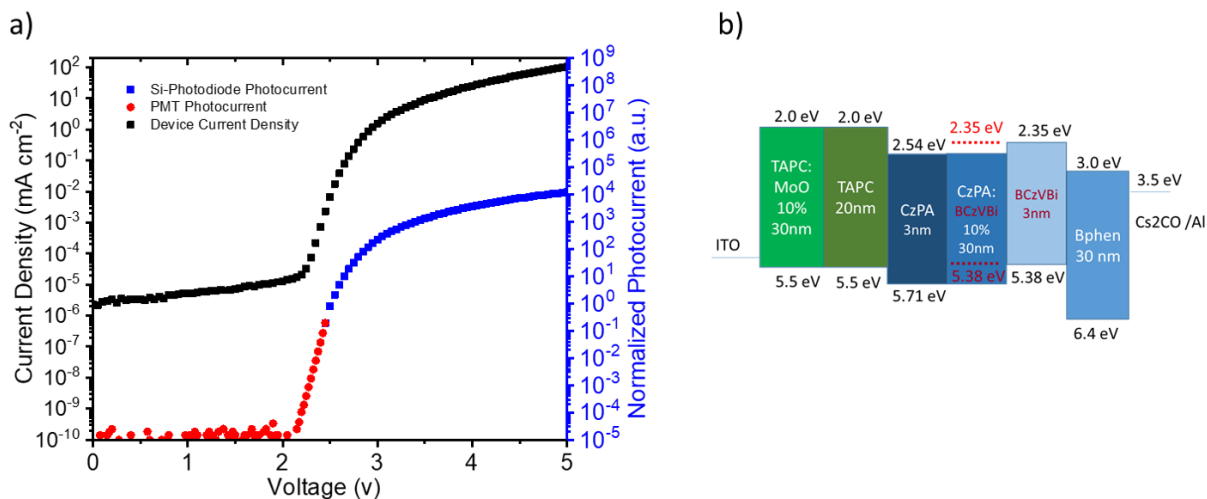


Figure 4.22.a) Voltage-Current Density-Photocurrent of the optimized device, using Si-Photo diode and PMT. The onset of the electroluminescence occurs at 2.1 volts, similar to the BCzVBi single-layer device, indicating that triplet excitons first form on BCzVBi at sub-bandgap voltages. b) Device structure of the optimized device.

Table 4.1. Materials studied in single-layer OLEDs. The OLED structure for all the devices is ITO/PEDOT (30 nm) / Material (40 nm) / Cs₂CO₃ (1 nm) / Aluminum (100 nm), except for rubrene. Rubrene device structure was ITO / PEDOT (30 nm) / Rubrene (40 nm) / Aluminum (100 nm).

Material	First Triplet Excited State ¹ (T ₁) (eV)	HOMO Level from Vacuum ² (eV)	Hole Injection Barrier from PEDOT (eV)	T ₁ + Hole Injection Barrier (eV)	Voltage at EL Onset (V)	HOMO- LUMO gap ³ (eV)
BCzVBi	1.94	5.38	0.18	2.12	2.10	3.03
CzPA	1.77	5.71	0.51	2.28	2.35	3.17
DMPPP	2.06	5.70	0.50	2.56	2.50	3.30
TBADN	1.82	5.58	0.38	2.20	2.50	3.16
BDAVBi	1.86	5.39	0.19	2.05	2.00 V	2.86
Rubrene	1.14	5.24	0.04	1.18	1.10 V	2.28

¹ Triplet state energies of the materials are measured using phosphorescence, as shown in the supporting information. ² HOMO levels are measured using cyclic voltammetry as explained in the experimental section. ³ HOMO-LUMO gap (bandgap) is measured from solution-phase absorption and emission spectra, as shown in the supporting information.

To investigate more the effect of hole-injection Schottky barrier on the voltage at onset of electroluminescence, single-layer devices using BCzVBi were made with different HTL layers, with the structure, ITO / PEDOT (30nm) / HTL (20 nm) / BCzVBi (40 nm) /Cs₂CO₃ (1 nm) / Al (100nm). For HTL, three different materials were used: CzPA, TAPC and TcTa, (Tris(4-carbazoyl-9-ylphenyl)amine). The results are shown in table 4.2.

4.3.12. A Perturbation Approach to Singlet-Triplet State Mixing

Based on my purposed mechanism of direct triplet exciton formation by charge injection, when positive polarons are present in the organic molecules, electrons are readily injected into the triplet level and form triplet excitons without injection into the HOMO level. The electric potential due to a positive polaron, has perturbative effect on the quantum states of the molecule, which leads to intermixing of pure states. Under perturbation, photoexcitation from the ground state of the molecule to the triplet excited state is allowed, since both singlet and triplet states become a linear combination of each other, as further explained below.

Treating an exciton as a two-fermionic quantum-system with half spins, when the ground state has a singlet spin-state, $|S_0\rangle$, (where $|S_0\rangle$ denotes the total eigenstate of the ground state, i.e. multiplication of special-eigenstate and spin-eigenstate) and the excited states have either singlet or triplet spin-eigenstates, i.e. $|S_n\rangle$ and $|T_n\rangle$, then only transition to excited states with a singlet spin-eigenstate is allowed, and the transition of excited states with a triplet spin-eigenstate is forbidden, i.e.:

$$\langle T_n | H | S_0 \rangle = 0, \quad (1-4)$$

However, when the positive polarons with potential V are introduced to the system, the new perturbed Hamiltonian becomes $H' = H + V$, and the new eigenstates of the system will become a linear combination of unperturbed, “pure” eigenstates. According to the first order perturbation theory, the new “perturbed” eigenstates, $|S'_n\rangle$ and $|T'_n\rangle$, can be calculated using the equations below:

$$|S'_n\rangle = \sum_{i \neq n} \frac{\langle S_i | V | S_n \rangle}{S_n - S_i} |S_i\rangle + \sum_{j \neq n} \frac{\langle T_j | V | S_n \rangle}{T_n - S_j} |T_j\rangle, \quad (2-4)$$

$$|T'_n\rangle = \sum_{i \neq n} \frac{\langle S_i | V | T_n \rangle}{S_n - T_i} |S_i\rangle + \sum_{j \neq n} \frac{\langle T_j | V | T_n \rangle}{T_n - T_j} |T_j\rangle, \quad (3-4)$$

Here, T_n (S_n) denotes the energy eigenvalue of the eigenstate of an excited state with a triplet (singlet) spin-eigenstate, under the hamiltonian operator in an unperturbed system, i.e.

$$H|T_n\rangle = T_n|T_n\rangle, \quad (4-4)$$

$$H|S_n\rangle = S_n|S_n\rangle, \quad (5-4)$$

As we see from equation 2-4 and 3-4, with the presence of a perturbative potential (from hole polarons), the triplet and singlet excited states have no longer a “pure” triplet or singlet spin-eigenstate and triplet and singlet excited states are “mixed” with each other. In the perturbed system, a transition from the ground state to all excited states is allowed, i.e.:

$$\langle T'_n|H'|S'_0\rangle \neq 0, \quad (6-4)$$

Therefore, we should be able to see the spectral absorption of the first excited triplet state when positive polarons are present in the film. Figure 4.23 a (b) shows the spectral absorption of the Device A (B) with the structure of: ITO/MoO_x/BCzVBi/Al (ITO/Bphen/BCzVBi/LiF/Al) at different bias voltages. MoO_x layer in Device A, creates an ohmic contact for hole injection into the BCzVBi layer, while BPhen layer in Device B creates a Schottky barrier for hole injection into the BCzVBi layer. There is a strong increase in absorption coefficient in Device A, around 2.0 eV which is the same as the triplet energy of BCzVBi, indicating that photoexcitation of the triplet states becomes accessible once hole polarons are present in the BCzVBi layer. We note that photoexcitation of triplet state of BCzVBi also happens at a reverse bias of -2 volts. In the next paragraph, I will argue that hole polarons in BCzVBi layer are present even at reverse biases. Device B, in figure 4.23 shows no significant change in the absorption coefficient for across the spectrum, indicating a lack of excitation for the triplet state of BCzVBi.

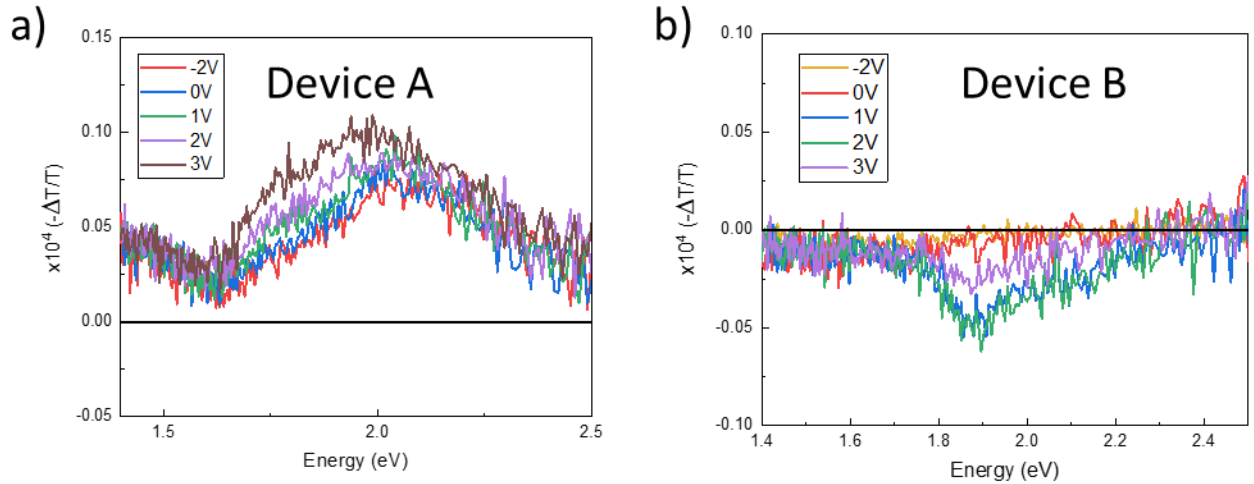


Figure 4.23. Spectral change in absorption coefficient as a function of applied bias for a) Device A with structure ITO/MoO_x/BCzVBi/Al and b) Device B with structure ITO/BPhen/BCzVBi/LiF/Al.

As shown in Figure 4.23 a, Device A showed absorption around the triplet energy of BCzVBi, even at reverse biases. This is not surprising, since Berleb et al. have previously shown that a negative interfacial charge concentration can remain in an NPB/Alq₃ bilayer device even when reverse biases are applied.[140] The interfacial charge can only be removed when the reverse bias is increased beyond a “transition voltage”.

Later Kondakov, measured lifetime of triplet excitons decays in TF OLEDs using transient EL (TrEL) measurements, with different reverse-biases applied immediately after device turn-off. Kondakov, too, observed that the triplet life time, dramatically increases when the reverse bias at the turn-off state of the devices is increased beyond a “transition voltage”.[136] He argued that the presence of negative polarons (from the interfacial charge) leads to triplet-polaron-annihilation, which shortens the triplet lifetime, and when the reverse bias at the onset of device turn-off is increased beyond the “transition voltage”, the negative interfacial charge is removed leading to an increase in triplet exciton lifetime.

It is interesting to note that increasing the forward bias voltage, increases the intensity in absorption. As I showed in equations 3-4 and 4-4, the numerator of the ket coefficients indicates that, the intensity of state mixing is directly proportional to the intensity of the perturbing potential V , i.e. more negative charges result in an stronger spin mixing. It should also be noted that the denominator of ket coefficients in equations 3-4 and 4-4 indicates that the states energies close to each other will have be “mixed” in an stronger manner, for instance $|T_1\rangle$ mixture with $|S_0\rangle$ is much stronger than its mixture with $|S_5\rangle$.

4.3.13. TF vs. non-TF Host

For the sake of comparison, a device was made with the exact structure as the optimized multilayer device in section 4.2, with the only difference of using CBP (4,4'-Bis (carbazol-9-yl) biphenyl) as the host instead of CzPA, as shown in Figure 4.24. CBP is a conventional host material with a high triplet energy of 2.6 eV, that is known to not show any delayed fluorescence nor triplet-fusion.[141][142] In the CBP device, at low voltages only the emitter can have TF which is quite ineffective due to low concentration of the emitter compared to the host. Figure 4.24 shows the device structure and performance of the CBP device vs. the optimized CzPA device. The device using CBP as host has a much larger operating voltage at similar luminances compared to the optimized CzPA device, resulting in four times less power efficiency.

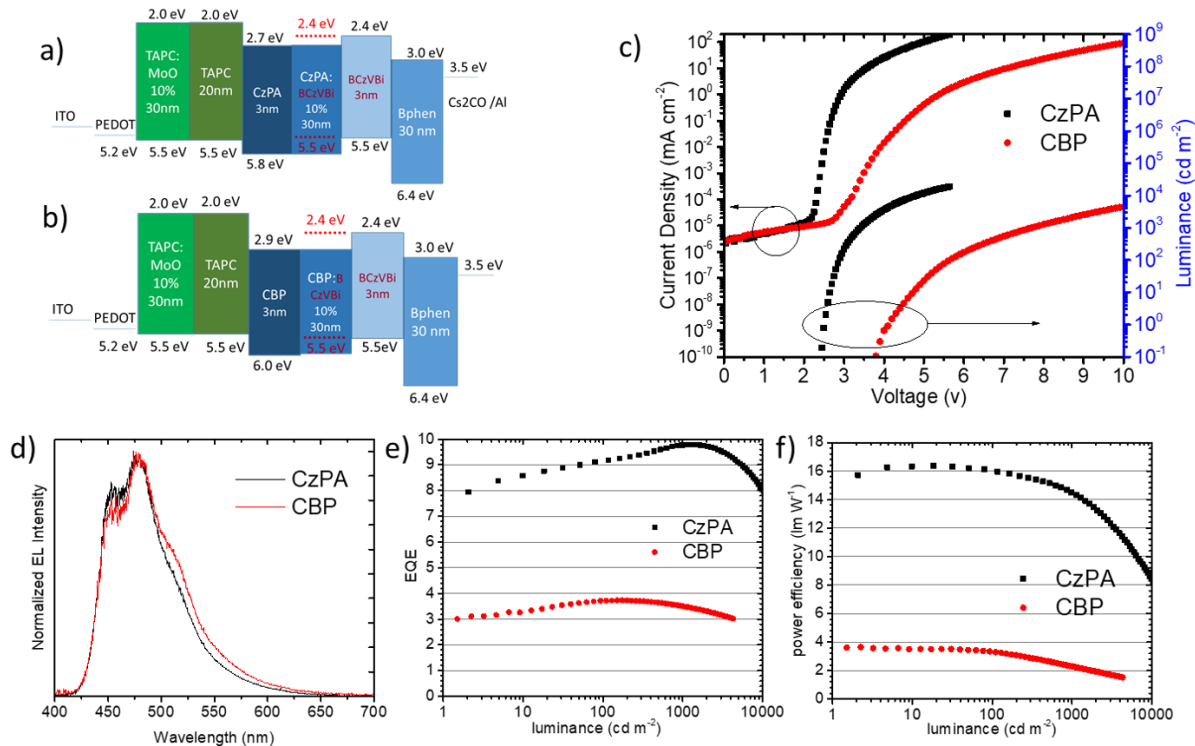


Figure 4.24. Comparison between the device using CBP as host vs the optimized device using CzPA as host. a) and b) Device structures. c) JVL characteristic of the devices, while the device using CzPA as host has a turn-on voltage of 2.4 volts, the device using CBP has a turn-on voltage of 3.8 volts. d) and e) and f) EL spectra, EQE and power efficiency of the devices.

4.3.14. This Work's Hyper-Fluorescent OLED vs. Literature's Best Phosphorescent and TADF OLEDs

In table 4.2, I have compared the performance of my optimized device with some of the best phosphorescent and TADF OLEDs with similar color coordinates. Although TADF and phosphorescent OLEDs can achieve very high values of EQE and power efficiency (PE) at very low luminance, at higher practical luminance ranges (>500 cd/m²) my optimized fluorescent device has the highest power efficiency compared to all other TADF and phosphorescent devices with similar color coordinates, owing to its sub-bandgap and low operating voltages.

Table 4.2. Comparing performance of my optimized device with some of the best TADF and phosphorescent OLEDs with similar color coordinates reported in literature. my device has the highest power efficiency at a luminance of 500 cd/m² and larger, compared to all other devices shown in the table. N/R stands for not-reported.

Emitter	V @ 1 cd/m ² (volts)	V @ 500 cd/m ² (volts)	V @ 1000 cd/m ² (volts)	Max PE (lm/W)	PE @ 500 cd/m ² (lm/W)	PE @ 1000 cd/m ² (lm/W)	Max EQE (%)	EQE @500 cd/m ² (%)	EQE @ 1000 cd/m ² (%)	CIE (x,y)	Ref.
BCzVBi	2.50	3.2	3.4	16.4	15.1	14.5	9.8	9.6	9.8	(0.15,0.21)	This Work
DTPDDA	3.0	5.0	5.8	30.4	10	9.8	22.3	11	10.6	(0.15,0.20)	Ref.[143]
34TCzTTrz	3.8	7.0	9.8	15.0	N/R	N/R	10.3	<5	<1	(0.16,0.20)	Ref.[144]
CzAcSF: TBPe	3.0	5.0	5.0	23.4	N/R	9.7	15.4	N/R	10.7	(0.15,0.23)	Ref.[145]
DDCzTrz	4.0	5.9	8.0	23.6	4.0	N/R	18.4	5.0	N/R	(0.16,0.21)	Ref.[146]
FCNIrpic	4.0	6.0	8.0	29.8	11.9	10.2	18.9	17.7	16.7	(0.14,0.21)	Ref.[147]
Ir(dbfmi)	2.56	N/R	4.74	35.9	10	6.3	18.6	N/R	6.2	(0.15,0.19)	Ref.[148]

4.4. Conclusion

In conclusion, in this chapter I have presented overwhelming evidence, for the first time, that organic molecules with the TF property can have electroluminescence at voltages as low as half of their bandgap, by direct triplet exciton formation, without providing the voltage corresponding to the HOMO-LUMO bandgap. My discovery, ushers in a new generation of fluorescent OLEDs with high efficiency and ultra-low operating voltages. I have presented a state-of-the-art hyper-fluorescent organic light emitting diode with ultra-low operating voltages which results in a performance comparable to the best TADF and phosphorescent blue OLEDs. Table 2 compares the performance of my best device with some of the best TADF and phosphorescent OLEDs reported in literature with similar color coordinates. The ultra-low sub-bandgap operating voltage of my hyper-fluorescent

OLED, results in a staggering power efficiency. This discovery, ushers in a new generation of fluorescent OLEDs with high efficiency and ultra-low operating voltages. Fluorescent OLEDs with efficiencies beyond fluorescence limit of the 25% internal quantum efficiency (IQE) have been called as “Hyper-Fluorescent”.[149][150][151] I name the new generation of OLED devices **Su-per** fluorescent OLEDs, after the combination of the **Sub**-bandgap and **Hyper**-Fluorescence.

4.6. Experimental

TAPC, BPhen, BCzVBi, DMPPP, BDAVBi and Rubrene were purchased from Lumtec Technology Corp. CzPA was purchased from Chang Chun Tuo Cai Technology Co., Ltd. ITO thickness for all the substrates used was 50nm thick. For ellipsometry measurements a Woollam M2000 ellipsometer was used, and the data was fitted using WVASE software. Fabrication and evaporation of all layers was carried out under vacuum pressure of below 2×10^{-6} torr. The evaporation rate was between 1 and 2 Å/s. Electroluminescent spectrum was collected using an OceanOptics spectrometer, and calibrated using an standard lamp. A Photo Multiplier Tube (PMT), Hamamatsu R6358, was used to detect low-intensity electroluminescence and transient electroluminescence. An Si-photodiode, OSI Optoelectronics PIN UV-100, was used to detect high intensity electroluminescence. A semi-hemispherical lens was placed on the substrate to extract substrate-trapped light for all JV-Photocurrent measurements. An Agilent function generator, 3320A, was used for transient EL (TrEL) measurements. A 100 micro-second long pulse following a reverse bias of 5 volts was applied to devices for the TrEL measurements. Two 50.00 ohms resistors were used with the PMT and the OLED devices, as shunt resistors, to minimize RC response in TrEL measurements.

Molecular HOMO energy levels of interest were estimated from redox potentials measured by cyclic voltammetry (CV) using a CH Instruments CHI650E Electrochemical

Analyzer/Workstation. Measurements were carried out in a single electrochemical cell with a typical three-electrode configuration contained within an inert atmosphere glovebox (MBraun). The cell configuration consisted of a platinum disk working electrode, platinum wire counter electrode, and a Ag/AgNO₃ reference electrode. Analyte solutions were prepared in degassed dry dichloromethane containing 0.1 M tetrabutylammonium hexafluorophosphate (TBAPF₆, recrystallized from ethanol) as the supporting electrolyte and analyzed at a scan rate of 0.100 V s⁻¹. As an internal standard, ferrocene exhibited a reproducible oxidation potential of 0.01 V in the same cell and solvent.

Molecular triplet energies were experimentally estimated via phosphorescence spectra recorded at 77 K, Figure 4.25. The material of interest was dissolved in a glass-forming, heavy-atom containing solvent of 40 wt.% toluene, 40 wt.% dichloromethane, and 20 wt.% iodobenzene. The solution was cooled to 77 K in a transparent liquid-nitrogen Dewar. Time-gated phosphorescence spectra of the molecules were collected with an LP920 laser flash photolysis system (Edinburgh Instruments) using a wavelength-tunable Vibrant 355 LD-UVM Nd:YAG/OPO system (OPOTEK) as the excitation source (1.0-2.6 mJ/pulse). Emission spectra were collected with an iStar ICCD camera (Andor Technology), which was controlled by the LP900 software program (Edinburgh Instruments). The gate delay after excitation into the wavelength of each molecule's respective absorbance maximum was 200 μs, and the gate width for data collection was 200 μs. Time-gated phosphorescence spectra reported herein are the average of at least 512 laser flashes.

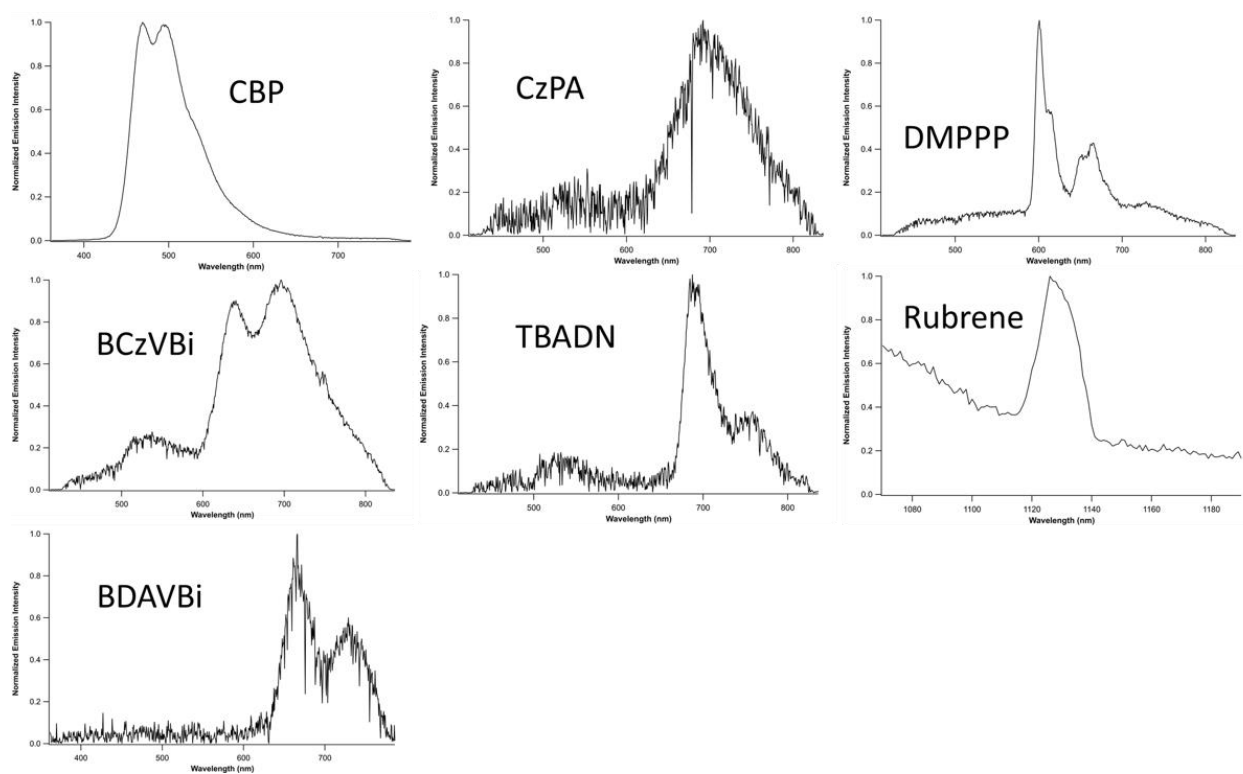


Figure 4.25. Phosphorescent spectra of the molecules studied in this work recorded at 77K. Molecular triplet energies were experimentally estimated via the phosphorescence spectra.

Molecular singlet energies were estimated from solution-phase absorption and emission spectra, Figure 4.26. Absorption spectra were acquired using an Agilent 8453 diode array spectrophotometer. Room temperature and 77 K static emission spectra were collected with a FLS980 fluorometer (Edinburgh Instruments) equipped with a 450 W Xe arc lamp and a Peltier cooled PMT (R928P Hamamatsu). The 77 K emission spectra were collected using a 2-MeTHF

optical glass cooled in the same manner detailed above. All static emission spectra were corrected for detector response.

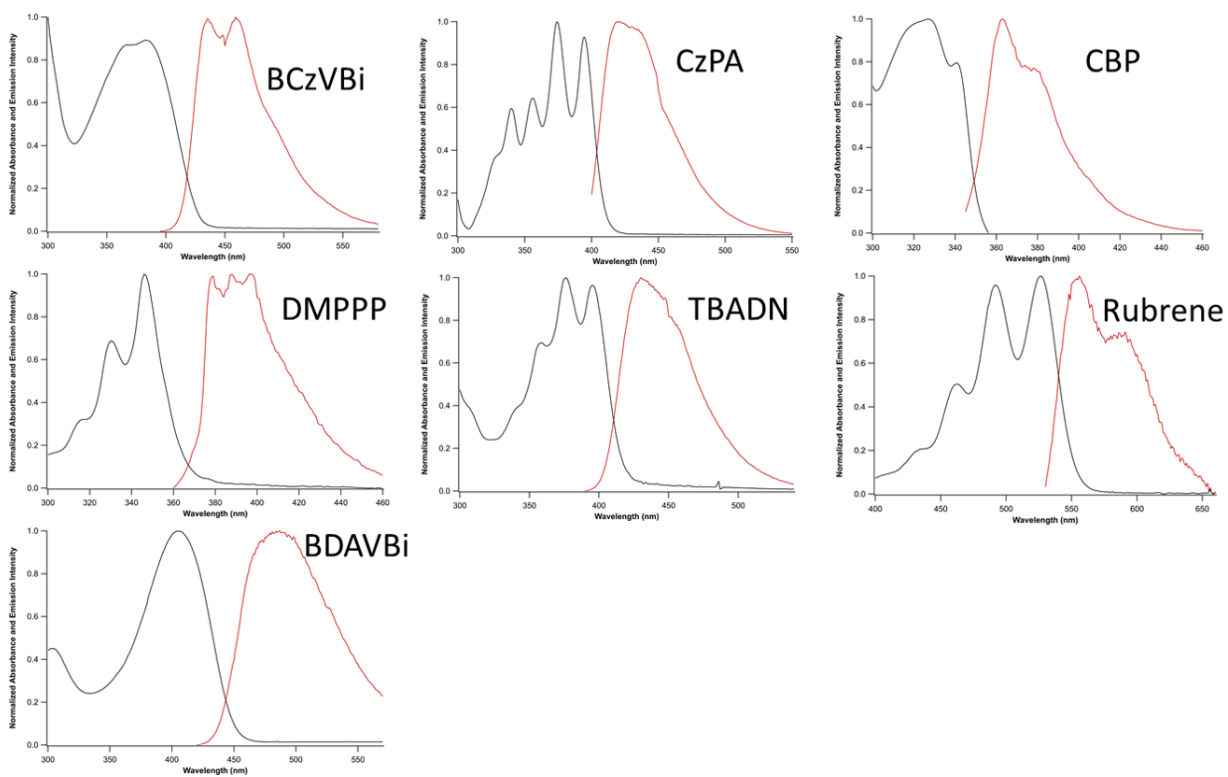


Figure 4.26. Photoluminescence (red) and absorption (black) spectra of the molecules used in this study. Molecular singlet energies were estimated from the absorption and emission spectra.

CHAPTER 5

CHAPTER 5: Future Work and Outlook

5.1. Electro-Optical Correlations in Organic Solids

In chapters two and three, I showed that low refractive index layers are crucial in increasing optical-outcoupling of organic light emitting diodes, when utilized at the position of the electron transporting layer, hole transporting layer and the transparent anode.

Apart from optical criteria to achieve an efficient OLED, in chapter one, it was argued that an optimal charge transport balance is required to have an efficient OLED. However, the correlation between charge transport mobility and the optical constants, of organic solids is not well understood. Yokoyama argued that the a larger in-plane birefringence leads to a larger vertical charge mobility due to a large π π orbital overlap because of a better molecular stacking order. He also showed that the structural disorder and electronic disorder are smaller for films with larger anisotropies. [101] However his study was only limited to a single family of electron transporting materials. A more comprehensive study, of correlation of optical anisotropy and both electron and hole transporting materials is recommended.

5.2. Degradation-Optical Correlations in Organic Solids

There seems to be an understating in the OLED community, especially by Adachi and others,[152] that low refractive index organic solids have a shorter operational lifetime and degrade faster compared with high index organic solids. Although they try to prove their argument through very small changes in the density of α NPD films deposited at different temperatures by ellipsometry measurements, the correlation between film density and material stability is still an open argument and requires a much more rigorous research.

5.3. Exploiting Optical Anisotropy

As I illustrated in chapter three, negative birefringent thin films can achieve similar increased optical out-coupling results when the layer, such as the electron transporting layer, is mainly responsible for a TM-polarized loss mode, such as SPP and TMWG mode. Also positive birefringent thin films can result in increased light out-coupling efficiency when they are located at positions where TE-polarized modes are largely distributed, for instance using PEDOT at the position of ITO (instead of ITO).

If Adachi's argument on the direct correlation of material stability and low-refractive is indeed accurate, then to achieve both stability and better optical outcoupling we can use birefringent layers. As I mentioned before, Yokoyama has already shown that birefringent materials have less disorder. It is worth mentioning that there are reports of very efficient OLEDs in literature by using PEDOT:PSS as anode and B3PYMPM as ETL, without realizing that the former is positively and the latter is negatively birefringent.[97]

5.4. Pushing the Efficiency Limit of Triplet-Fusion OLEDs

5.4.1 Quantification of Triplet-Fusion Contribution

In fluorescent OLEDs, the internal quantum efficiency is limited to only 25% due to non-radiative triplets. The archaic optical understanding of OLEDs predicts an optical-outcoupling of 20%. Based on this understanding the external efficiency of fluorescent OLEDs was thought to only be about 5% for a long time.

If we could harvest all the triplet excitons using triplet-fusion, then the internal quantum efficiency could increase up to $25\% + \frac{75\%}{2} = 62.5\%$. Now, based on the archaic understanding of light outcoupling, an external efficiency of a triplet-fusion OLED that harvests all the triplet

excitons is 12.5%. When Kondakov and others first reported a triplet-fusion OLED with 12.5% efficiency, they claimed that they have achieved 100% efficiency in triplet fusion and they have achieved the maximum internal quantum efficiency of 62.5% .[124] However today we know that the optical outcoupling in a conventional OLEDs with random orientation of the transition dipole moments is beyond 20% and it could be more than 40% for horizontally oriented dipoles. [153] This means that it is highly likely that the internal efficiency of the OLED reported by Kondakov and others is not 62.5% and the optical outcoupling is mis-accounted for. Unfortunately, up to this date there doesn't seem to be any robust method of quantization of triplet-fusion efficiency. A more fundamental study in this matter is recommended.

5.4.2 The Efficiency Limit of Triplet-Fusion OLEDs

Using emitters with preferred horizontal orientation, the potential to achieve external efficiencies as high as 25% is within reach and remains as a future challenge. Given the fact that the phosphorescent and TADF emitters are inherently unstable in blue due to high triplet energies, the future of blue OLEDs is without question in triplet-fusion.

5.4.3 Developing New Materials for Triplet-Fusion OLEDs

To develop new host materials for TF OLEDs, materials with larger photoluminescence quantum efficiency should be developed that with their first excited triplet energies exactly half of their first excited singlet energy and their higher triplet energies much larger than their first excited singlet energy. So that the conversion from triplet-fusion into the first singlet is energetically favorable. Up to this date such material for blue emission has not yet been invented and remains a future challenge.

REFERENCES

- [1] M. Schwoerer and H. C. Wolf, *Organic Molecular Solids*. 2008.
- [2] S. Ho, Y. Chen, S. Liu, C. Peng, D. Zhao, and F. So, “Interface Effect on Efficiency Loss in Organic Light Emitting Diodes with Solution Processed Emitting Layers,” *Adv. Mater. Interfaces*, vol. 3, no. 19, p. 1600320, Oct. 2016.
- [3] P. Yimsiri and M. R. MacKley, “Spin and dip coating of light-emitting polymer solutions: Matching experiment with modelling,” *Chem. Eng. Sci.*, vol. 61, no. 11, pp. 3496–3505, 2006.
- [4] N. F. Mott, “Electrons in disordered structures,” *Adv. Phys.*, vol. 16, no. 61, pp. 49–144, Jan. 1967.
- [5] V. Coropceanu, J. Cornil, D. A. da Silva Filho, Y. Olivier, R. Silbey, and J. L. Brédas, “Charge transport in organic semiconductors,” *Chemical Reviews*, vol. 107, no. 4. American Chemical Society, pp. 926–952, 2007.
- [6] T. H. El-Assaad, M. Auer, R. Castañeda, K. M. Hallal, F. M. Jradi, L. Mosca, R. S. Khnayzer, D. Patra, T. V. Timofeeva, J.-L. Brédas, E. J. W. List-Kratochvil, B. Wex, and B. R. Kaafarani, “Tetraaryl pyrenes: photophysical properties, computational studies, crystal structures, and application in OLEDs,” *J. Mater. Chem. C*, vol. 4, no. 14, pp. 3041–3058, 2016.
- [7] R. H. Young and J. J. Fitzgerald, “Effect of polar additives on charge transport in a molecularly doped polymer: Survey of various additives,” *J. Chem. Phys.*, vol. 102, no. 5, pp. 2209–2221, Feb. 1995.
- [8] J. C. Scott, “Metal-organic interface and charge injection in organic electronic devices,” *Cit. J. Vac. Sci. Technol. A*, vol. 21, p. 521, 2003.

- [9] R. Schmechel, "Hopping transport in doped organic semiconductors: A theoretical approach and its application to p-doped zinc-phthalocyanine," *Cit. J. Appl. Phys.*, vol. 93, p. 4653, 2003.
- [10] H. Yersin, "Triplet Emitters for OLED Applications. Mechanisms of Exciton Trapping and Control of Emission Properties," pp. 1–26, 2004.
- [11] D. J. Gaspar and E. Polikarpov, *OLED fundamentals : materials, devices, and processing of organic light-emitting diodes. .*
- [12] S. Haneder, E. Da Como, J. Feldmann, J. M. Lupton, C. Lennartz, P. Erk, E. Fuchs, O. Molt, I. M??nster, C. Schildknecht, and G. Wagenblast, "Controlling the radiative rate of deep-blue electrophosphorescent organometallic complexes by singlet-triplet gap engineering," *Adv. Mater.*, vol. 20, no. 17, pp. 3325–3330, 2008.
- [13] S. Reineke and M. A. Baldo, "Recent progress in the understanding of exciton dynamics within phosphorescent OLEDs," *Phys. Status Solidi Appl. Mater. Sci.*, vol. 209, no. 12, pp. 2341–2353, 2012.
- [14] M. A. Baldo, D. F. O 'brien, Y. You, A. Shoustikov, S. Sibley, M. E. Thompson, and S. R. Forrest, "Highly efficient phosphorescent emission from organic electroluminescent devices," *Nature*, vol. 395, no. September, pp. 151–154, 1998.
- [15] J. Lee, C. Jeong, T. Batagoda, C. Coburn, M. E. Thompson, and S. R. Forrest, "Hot excited state management for long-lived blue phosphorescent organic light-emitting diodes," *Nat. Commun.*, vol. 8, no. May, p. 15566, 2017.
- [16] M. A. Baldo and S. R. Forrest, "Transient analysis of organic electrophosphorescence: I. Transient analysis of triplet energy transfer," *Phys. Rev. B - Condens. Matter Mater. Phys.*, vol. 62, no. 16, pp. 10958–10966, 2000.

- [17] M. A. Baldo, C. Adachi, and S. R. Forrest, “Transient analysis of organic electrophosphorescence. II. Transient analysis of triplet-triplet annihilation,” *Phys. Rev. B - Condens. Matter Mater. Phys.*, vol. 62, no. 16, pp. 10967–10977, 2000.
- [18] Y. Zhang and S. R. Forrest, “Triplet diffusion leads to triplet-triplet annihilation in organic phosphorescent emitters,” *Chem. Phys. Lett.*, vol. 590, pp. 106–110, 2013.
- [19] C. Adachi, “Third-generation organic electroluminescence materials,” *Jpn. J. Appl. Phys.*, vol. 53, no. 6, 2014.
- [20] A. Salehi, S. Ho, Y. Chen, C. Peng, H. Yersin, and F. So, “Highly Efficient Organic Light-Emitting Diode Using A Low Refractive Index Electron Transport Layer,” *Adv. Opt. Mater.*, vol. 1700197, p. 1700197, 2017.
- [21] H. Nakanotani, K. Masui, J. Nishide, T. Shibata, and C. Adachi, “Promising operational stability of high-efficiency organic light-emitting diodes based on thermally activated delayed fluorescence,” *Sci. Rep.*, vol. 3, no. 1, p. 2127, Dec. 2013.
- [22] S. Wu, M. Aonuma, Q. Zhang, S. Huang, T. Nakagawa, K. Kuwabara, and C. Adachi, “High-efficiency deep-blue organic light-emitting diodes based on a thermally activated delayed fluorescence emitter,” *J. Mater. Chem. C*, vol. 2, no. 3, pp. 421–424, 2014.
- [23] Q. Zhang, B. Li, S. Huang, H. Nomura, H. Tanaka, and C. Adachi, “Efficient blue organic light-emitting diodes employing thermally activated delayed fluorescence,” *Nat. Photonics*, vol. 8, no. 4, pp. 326–332, Apr. 2014.
- [24] J. Guo, X.-L. Li, H. Nie, W. Luo, S. Gan, S. Hu, R. Hu, A. Qin, Z. Zhao, S.-J. Su, and B. Z. Tang, “Achieving High-Performance Nondoped OLEDs with Extremely Small Efficiency Roll-Off by Combining Aggregation-Induced Emission and Thermally Activated Delayed Fluorescence,” *Adv. Funct. Mater.*, vol. 27, no. 13, p. 1606458, Apr.

- 2017.
- [25] B. J. Chen, S. C. Tan, and X. W. Sun, “The role of LiF buffer layer in tris-(8-hydroxyquinoline) aluminum-based organic light-emitting devices with Mg:Ag cathode,” *J. Soc. Inf. Disp.*, vol. 13, no. 5, p. 443, May 2005.
- [26] L.-W. Xin, X.-M. Wu, Y.-L. Hua, Z.-H. Xiao, L. Wang, X. Zhang, and S.-G. Yin, “Improvement of electron injection of organic light-emitting devices by inserting a thin aluminum layer into cesium carbonate injection layer,” *Chinese Phys. B*, vol. 24, no. 3, p. 037802, Mar. 2015.
- [27] S. Y. Kim, J.-L. Lee, K.-B. Kim, and Y.-H. Tak, “Effect of ultraviolet–ozone treatment of indium–tin–oxide on electrical properties of organic light emitting diodes,” *J. Appl. Phys.*, vol. 95, no. 5, pp. 2560–2563, Mar. 2004.
- [28] S.-H. Wen, A. Li, J. Song, W.-Q. Deng, K.-L. Han, and W. A. Goddard, “First-Principles Investigation of Anisotropic Hole Mobilities in Organic Semiconductors,” *J. Phys. Chem. B*, vol. 113, no. 26, pp. 8813–8819, Jul. 2009.
- [29] S. Scholz, D. Kondakov, B. Lüssem, and K. Leo, “Degradation mechanisms and reactions in organic light-emitting devices,” *Chem. Rev.*, vol. 115, no. 16, pp. 8449–8503, 2015.
- [30] Y. J. Pu, G. Nakata, F. Satoh, H. Sasabe, D. Yokoyama, and J. Kido, “Optimizing the charge balance of fluorescent organic light-emitting devices to achieve high external quantum efficiency beyond the conventional upper limit,” *Adv. Mater.*, vol. 24, no. 13, pp. 1765–1770, 2012.
- [31] N. Chopra, J. Lee, Y. Zheng, S.-H. Eom, J. Xue, and F. So, “Effect of the Charge Balance on High-Efficiency Blue-Phosphorescent Organic Light-Emitting Diodes,” *ACS Appl. Mater. Interfaces*, vol. 1, no. 6, pp. 1169–1172, Jun. 2009.

- [32] P. Tyagi, R. Srivastava, A. Kumar, S. Tuli, and M. N. Kamalasanan, “Effect of doping of cesium carbonate on electron transport in Tris(8-hydroxyquinolino) aluminum,” *Org. Electron. physics, Mater. Appl.*, vol. 14, no. 5, pp. 1391–1395, 2013.
- [33] M. Ikai, S. Tokito, Y. Sakamoto, T. Suzuki, and Y. Taga, “Highly efficient phosphorescence from organic light-emitting devices with an exciton-block layer,” *Cit. Appl. Phys. Lett.*, vol. 79, p. 156, 2001.
- [34] N. Seidler, S. Reineke, K. Walzer, B. Lüssem, A. Tomkeviciene, J. V. Grazulevicius, and K. Leo, “Influence of the hole blocking layer on blue phosphorescent organic light-emitting devices using 3,6-di(9-carbazolyl)-9-(2-ethylhexyl)carbazole as host material,” *Appl. Phys. Lett.*, vol. 96, no. 9, p. 093304, Mar. 2010.
- [35] S. T. Zhang, Z. J. Wang, J. M. Zhao, Y. Q. Zhan, Y. Wu, Y. C. Zhou, X. M. Ding, and X. Y. Hou, “Electron blocking and hole injection: The role of N,N-Bis(phenyl)-1,8-naphthalen-1,8-diylium in organic light-emitting devices,” *Appl. Phys. Lett.*, vol. 84, p. 12, 2004.
- [36] W. S. Jeon, T. J. Park, S. Y. Kim, R. Pode, J. Jang, and J. H. Kwon, “Ideal host and guest system in phosphorescent OLEDs,” *Org. Electron.*, vol. 10, no. 2, pp. 240–246, Apr. 2009.
- [37] L.-Z. Yu, X.-Y. Jiang, Z.-L. Zhang, L.-R. Lou, and C.-T. Lee, “Investigation of Förster-type energy transfer in organic light-emitting devices with 4-(dicyanomethylene)-2-t-butyl-6-(1,1,7,7-tetramethyljulolidin-4-yl-vinyl)-4H-pyran doped cohost emitting layer,” 2009.
- [38] J. W. Kim, S. Il You, N. H. Kim, J.-A. Yoon, K. W. Cheah, F. R. Zhu, and W. Y. Kim, “Study of Sequential Dexter Energy Transfer in High Efficient Phosphorescent White

- Organic Light-Emitting Diodes with Single Emissive Layer,” *Sci. Rep.*, vol. 4, no. 1, p. 7009, May 2015.
- [39] S. Nowy, B. C. Krummacher, J. Frischeisen, N. A. Reinke, and W. Brütting, “Light extraction and optical loss mechanisms in organic light-emitting diodes: Influence of the emitter quantum efficiency,” *J. Appl. Phys.*, vol. 104, no. 12, 2008.
- [40] A. Salehi, Y. Chen, X. Fu, C. Peng, and F. So, “Manipulating Refractive Index in Organic Light Emitting Diodes,” *ACS Appl. Mater. Interfaces*, no. March, p. acsami.7b18514, Mar. 2018.
- [41] J. Lee, T. H. Han, M. H. Park, D. Y. Jung, J. Seo, H. K. Seo, H. Cho, E. Kim, J. Chung, S. Y. Choi, T. S. Kim, T. W. Lee, and S. Yoo, “Synergetic electrode architecture for efficient graphene-based flexible organic light-emitting diodes,” *Nat. Commun.*, vol. 7, pp. 1–9, 2016.
- [42] C. W. Tang and S. A. Vanslyke, “Coupling Efficiency Enhancement in Organic Light-Emitting Devices Using Microlens Array-Theory and Experiment,” 1987.
- [43] S. Mladenovski, K. Neyts, D. Pavicic, A. Werner, and C. Rothe, “Exceptionally efficient organic light emitting devices using high refractive index substrates,” *Opt. Express*, vol. 17, no. 9, p. 7562, 2009.
- [44] Y. Sun and S. R. Forrest, “Enhanced light out-coupling of organic light-emitting devices using embedded low-index grids,” *Nat Phot.*, vol. 2, pp. 483–487, 2008.
- [45] Y. Qu, C. Coburn, D. Fan, and S. R. Forrest, “Elimination of Plasmon Losses and Enhanced Light Extraction of Top-Emitting Organic Light-Emitting Devices Using a Reflective Subelectrode Grid,” *ACS Photonics*, vol. 4, no. 2, pp. 363–368, Feb. 2017.
- [46] W. L. Barnes, “Fluorescence near interfaces: the role of photonic mode density,” *J. Mod.*

- Opt.*, vol. 45, no. 4, pp. 661–699, 1998.
- [47] R. R. Chance, A. Prock, and R. Silbey, “Lifetime of an emitting molecule near a partially reflecting surface,” *J. Chem. Phys.*, vol. 60, no. 7, pp. 2744–2748, Apr. 1974.
- [48] I. Prigogine and S. A. Rice, *Advances in Chemical Physics*, 37. John Wiley & Sons, 2009.
- [49] T. D. Schmidt, B. J. Scholz, C. Mayr, and W. Brütting, “Efficiency Analysis of Organic Light-Emitting Diodes Based on Optical Simulations,” *IEEE J. Sel. Top. Quantum Electron.*, vol. 19, no. 5, pp. 1–12, Sep. 2013.
- [50] M. C. Gather and S. Reineke, “Recent advances in light outcoupling from white organic light-emitting diodes,” *J. Photonics Energy*, vol. 5, no. 1, p. 057607, May 2015.
- [51] W. Brütting, J. Frischeisen, T. D. Schmidt, B. J. Scholz, and C. Mayr, “Device efficiency of organic light-emitting diodes: Progress by improved light outcoupling,” *Phys. Status Solidi Appl. Mater. Sci.*, vol. 210, no. 1, pp. 44–65, 2013.
- [52] FIUXiM, *SETFOS 4.4 Manual*. Feusisberg, Switzerland: Fluxim AG, 2016.
- [53] N. A. Reinke, “Photophysikalische Prozesse und Lichtextraktion in organischen Leuchtdioden,” University of Augsburg, Germany, 2008.
- [54] D. E. Aspnes, *Advanced Electromagnetism Lectures*. Raleigh NC, 2014.
- [55] D. E. Aspnes, “Bond models in linear and nonlinear optics,” *Phys. Status Solidi*, vol. 247, no. 8, pp. 1873–1880, 2010.
- [56] L. Penninck, S. Mladenowski, and K. Neyts, “The effects of planar metallic interfaces on the radiation of nearby electrical dipoles,” *J. Opt.*, vol. 12, no. 7, p. 075001, 2010.
- [57] K. Kim, C. Moon, J. Lee, S. Kim, and J. Kim, “Highly Efficient Organic Light-Emitting Diodes with Phosphorescent Emitters Having High Quantum Yield and Horizontal Orientation of Transition Dipole Moments,” pp. 3844–3847, 2014.

- [58] S.-Y. Kim, W.-I. Jeong, C. Mayr, Y.-S. Park, K.-H. Kim, J.-H. Lee, C.-K. Moon, W. Brütting, and J.-J. Kim, “Organic Light-Emitting Diodes with 30% External Quantum Efficiency Based on a Horizontally Oriented Emitter,” *Adv. Funct. Mater.*, vol. 23, no. 31, pp. 3896–3900, Aug. 2013.
- [59] J. Frischeisen, D. Yokoyama, A. Endo, C. Adachi, and W. Brütting, “Increased light outcoupling efficiency in dye-doped small molecule organic light-emitting diodes with horizontally oriented emitters,” *Org. Electron.*, vol. 12, no. 5, pp. 809–817, May 2011.
- [60] D. Yokoyama, “Molecular orientation in small-molecule organic light-emitting diodes,” *J. Mater. Chem.*, vol. 21, no. 48, p. 19187, 2011.
- [61] P. Yeh, *Optical Waves in Layered Media*, 2nd editio. Wiley-Interscience, 2005.
- [62] W. H. Koo, W. Youn, P. Zhu, X.-H. Li, N. Tansu, and F. So, “Light Extraction of Organic Light Emitting Diodes by Defective Hexagonal-Close-Packed Array,” *Adv. Funct. Mater.*, vol. 22, no. 16, pp. 3454–3459, Aug. 2012.
- [63] B. J. Matterson, J. M. Lupton, A. F. Safonov, M. G. Salt, W. L. Barnes, and I. D. W. Samuel, “Increased Efficiency and Controlled Light Output from a Microstructured Light-Emitting Diode,” *Adv. Mater.*, vol. 13, no. 2, pp. 123–127, Jan. 2001.
- [64] C.-K. Moon, S.-Y. Kim, J.-H. Lee, and J.-J. Kim, “Luminescence from oriented emitting dipoles in a birefringent medium,” *Opt. Express*, vol. 23, no. 7, pp. A279–A291, 2015.
- [65] M. K. Callens, D. Yokoyama, and K. Neyts, “Anisotropic materials in OLEDs for high outcoupling efficiency,” *Opt. Express*, vol. 23, no. 16, pp. 21128–21148, 2015.
- [66] H. Shin, J. H. Lee, C. K. Moon, J. S. Huh, B. Sim, and J. J. Kim, “Sky-Blue Phosphorescent OLEDs with 34.1% External Quantum Efficiency Using a Low Refractive Index Electron Transporting Layer,” *Adv. Mater.*, pp. 4920–4925, 2016.

- [67] D. M. Zink, L. Bergmann, D. Ambrosek, M. Wallesch, D. Volz, and M. Mydlak, "Singlet harvesting copper-based emitters: a modular approach towards next-generation OLED technology," *Transl. Mater. Res.*, vol. 1, no. 1, p. 15003, 2014.
- [68] K. S. Yook and J. Y. Lee, "Small molecule host materials for solution processed phosphorescent organic light-emitting diodes," *Adv. Mater.*, vol. 26, no. 25, pp. 4218–4233, 2014.
- [69] B. Chen, L. Zhao, J. Ding, L. Wang, X. Jing, and F. Wang, "An alcohol-soluble and ion-free electron transporting material functionalized with phosphonate groups for solution-processed multilayer PLEDs," *Chem. Commun.*, vol. 52, no. 81, pp. 12052–12055, Oct. 2016.
- [70] K. S. Yook and J. Y. Lee, "Small Molecule Host Materials for Solution Processed Phosphorescent Organic Light-Emitting Diodes," *Adv. Mater.*, vol. 26, no. 25, pp. 4218–4233, Jul. 2014.
- [71] C. Xiang, N. Chopra, J. Wang, C. Brown, S. Ho, M. Mathai, and F. So, "Phosphorescent organic light emitting diodes with a cross-linkable hole transporting material," *Org. Electron.*, vol. 15, no. 7, pp. 1702–1706, Jul. 2014.
- [72] Q. Zhang, T. Komino, S. Huang, S. Matsunami, K. Goushi, and C. Adachi, "Triplet exciton confinement in green organic light-emitting diodes containing luminescent charge-transfer Cu(I) complexes," *Adv. Funct. Mater.*, vol. 22, no. 11, pp. 2327–2336, 2012.
- [73] H.-F. Chen, T.-C. Wang, S.-W. Lin, W.-Y. Hung, H.-C. Dai, H.-C. Chiu, K.-T. Wong, M.-H. Ho, T.-Y. Cho, C.-W. Chen, and C.-C. Lee, "Peripheral modification of 1,3,5-triazine based electron-transporting host materials for sky blue, green, yellow, red, and white

- electrophosphorescent devices,” *J. Mater. Chem.*, vol. 22, no. 31, p. 15620, Jul. 2012.
- [74] X.-P. Lv, H. Wang, L.-Q. Meng, X.-F. Wei, Y.-Z. Chen, X.-B. Kong, J.-J. Liu, J.-X. Tang, P.-F. Wang, and Y. Wang, “High Efficiency and Stable Organic Light-Emitting Diodes Based on Thermally Activated Delayed Fluorescence Emitter,” *Chinese Phys. Lett.*, vol. 33, no. 8, p. 088501, 2016.
- [75] T. Furukawa, H. Nakanotani, M. Inoue, and C. Adachi, “Dual enhancement of electroluminescence efficiency and operational stability by rapid upconversion of triplet excitons in OLEDs,” *Sci. Rep.*, vol. 5, p. 8429, 2015.
- [76] D. Volz, Y. Chen, M. Wallesch, R. Liu, C. Fléchon, D. M. Zink, J. Friedrichs, H. Flügge, R. Steininger, J. Göttlicher, C. Heske, L. Weinhardt, S. Bräse, F. So, and T. Baumann, “Bridging the efficiency gap: Fully bridged dinuclear Cu(I)-complexes for singlet harvesting in high-efficiency OLEDs,” *Adv. Mater.*, vol. 27, no. 15, pp. 2538–2543, 2015.
- [77] C. Xiang, W. Koo, F. So, H. Sasabe, and J. Kido, “A systematic study on efficiency enhancements in phosphorescent green, red and blue microcavity organic light emitting devices,” *Light Sci. Appl.*, vol. 2, no. 6, pp. e74–e74, Jun. 2013.
- [78] D. Tanaka, Y. Agata, T. Takeda, S. Watanabe, and J. Kido, “High Luminous Efficiency Blue Organic Light-Emitting Devices Using High Triplet Excited Energy Materials,” *Jpn. J. Appl. Phys.*, vol. 46, no. 5, pp. L117–L119, 2007.
- [79] D. Tanaka, T. Takeda, T. Chiba, S. Watanabe, and J. Kido, “Novel Electron-transport Material Containing Boron Atom with a High Triplet Excited Energy Level,” *Chem. Lett.*, vol. 36, no. 2, pp. 262–263, 2007.
- [80] X. B. Chu, M. Guan, L. T. Niu, Y. Zhang, Y. Y. Li, X. F. Liu, and Y. P. Zeng, “The utilization of low-temperature evaporable CsN3-doped NBphen as an alternative and

- efficient electron-injection layer in OLED,” *Phys. Status Solidi Appl. Mater. Sci.*, vol. 211, no. 7, pp. 1605–1609, 2014.
- [81] S. Naka, H. Okada, H. Onnagawa, and T. Tsutsui, “High electron mobility in bathophenanthroline,” *Appl. Phys. Lett.*, vol. 76, no. 2, p. 197, 2000.
- [82] M. J. Leitl, D. M. Zink, A. Schinabeck, T. Baumann, D. Volz, and H. Yersin, “Copper(I) Complexes for Thermally Activated Delayed Fluorescence: From Photophysical to Device Properties,” *Top. Curr. Chem.*, vol. 374, no. 3, 2016.
- [83] D. Hill, “The Optical Outcoupling of Organic Light Emitting Diodes,” *Thesis*, no. June, 2008.
- [84] S. Nowy, J. Frischeisen, and W. Brütting, “Simulation based optimization of light-outcoupling in organic light-emitting diodes,” 2009, vol. 7415, p. 74151C.
- [85] S. Ho, Y. Chen, S. Liu, C. Peng, D. Zhao, and F. So, “Interface Effect on Efficiency Loss in Organic Light Emitting Diodes with Solution Processed Emitting Layers,” *Adv. Mater. Interfaces*, vol. 3, no. 19, pp. 1–6, 2016.
- [86] L. A. . Pettersson, S. Ghosh, and O. Inganäs, “Optical anisotropy in thin films of poly(3,4-ethylenedioxythiophene)–poly(4-styrenesulfonate),” *Org. Electron.*, vol. 3, no. 3, pp. 143–148, 2002.
- [87] M. Shibata, Y. Sakai, and D. Yokoyama, “Advantages and disadvantages of vacuum-deposited and spin-coated amorphous organic semiconductor films for organic light-emitting diodes,” *J. Mater. Chem. C*, vol. 3, no. 42, pp. 11178–11191, Oct. 2015.
- [88] J. Q. Xi, M. F. Schubert, J. K. Kim, E. F. Schubert, M. Chen, S.-Y. Lin, W. Liu, and J. A. Smart, “Optical thin-filmmaterials with low refractive index for broadband elimination of Fresnel reflection,” *Nat. Photonics*, vol. 1, pp. 176–179, Feb. 2007.

- [89] J. K. Kim, S. Chhajed, M. F. Schubert, E. F. Schubert, A. J. Fischer, M. H. Crawford, J. Cho, H. Kim, and C. Sone, "Light-extraction enhancement of GaInN light-emitting diodes by graded-refractive-index indium tin oxide anti-reflection contact," *Adv. Mater.*, vol. 20, no. 4, pp. 801–804, 2008.
- [90] M. F. Schubert, D. J. Poxson, F. W. Mont, J. K. Kim, and E. F. Schubert, "Performance of antireflection coatings consisting of multiple discrete layers and comparison with continuously graded antireflection coatings," *Appl. Phys. Express*, vol. 3, no. 8, pp. 3–5, 2010.
- [91] A. Barranco, A. Borrás, A. R. González-Elipé, and A. Palmero, "Perspectives on oblique angle deposition of thin films: From fundamentals to devices," *Prog. Mater. Sci.*, vol. 76, pp. 59–153, 2016.
- [92] B. Szeto, P. C. P. Hruday, J. Gospodyn, J. C. Sit, and M. J. Brett, "Obliquely deposited tris(8-hydroxyquinoline) aluminium (Alq₃) biaxial thin films with negative in-plane birefringence," *J. Opt. A Pure Appl. Opt.*, vol. 9, no. 5, pp. 457–462, 2007.
- [93] Y. Zhong, Y. C. Shin, C. M. Kim, B. G. Lee, E. H. Kim, Y. J. Park, K. M. a. Sobahan, C. K. Hwangbo, Y. P. Lee, and T. G. Kim, "Optical and electrical properties of indium tin oxide thin films with tilted and spiral microstructures prepared by oblique angle deposition," *J. Mater. Res.*, vol. 23, no. 09, pp. 2500–2505, 2008.
- [94] M. Slights and S. R. Forrest, "Enhancing waveguided light extraction in organic LEDs using an ultra-low-index grid," *Opt. Lett.*, vol. 35, no. 7, pp. 1052–4, 2010.
- [95] K. Saxena, D. S. Mehta, R. Srivastava, and M. N. Kamalasanan, "Effect of oblique angle deposition of α -naphthylphenylbiphenyl diamine on the performance of organic light-emitting diodes," *J. Phys. D. Appl. Phys.*, vol. 41, no. 1, p. 015102, 2008.

- [96] A. Kumar, R. Srivastava, M. N. Kamalasanan, and D. S. Mehta, "Enhancement of light extraction efficiency of organic light emitting diodes using nanostructured indium tin oxide.," *Opt. Lett.*, vol. 37, no. 4, pp. 575–7, 2012.
- [97] C. Y. Lu, M. Jiao, W. K. Lee, C. Y. Chen, W. L. Tsai, C. Y. Lin, and C. C. Wu, "Achieving Above 60% External Quantum Efficiency in Organic Light-Emitting Devices Using ITO-Free Low-Index Transparent Electrode and Emitters with Preferential Horizontal Emitting Dipoles," *Adv. Funct. Mater.*, pp. 3250–3258, 2016.
- [98] M. Cai, Z. Ye, T. Xiao, R. Liu, Y. Chen, R. W. Mayer, R. Biswas, K. M. Ho, R. Shinar, and J. Shinar, "Extremely efficient indium-tin-oxide-free green phosphorescent organic light-emitting diodes," *Adv. Mater.*, vol. 24, no. 31, pp. 4337–4342, 2012.
- [99] T. W. Koh, J. M. Choi, S. Lee, and S. Yoo, "Optical outcoupling enhancement in organic light-emitting diodes: highly conductive polymer as a low-index layer on microstructured ITO electrodes," *Adv. Mater.*, vol. 22, no. 16, pp. 1849–1853, 2010.
- [100] M. K. Callens, D. Yokoyama, and K. Neyts, "Anisotropic materials in OLEDs for high outcoupling efficiency," *Opt. Express*, vol. 23, no. 16, p. 21128, Aug. 2015.
- [101] D. Yokoyama, "Molecular orientation in small-molecule organic light-emitting diodes," *J. Mater. Chem.*, vol. 21, no. 48, p. 19187, 2011.
- [102] P. C. P. Hrudehy, K. L. Westra, and M. J. Brett, "Highly ordered organic Alq3 chiral luminescent thin films fabricated by glancing-angle deposition," *Adv. Mater.*, vol. 18, no. 2, pp. 224–228, 2006.
- [103] S. Tsoi, B. Szeto, M. D. Fleischauer, J. G. C. Veinot, and M. J. Brett, "Control of Alq3 wetting layer thickness via substrate surface functionalization," *Langmuir*, vol. 23, no. 12, pp. 6498–6500, 2007.

- [104] M. Brinkmann, F. Biscarini, C. Taliani, I. Aiello, and M. Ghedini, "Growth of mesoscopic correlated droplet patterns by high-vacuum sublimation," *Phys. Rev. B*, vol. 61, no. 24, pp. R16339–R16342, 2000.
- [105] J. A. Thornton, "The microstructure of sputter-deposited coatings," *J. Vac. Sci. Technol. A Vacuum, Surfaces, Film.*, vol. 4, no. 6, pp. 3059–3065, Nov. 1986.
- [106] K. H. Müller, "Dependence of thin-film microstructure on deposition rate by means of a computer simulation," *J. Appl. Phys.*, vol. 58, no. 7, pp. 2573–2576, 1985.
- [107] E. Mirica, G. Kowach, and H. Du, "Modified Structure Zone Model to Describe the Morphological Evolution of ZnO Thin Films Deposited by Reactive Sputtering," *Cryst. Growth Des.*, no. 4, pp. 157–159, 2004.
- [108] A. Anders, "A structure zone diagram including plasma-based deposition and ion etching," *Thin Solid Films*, vol. 518, no. 15, pp. 4087–4090, 2010.
- [109] M. H. Wang, Y. Sawada, K. Saito, S. Horie, T. Uchida, M. Ohtsuka, S. Seki, S. Kobayashi, T. Arai, A. Kishi, T. Takahashi, Y. Nishimoto, T. Wakimoto, K. Monzen, I. Kashima, T. Nishikiori, L. X. Sun, and R. Ozao, "Thermal change of Alq₃, tris(8-hydroxyquinolino) aluminum(III) studied by TG and XRD-DSC," *J. Therm. Anal. Calorim.*, vol. 89, no. 2, pp. 363–366, 2007.
- [110] G. Vamvounis, H. Aziz, N. X. Hu, and Z. D. Popovic, "Temperature dependence of operational stability of organic light emitting diodes based on mixed emitter layers," *Synth. Met.*, vol. 143, no. 1, pp. 69–73, 2004.
- [111] K. Naito and A. Miura, "Molecular design for nonpolymeric organic dye glasses with thermal stability: Relations between thermodynamic parameters and amorphous properties," *J. Phys. Chem.*, vol. 97, no. 23, pp. 6240–6248, 1993.

- [112] M. H. Tsai, Y. H. Hong, C. H. Chang, H. C. Su, C. C. Wu, A. Matoliukstyte, J. Simokaitiene, S. Grigalevicius, J. V. Grazulevicius, and C. P. Hsu, “3-(9-carbazolyl)carbazoles and 3,6-Di(9-carbazolyl)carbazoles as effective host materials for efficient blue organic electrophosphorescence,” *Adv. Mater.*, vol. 19, no. 6, pp. 862–866, 2007.
- [113] J. Lee, N. Chopra, S. H. Eom, Y. Zheng, J. Xue, F. So, and J. Shi, “Effects of triplet energies and transporting properties of carrier transporting materials on blue phosphorescent organic light emitting devices,” *Appl. Phys. Lett.*, vol. 93, no. 12, 2008.
- [114] B. Sim, C.-K. Moon, K.-H. Kim, and J.-J. Kim, “Quantitative Analysis of the Efficiency of OLEDs,” *ACS Appl. Mater. Interfaces*, p. acsami.6b10297, 2016.
- [115] FLUXiM, “SETFOS database.” Fluxim AG, Winterthur, Switzerland, 2017.
- [116] S. Kong, F. Application, and P. Data, “(12) United States Patent,” vol. 2, no. 12, pp. 12–15, 2011.
- [117] D. Jacquemin and D. Escudero, “The short device lifetimes of blue PhOLEDs: insights into the photostability of blue Ir(III) complexes,” *Chem. Sci.*, vol. 8, pp. 7844–7850, 2017.
- [118] J. Zhuang, W. Li, W. Su, Y. Liu, Q. Shen, L. Liao, and M. Zhou, “Highly efficient phosphorescent organic light-emitting diodes using a homoleptic iridium(III) complex as a sky-blue dopant,” *Org. Electron. physics, Mater. Appl.*, vol. 14, no. 10, pp. 2596–2601, 2013.
- [119] Y. J. Kang and J. Y. Lee, “High triplet energy electron transport type exciton blocking materials for stable blue phosphorescent organic light-emitting diodes,” *Org. Electron. physics, Mater. Appl.*, vol. 32, pp. 109–114, 2016.
- [120] C. Murawski, K. Leo, and M. C. Gather, “Efficiency roll-off in organic light-emitting

- diodes,” *Adv. Mater.*, vol. 25, no. 47, pp. 6801–6827, 2013.
- [121] X. Gong, M. R. Robinson, J. C. Ostrowski, D. Moses, G. C. Bazan, and A. J. Heeger, “High-Efficiency Polymer-Based Electrophosphorescent Devices,” *Adv. Mater.*, vol. 14, no. 8, pp. 581–585, Apr. 2002.
- [122] D. . O’Brien, C. Giebeler, R. . Fletcher, A. . Cadby, L. . Palilis, D. . Lidzey, P. . Lane, D. . Bradley, and W. Blau, “Electrophosphorescence from a doped polymer light emitting diode,” *Synth. Met.*, vol. 116, no. 1–3, pp. 379–383, Jan. 2001.
- [123] S. Difley, D. Beljonne, and T. Van Voorhis, “On the Singlet– Triplet Splitting of Geminate Electron– Hole Pairs in Organic Semiconductors,” *J. Am. Chem. Soc.*, vol. 130, no. 11, pp. 3420–3427, 2008.
- [124] D. Y. Kondakov, T. D. Pawlik, T. K. Hatwar, and J. P. Spindler, “Triplet annihilation exceeding spin statistical limit in highly efficient fluorescent organic light-emitting diodes,” *J. Appl. Phys.*, vol. 106, no. 12, 2009.
- [125] D. Y. Kondakov, “Role of triplet-triplet annihilation in highly efficient fluorescent devices,” *Journal of the Society for Information Display*, vol. 17, no. 2. p. 137, 2009.
- [126] C. J. Chiang, A. Kimyonok, M. K. Etherington, G. C. Griffiths, V. Jankus, F. Turksoy, and A. P. Monkman, “Ultrahigh efficiency fluorescent single and bi-layer organic light emitting diodes: The key role of triplet fusion,” *Adv. Funct. Mater.*, vol. 23, no. 6, pp. 739–746, 2013.
- [127] Y. J. Luo, Z. Y. Lu, and Y. Huang, “Triplet fusion delayed fluorescence materials for OLEDs,” *Chinese Chem. Lett.*, vol. 27, no. 8, pp. 1223–1230, 2016.
- [128] C. Xiang, C. Peng, Y. Chen, and F. So, “Origin of Sub-Bandgap Electroluminescence in Organic Light-Emitting Diodes,” no. 40, pp. 5439–5443, 2015.

- [129] B. Lin, C. J. Easley, C. Chen, P. Tseng, M. Lee, P.-H. Sher, J.-K. Wang, T.-L. Chiu, C.-F. Lin, C. J. Bardeen, and J.-H. Lee, “Exciplex-Sensitized Triplet–Triplet Annihilation in Heterojunction Organic Thin-Film,” *ACS Appl. Mater. Interfaces*, vol. 9, no. 12, pp. 10963–10970, 2017.
- [130] D. Kabra, M. H. Song, B. Wenger, R. H. Friend, and H. J. Snaith, “High efficiency composite metal oxide-polymer electroluminescent devices: A morphological and material based investigation,” *Adv. Mater.*, vol. 20, no. 18, pp. 3447–3452, 2008.
- [131] L. Qian, Y. Zheng, K. R. Choudhury, D. Bera, F. So, J. Xue, and P. H. Holloway, “Electroluminescence from light-emitting polymer / ZnO nanoparticle heterojunctions at sub-bandgap voltages,” pp. 384–389, 2010.
- [132] T. Suzuki, Y. Nonaka, T. Watabe, H. Nakashima, S. Seo, S. Shitagaki, and S. Yamazaki, “Highly efficient long-life blue fluorescent organic light-emitting diode exhibiting triplet-triplet annihilation effects enhanced by a novel hole-transporting material,” *Jpn. J. Appl. Phys.*, vol. 53, no. 5, pp. 1–6, 2014.
- [133] H. Fukagawa, T. Shimizu, N. Ohbe, S. Tokito, K. Tokumaru, and H. Fujikake, “Anthracene derivatives as efficient emitting hosts for blue organic light-emitting diodes utilizing triplet – triplet annihilation Spiro-FA,” *Org. Electron.*, vol. 13, no. 7, pp. 1197–1203, 2012.
- [134] H. Fukagawa, T. Shimizu, N. Ohbe, S. Tokito, K. Tokumaru, and H. Fujikake, “Anthracene derivatives as efficient emitting hosts for blue organic light-emitting diodes utilizing triplet – triplet annihilation Spiro-FA,” *Org. Electron.*, vol. 13, no. 7, pp. 1197–1203, 2012.
- [135] H. Park, J. Lee, I. Kang, H. Y. Chu, J.-I. Lee, S.-K. Kwon, and Y.-H. Kim, “Highly rigid

- and twisted anthracene derivatives: a strategy for deep blue OLED materials with theoretical limit efficiency,” *J. Mater. Chem.*, vol. 22, no. 6, pp. 2695–2700, 2012.
- [136] D. Y. Kondakov, “Characterization of triplet-triplet annihilation in organic light-emitting diodes based on anthracene derivatives,” *J. Appl. Phys.*, vol. 102, no. 11, 2007.
- [137] A. Haefele, J. Rg Blumhoff, R. S. Khnayzer, and F. N. Castellano, “Getting to the (Square) Root of the Problem: How to Make Noncoherent Pumped Upconversion Linear,” *J. Phys. Chem. Lett.*, vol. 3, pp. 299–303, 2012.
- [138] B. A. K. Pandey and J. Nunzi, “Rubrene / Fullerene Heterostructures With a Half-Gap Electroluminescence Threshold And Large Photovoltage **,” pp. 3613–3617, 2007.
- [139] S. E. Shaheen, G. E. Jabbour, M. M. Morrell, Y. Kawabe, B. Kippelen, N. Peyghambarian, M. F. Nabor, R. Schlaf, E. A. Mash, and N. R. Armstrong, “Bright blue organic light-emitting diode with improved color purity using a LiF/Al cathode,” *J. Appl. Phys.*, vol. 84, no. 4, pp. 2324–2327, 1998.
- [140] S. Berleb, W. Brütting, and G. Paasch, “Interfacial charges and electric field distribution in organic hetero-layer light-emitting devices,” *Org. Electron. physics, Mater. Appl.*, 2000.
- [141] S. Gong, X. He, Y. Chen, Z. Jiang, C. Zhong, D. Ma, J. Qin, and C. Yang, “Simple CBP isomers with high triplet energies for highly efficient blue electrophosphorescence,” *J. Mater. Chem.*, vol. 22, no. 7, pp. 2894–2899, 2012.
- [142] Y.-H. Chen, C.-C. Lin, M.-J. Huang, K. Hung, Y.-C. Wu, W.-C. Lin, R.-W. Chen-Cheng, H.-W. Lin, and C.-H. Cheng, “Superior upconversion fluorescence dopants for highly efficient deep-blue electroluminescent devices,” *Chem. Sci.*, vol. 7, no. 7, pp. 4044–4051, 2016.

- [143] J. W. Sun, J. Y. Baek, K. H. Kim, C. K. Moon, J. H. Lee, S. K. Kwon, Y. H. Kim, and J. J. Kim, "Thermally Activated Delayed Fluorescence from Azasiline Based Intramolecular Charge-Transfer Emitter (DTPDDA) and a Highly Efficient Blue Light Emitting Diode," *Chem. Mater.*, vol. 27, no. 19, pp. 6675–6681, 2015.
- [144] M. Kim, S. K. Jeon, S. H. Hwang, S. S. Lee, E. Yu, and J. Y. Lee, "Correlation of Molecular Structure with Photophysical Properties and Device Performances of Thermally Activated Delayed Fluorescent Emitters," *J. Phys. Chem. C*, vol. 120, no. 5, pp. 2485–2493, 2016.
- [145] W. Song, I. Lee, and J. Y. Lee, "Host Engineering for High Quantum Efficiency Blue and White Fluorescent Organic Light-Emitting Diodes," *Adv. Mater.*, vol. 27, no. 29, pp. 4358–4363, 2015.
- [146] M. Kim, S. K. Jeon, S. H. Hwang, and J. Y. Lee, "Stable blue thermally activated delayed fluorescent organic light-emitting diodes with three times longer lifetime than phosphorescent organic light-emitting diodes," *Adv. Mater.*, vol. 27, no. 15, pp. 2515–2520, 2015.
- [147] S. O. Jeon, S. E. Jang, H. S. Son, and J. Y. Lee, "External quantum efficiency above 20% in deep blue phosphorescent organic light-emitting diodes," *Adv. Mater.*, vol. 23, no. 12, pp. 1436–1441, 2011.
- [148] H. Sasabe, J. I. Takamatsu, T. Motoyama, S. Watanabe, G. Wagenblast, N. Langer, O. Molt, E. Fuchs, C. Lennartz, and J. Kido, "High-efficiency blue and white organic light-emitting devices incorporating a blue iridium carbene complex," *Adv. Mater.*, vol. 22, no. 44, pp. 5003–5007, 2010.
- [149] W. Song and K. S. Yook, "Hyperfluorescence-based full fluorescent white organic light-

- emitting diodes,” *J. Ind. Eng. Chem.*, no. 2017, pp. 10–13, 2018.
- [150] S. H. Han and J. Y. Lee, “Spatial separation of sensitizer and fluorescent emitter for high quantum efficiency in hyperfluorescent organic light-emitting diodes,” *J. Mater. Chem. C*, vol. 6, no. 6, pp. 1504–1508, 2018.
- [151] S. K. Jeon, H.-J. Park, and J. Y. Lee, “Highly Efficient Soluble Blue Delayed Fluorescent and Hyperfluorescent Organic Light-Emitting Diodes by Host Engineering,” *ACS Appl. Mater. Interfaces*, vol. 10, no. 6, pp. 5700–5705, 2018.
- [152] Y. Esaki, T. Komino, T. Matsushima, and C. Adachi, “Enhanced Electrical Properties and Air Stability of Amorphous Organic Thin Films by Engineering Film Density,” 2017.
- [153] T. D. Schmidt, T. Lampe, M. R. Daniel Sylvinson, P. I. Djurovich, M. E. Thompson, and W. Brütting, “Emitter Orientation as a Key Parameter in Organic Light-Emitting Diodes,” *Phys. Rev. Appl.*, vol. 8, no. 3, pp. 1–28, 2017.